

https://dspace.org/

Cross-section transmission electron microscopy of the ion implantation damage in annealed diamond

Nshingabigwi, Emmanuel Korawinga

2014-01-06
http://hdl.handle.net10539/13350

Downloaded from a DSpace repository. https://dspace.org/

CROSS-SECTION TRANSMISSION ELECTRON MICROSCOPY OF THE ION IMPLANTATION DAMAGE IN ANNEALED DIAMOND

Emmanuel K. Nshingabigwi

A thesis submitted to the Faculty of Science, University of the Witwatersrand, Johannesburg, in fulfilment of the requirements for the degree of Doctor of Philosophy.

Johannesburg, June, 2013

Declaration

I declare that this dissertation is my own unaided work. It is being submitted for the degree of Doctor of Philosophy in the University of the Witwatersrand, Johannesbourg. It has not been submitted before for any degree or examination in any other university.

_____

(Signature of candidate)

_____day of _____2013

Abstract

Diamond with its outstanding and unique physical properties offers the opportunity to be used as semiconductor material in future device technologies. Promising applications are, among others, high speed and high-power electronic devices working under extreme conditions, such as high temperature and harsh chemical environments. With respect to electronic applications, a controlled doping of the material is necessary which is preferably done by ion implantation. The ion implantation technique allows incorporation of foreign atoms at defined depths and with controlled spatial distribution which is not achievable with other methods. However, the ion implantation process is always connected with the formation of defects which compensate and trap charge carriers thus degrading the electrical behaviour. It is therefore essential to understand the nature of defects produced under various implantation conditions. In this respect, this study involves the investigation of the nature of the radiation damage produced during the multi-implantation of carbon ions in synthetic high-pressure, high-temperature (HPHT) type Ib diamond spread over a range of energies from 50 to 150 keV and fluences, using the cold-implantation-rapid-annealing (CIRA) routine. Single energy implantation of carbon ions in synthetic HPHT (type Ib), at room temperature, was also performed. Both ion milling and FIB (Focused Ion Beam) milling were used to prepare thin specimen for transmission electron microscope (TEM) analysis.

The unimplanted, implanted and annealed samples were characterized using transmission electron microscopy based techniques and Raman spectroscopy.

In unimplanted type Ia natural diamond, a high density of platelets, exhibiting the typical contrast of both edge-on and inclined platelets on {100} planes was found. As-implanted HPHT type Ib diamond, implanted with single energy of 150 keV carbon ions and fluence of 7×10^{15} ions cm^{-2} revealed an amorphous diamond layer of about 80 nm in thickness while, for low fluence implantations, the damaged diamond retained its crystallinity after annealing at 1600 K. In addition, damaged diamond transformed into disordered carbon comprising regions with bent (002) graphitic fringes and regions of amorphous carbon when high fluence, i.e., one above the amorphization/graphitisation threshold were used followed by rapid thermal annealing at 1600 K. Furthermore, the interface between the implanted and annealed layer and the diamond substrate at the end of the range, showed diamond crystallites, interspersed between regions of amorphous carbon and partially graphitized carbon. This indicates that solid phase epitaxial recrystallization regrowth in diamond does not occur.

Dedication

This work is dedicated to my wife Francine Mukandori, my children, Vaillant Manzi, Delice Mugeni and Prince Mugisha.

Acknowledgements

First and foremost, I would like to express my heartfelt gratitude and appreciation to all my supervisors Prof. T.E. Derry, Prof. J.H. Neethling and Dr. S.R. Naidoo for their guidance, support and patience throughout this thesis. It was through their concerted efforts that this thesis became a success.

I am also indebted to De Beers Industrial Diamond Division (Pty) South Africa for the donation of all the diamond samples used in this study. Mik Rebak and his assistant Tshepo Colby Mashego are thanked for expertly preparing the samples down to sub-50 μm, designing the diamond holder for edge-on implantations and laser-cutting all my cross-sectional electron microscope (TEM) specimens.

Prof. J.H. Neethling, Dr Jaco Olivier and Jacques O'Connel from the Centre for HRTEM at Nelson Mandela Metropolitan university (NMMU) where all the electron microscopy work was carried out are acknowledged for their expertise.

I would like to thank Dr C.M. Levitt, Prof. B. Skews, A. Voervelt and B. Fairbrother for valuable discussions for the design of a horizontal furnace setup for the rapid thermal annealing (RTA) of very thin diamonds slices.

I am grateful to the University of the Witwatersrand, the School of Physics, iThemba-LABS (Gauteng) and the Department of Science and Technology/National Research Foundation-Centre of Excellence in Strong Materials at Wits University for their support. Particularly, the financial support of the DST/NRF Centre of Excellence in Strong Materials (CoE-SM) towards this research is hereby acknowledged.

I would like to thank my fellow students/country men and friends for their moral

support and assistance. Special mention must be made of Dr Apollinaire Munyaneza, Dr Daniel Wamwangi, Dr Morgan Madhuku and Dr Rudolph Erasmus and Dr Nicholas Wambua for the many fruitful discussions that we had. I would like also to express my sincere thanks to Jean Berchmans , Marie, Anne Marie, Josephine, Kamanzi, Chantal, Mboni, Hyacinthe Murekatete, Emily Aradi, Wilfred Mbiombi, Isaac Motochi, Anna Kozakiewicz, George Manyali, Jacques Kayembe, Kalala Mbuyi, Pierre Bavon, Ruth Mawanda, Alain Mufula, Jonah KURIA, Kudakwashe Jakata, Oleary Moshe Bill, Daisy Moloko Malhare, Doris Monyamane, Marisa Kolver, Innocent Twagilimana, Nicholas Ade, Innocent Rusagara, Hilary Masenda and Mehluli Ncube for their companionship, help and encouragement.

Lastly, I would like to thank the LORD of lords for His grace and mercy.

Contents

List of Figures **xix**

List of Tables **xix**

1 Introduction **1**

1.1 Motivation 1

1.2 Thesis breakdown 5

2 Theoretical Background **6**

2.1 Layout of the chapter 6

2.2 Carbon and its main allotropes 6

2.3 Properties of diamond 12

2.3.1 Crystal structure 12

2.3.2 Classification of diamonds 16

2.4 HPHT diamond synthesis 18

2.5 Application of diamond 21

2.5.1 The doping of diamond 21

2.5.2 Other applications 21

2.6 Ion Implantation 23

2.6.1 Introduction 23

2.6.2 Energy-loss mechanisms 24

2.6.3 Radiation damage 32
2.6.4 Channelling 37

3 Experimental Techniques 39

3.1 Layout of the Chapter 39
3.2 Sample preparation (Mechanical Polishing) 40
3.3 Ion implantation 45
3.3.1 Introduction 45
3.3.2 Instrumentation 48
3.4 Annealing 50
3.4.1 Introduction 50
3.4.2 Cold-Implantation-Rapid-Annealing Technique 51
3.4.3 Instrumentation 53
3.5 Ion Milling 55
3.5.1 Introduction 55
3.5.2 Instrumentation 57
3.6 Focused ion beam milling(FIB) SEM 58
3.7 Characterization Techniques 60
3.7.1 Raman spectroscopy 60
3.7.2 Transmission Electron Microscopy 69

4 Results and Discussion 80

4.1 Layout of the Chapter 80
4.2 Simulation of ion implantation 80
4.3 Conventional transmission electron microscopy 82
4.3.1 X-TEM results of unimplanted, as-implanted and implanted and annealed samples obtained using conventional preparation methods. 83

4.3.2 Plan-view TEM results of ion beam thinned unimplanted samples acquired using conventional preparation methods. 87
4.3.3 X-TEM results of as-implanted, low and high fluences C^+-implanted diamond samples obtained using FIB-SEM preparation method. 91
4.4 EELS results of un-implanted, as-implanted, low and high fluences C^+-implanted diamond. 97
4.5 HRTEM results of high fluence carbon implanted diamond. 100
4.6 Raman spectroscopy of unimplanted, ion-beam thinned, as-implanted, low and high fluence C^+-implanted and annealed diamond samples. . 102

5 Summary and Conclusions **110**

References **112**

List of Figures

2.1 The sp^3, sp^2 and sp^1 hybridised bonding configurations. The unshaded and the shaded lobes denote strong bonds and weak bonds, respectively. sp^3, for example, signifies the overlap or combination of one s and 3p orbitals [21]. 8

2.2 Crystal structure of graphite highlighting ABAB planar stacking arrangement and unit cell [23]. 9

2.3 Ternary phase diagram of amorphous carbons. The three vertices correspond to diamond (sp^3), graphite (sp^2) and hydrocarbons [27]. . . . 11

2.4 A typical representation of a face-centred cubic lattice, with lattice points represented by black spheres [40]. 13

2.5 The diamond crystal lattice structure, with bases added at each point in the fcc lattice. The conventional unit cell vectors (x,y,z) are shown in blue while the primitive unit cell vectors ($V_1 = \frac{1}{2}\vec{i} + \frac{1}{2}\vec{j} + 0\vec{k}, V_2 = \frac{1}{2}\vec{i} + 0\vec{j} + \frac{1}{2}\vec{k}, V_3 = 0\vec{i} + \frac{1}{2}\vec{j} + \frac{1}{2}\vec{k}$ which define the minimum volume that can be translated to represent the diamond structure) are shown in red [40,41]. 14

2.6 Pressure/Temperature phase and transition diagram for carbon. Letters A, B, C, D, E, F and G show different regions within the phase diagram. The solid lines represent the equilibrium phase boundaries. Region A is where the commercial synthesis of diamond from graphite by catalysis is feasible. "Region B is the P/T threshold of very fast (less than 1ms) solid-solid transformation of graphite to diamond, Region C is the P/T threshold of very fast reversible phase transformation of diamond to graphite, region D is the region where single crystal hexagonal graphite transforms to retrieval hexagonal-type diamond, region E marks the upper ends of shock compression/quench cycles that convert hex-type graphite particles to hex-type diamond, region F designates the upper ends of shock compression/quench cycles that convert hex-type graphite to cubic-type diamond, region B-F-G indicates the threshold of fast P/T cycles that convert either type of graphite or hexagonal diamond into cubic-type diamond, and, region H-I-F denotes the path along which crystal hex-type graphite compressed in the c-direction at room temperature loses some graphite characteristics and acquires properties consistent with diamond-like polytypes, but reverses to graphite upon release of pressure" [26]. 20

2.7 Activation energies for some impurities in diamond. 22

2.8 Schematic representation of an elastic collision, in a laboratory frame of reference, between a projectile atom of mass M_1 and a stationary target atom of mass M_2 [73]. 26

2.9 Dependence of the nuclear and electronic energy loss on the energy of the projectile where $E_2 < 5$ keV, $E_3 \sim 15$ keV and $E_4 \approx 2$ MeV [11]. 31

2.10 The relationship between the projected range R_p and the total ion path R [81]. 32

2.11 Two dimensional Gaussian of the stopped atom distribution [82]. . . . 33

2.12 Example of typical defects by ion implantation [11]. 35
2.13 Structure of the <100>-split interstitial, showing the two atoms (in red) forming the interstitial pair, and their neighbours (in blue) [88]. . 36
2.14 Model depicting the diamond lattice. The panel on the left hand side shows a <110> direction, while the right hand side one shows the diamond lattice viewed along a random direction [95]. 38

3.1 Photograph of a diamond saw [97]. 40
3.2 Photograph of three pairs of 110 flakes of HPHT diamonds of $\sim$ half mm thickness. 41
3.3 A schematic diagram of a simplified set up used for the mechanical polishing of diamond surfaces [101]. 43
3.4 A photograph of thin diamond holder. 46
3.5 A schematic diagram of the model 200-20A2F Ion Implanter [113]. . . 50
3.6 Horizontal Split Tube Furnace. 54
3.7 Schematic diagram of the quartz tube. Some argon flows continuously out of the entry funnel, preventing the ingress of air 55
3.8 Scanning electron microscope (SEM) images of the cross-sectional ion milled diamond TEM sample. TEM investigations were carried out at the edge of the hole at the diamond/diamond interface. 56
3.9 A schematic illustration of an ion-beam thinning device [121]. 57
3.10 Stages in making cross-sectional TEM samples using the lift-out method. (A) The area of interest has been marked. (B) A Pt bar is deposited to protect this area from the Ga beam. (C,D) The two trenches (FIB boxes) are cut. (E) The bottom and sides of the slice are (final) cut. (F) The TEM specimen is extracted and polished after welding it onto the TEM specimen grid [122]. 59

3.11 Schematic drawing of a 3 mm diameter half-ring, used for mounting a thin TEM specimen lamella in the lift-out method [123]. 60
3.12 Illustration of the vibrational energy level transitions, induced by a photon of energy hν_0, redrawn after [40]. 66
3.13 Schematic diagram of the Jobin-Yvon T64000 spectrograph showing the beam path. From Jobin-Yvon T6000 Raman Spectrograph Instructional manual. 68
3.14 A block diagram of a TEM [135]. 72
3.15 Schematic diagram of the electron scattering processes [123]. 74
3.16 Schematic diagram of the geometry of a selected area diffraction [122]. 76

4.1 A SRIM-2008 derived damage density produced by the carbon ion multi-implantation into diamond whose parameters are given in Table 3.1 and calculated for a total fluence of $7\times\ 10^{15}$ ions cm^{-2}. 81
4.2 Cross-sectional bright-field TEM image of unimplanted type Ib HPHT synthetic diamond. The surface region of the diamond contains a high concentration of ripples. A two-beam diffraction condition was used to record the image. 83
4.3 (a) Cross-sectional bright-field TEM images of etched C^+-implanted diamond to a low fluence of 5×10^{15} ions cm^{-2} and annealed at 1600K and (b) Cross-sectional bright-field TEM images of etched C^+-as-implanted diamond to a high fluence of $6\times\ 10^{15}$ ions cm^{-2} and unannealed or rather warmed to room temperature. The corresponding selected area diffraction patterns are shown in the inserts. The implanted surfaces are indicated by the arrows. The white line (fringe) through the arrowhead of Figure 4.3 (a) is a result of an out-focus image. Two-beam diffraction conditions were used for both images. 84

4.4 Cross-sectional bright-field TEM micrograph of unetched C^+-implanted diamond to a fluence of 1×10^{15} ions cm^{-2} and rapidly annealed at 1600 K (CIRA) with corresponding selected area diffraction pattern. The sample has a wedge shaped edge as a result of ion milling and therefore show a number of thickness fringes close to the edge. 85

4.5 Cross-sectional bright-field TEM micrograph of unetched C^+-implanted diamond to a fluence of 1×10^{15} ions cm^{-2} with corresponding selected area diffraction pattern. This is the same sample as in Fig. 4.4 but viewed at a different position. The sample has a thin region produced by ion beam thinning, showing - defects in the form of fringes close to the edge. The fringes consist of stacking faults and curved dark lines most likely caused by the argon ion milling process. 86

4.6 (a) Cross-sectional bright-field TEM micrograph of unetched C^+-implanted diamond to a fluence of 7×10^{15} ions cm^{-2} at liquid nitrogen temperature and rapidly annealed at 1600 K with SAD patterns from the implanted layer (b) and diamond substrate (c). The dark defect contrast at the interface region between the amorphous implanted layer and diamond substrate is due to the implantation damage at the tail of the projected ion range. The SAD pattern (b) from the amorphous implanted layer exhibits the 002 arcs of graphite. The SAD pattern of the substrate in (c) shows the 111 reflections of diamond. 87

4.7 Bright-field TEM micrographs of unimplanted diamonds: (a) unimplanted synthetic HPHT diamond with corresponding selected area diffraction pattern in the insert. No extended defects are visible and the diffraction pattern spots are sharp. (b) Unimplanted natural diamond recorded in a thin region of the foil. A high density of platelets is visible. No dislocations are present. The broad dark lines in the image are bend contours and thickness fringes. 89

4.8 Bright-field TEM micrographs of unimplanted natural diamond (type Ia) with corresponding selected area diffraction patterns. A high density of platelets on {100} planes, showing the typical contrast of both edge-on and inclined platelets, is visible. The operating reflections are $\mathbf{g} = 111$ in (a) and $\mathbf{g} = 220$ in (b) with the electron beam along the <110> direction. 90

4.9 Cross-sectional bright-field micrograph of unetched C^+-as-implanted diamond (HPHT, type Ib) to a fluence of 7×10^{15} ions cm^{-2} showing an amorphous region 80.3 nm thick at a depth of about 130 nm. . . . 92

4.10 A SRIM-2008 derived damage density of C^+-implanted diamond at 150 keV to a high fluence of 7×10^{15} ions cm^{-2}. 93

4.11 Cross-sectional bright-field TEM micrographs of unetched C^+-implanted diamond to a low fluence of 1×10^{15} ions cm^{-2} and annealed at 1600 K with corresponding selected area diffraction pattern in the insert. The SAD (Selected Area Diffraction) pattern shows the 110 reflections of diamond. 95

4.12 Cross-sectional bright-field TEM micrographs of unetched C^+-implanted diamond to a fluence of 1×10^{15} ions cm^{-2} and annealed at 1600 K beyond the implanted range. The magnified image in (b) is an enlarged image extracted from middle of image (a), for clarity. A high density of loops on inclined {111} planes and platelets on {100} planes are visible. The electron beam is along the <111> direction. 95

4.13 Cross-sectional bright-field TEM micrographs of etched C^+-implanted diamond (a) to a fluence of 6×10^{15} ions cm^{-2} warmed to room temperature then annealed at 1600 K and (b) implanted to a fluence of 2.5×10^{15} ions cm^{-2} and rapidly annealed at 1600 K. 96

4.14 (a) Bright-field TEM micrograph of unetched C^+-implanted diamond (HPHT, type Ib) with high fluence of 7×10^{15} ions cm^{-2} and annealed at 1600 K. (b) EELS spectrum image map- obtained by using the $\pi^\star$ peak (284.1-289.9 eV), corresponding to the (sp^2), in the EELS spectrum of the implanted layer. 97

4.15 (a) Core EELS spectrum acquired from diamond substrate, away from the implanted layer. (b) Core EELS spectrum acquired from C^+-as-implanted diamond to a fluence of 7×10^{15} ions cm^{-2} at 150 keV, room temperature. 98

4.16 Core EELS spectrum acquired from C^+-implanted diamond to a fluence of 1×10^{15} ions cm^{-2} and annealed at 1600 K. 99

4.17 (a) EEL Spectrum acquired from bulk diamond (un-implanted) and annealed at 1600 K. The EELS spectrum above indicates the crystalline structure of diamond. (b) EEL Spectrum of the carbon K-edge acquired from C^+-implanted diamond layer to a high fluence of 7×10^{15} ions cm^{-2} and annealed at 1600 K. A pre-edge peak is assigned to the transition from the 1s core level to antibonding $\pi^\star$ levels above the Fermi level. 100

4.18 (a) High-resolution TEM images of C^+-implanted diamond to a high fluence of 7×10^{15} ions cm^{-2} and annealed at 1600 K. Insert: Corresponding selected area diffraction (SAD) pattern. The SAD pattern exhibits the 002 arcs of graphite. (b) Enlarged HRTEM image acquired across the implanted region. 101

4.19 High-resolution TEM images of the interface between the implanted layer and diamond substrate. Diamond crystallites (D), interspersed between regions of amorphous carbon (A) and partially graphitized carbon (G), are visible. The arrowed region shows lattice images of extended defects. The selected area diffraction pattern corresponds to the diamond substrate. The SAD pattern of the substrate shows the 111 reflections of diamond. 102
4.20 Raman spectrum of unimplanted HPHT synthetic type Ib diamond. . 103
4.21 Raman spectrum of unimplanted natural Ia diamond. 104
4.22 Raman spectrum of ion-beam thinned (IBT)/TEM analysed diamond. The Raman spectrum was taken from regions near the perforation, that is, electron transparent regions 105
4.23 Raman spectrum of unetched C^+-as-implanted diamond at room temperature, to a fluence of 7×10^{15} ions cm^{-2} (close to the edge of the perforated hole). 106
4.24 Schematic diagram, not to scale, showing cross-sectional geometry of ion-implantation radiation damage in diamond, redrawn after [151]. The thickness of the diamond is 40 μm while the width of the implanted diamond (edge) is 0.25 μm. 107
4.25 Raman spectrum of unetched C^+-implanted diamond (HPHT type Ib) at liquid nitrogen temperature with low fluence of 2.5×10^{15} ions cm^{-2} and rapidly annealed at 1600 K. A weak D band and a broad G peak are observed from carbon contamination. The Raman spectrum was acquired after the CIRA process, i.e. before glueing and milling. . . . 108

4.26 Raman spectrum of unetched C^+-implanted diamond (HPHT type Ib) at liquid nitrogen temperature with high fluence of 7×10^{15} ions cm^{-2} and rapidly annealed at 1600 K. Sharps D and G peaks are visible. The Raman spectrum was acquired after the CIRA process, i.e. before glueing and milling. 109

List of Tables

2.1 Mechanical, thermal, optical and electronic properties of graphite. . . 10

2.2 Comparison of major properties of amorphous carbons with those of reference materials diamond and graphite. The single most important parameter determining amorphous carbon properties is the fraction of tetrahedrally bonded f(sp^3) carbon. 12

2.3 Auxiliary properties of diamond 15

2.4 Auxiliary properties of diamond (continued) 16

2.5 The types and subtypes of diamond, with their main defects. 18

2.6 Intrinsic/extrinsic point defects in natural and HPHT diamond and their known properties. 37

3.1 Implantation parameters: Fractional fluence at the different energies. 46

3.2 Detailed implantation parameters. 47

Chapter 1

Introduction

1.1 Motivation

Diamond with its outstanding and unique physical properties offers the opportunity to be used as semiconductor material in future device technologies. Promising applications are, among others, high speed and high-power electronic devices working under extreme conditions, such as high temperature and harsh chemical environments. With respect to electronic applications, a controlled doping of the material is necessary which is preferably done by ion implantation. The ion implantation technique allows incorporation of foreign atoms at defined depths and with controlled spatial distribution which is not achievable with other methods. However, the ion implantation process is always connected with the formation of defects which compensate and trap charge carriers thus degrading the electrical behaviour. It is therefore essential to understand the nature of defects produced under various implantation conditions.

The development of diamond electronic devices will be effective if and only if diamond can be doped both p- and n-type. In this regard, while p-type doping has been achieved where boron is an effective, reliable and controllable acceptor which fits well into the diamond lattice; n-type doping of diamond has been rather problematical over the last couple of decades. Previous studies involving the ion implantation

damage in annealed diamond in the past have focused on the macroscopic changes within the damaged diamond. Few microscopic studies [1] on the nature of radiation damage, to our knowledge, have been attempted until now, at least for the radiation produced by sub-MeV multi-implantations followed by rapid annealing. This study thus aims to fill this gap by using detailed transmission electron microscopy (TEM) as our main investigation technique.

It is important to mention that although a lot of work involving radiation-induced effects in diamond using various characterization techniques has been carried out for almost half a century [2, 3], even plan-view transmission electron microscopy studies on the evolution of the implantation damage in annealed diamond are scarce [4, 5, 6, 7, 8], thin specimen preparation being clearly a major stumbling-block [9].

It is known that high fluence irradiation for single energy implantations, that is, above a certain critical damage threshold of fluence D_c, in covalently bonded solids usually results in amorphization [10]. For instance, the implanted layer in silicon amorphizes and subsequent post-implantation annealing recrystallises the amorphous layer and 'drives in' the dopant into electronically substitutional sites. In contrast, for diamond a rearrangement of the bonds broken by the irradiation into an sp^2-bonded structure assimilable to an amorphous structure takes place [11]. It has been shown that below D_c, annealing restores the crystalline order, while above it, an etchable form of sp^2-bonded carbon layer is formed. The critical damage threshold at which this process occurs, for room temperature implants, has been estimated to be 1×10^{22} vac/cm^3, independent of ion species or implantation energies [12]. However, Fairchild et al. [13] have postulated the damage threshold to be larger than 1×10^{22} vac/cm^3 for high-energy implantations whose damage is buried below the surface. For high energy implantations $>$ 1 MeV, recent studies [6, 14] have found it to be $6\pm3\times10^{22}$ vac/cm^3. In this study, the CIRA (Cold Implant Rapid Anneal) technique was used and it involved multiple implantations where the total implanted fluence was spread over a range of energies (50-150 keV) and fluences. For the conditions used (multi-

implantations and single energy implantation), the threshold damage between 5 $\times 10^{22}$ vac/cm^3 and 6 $\times 10^{22}$ vac/cm^3 is obtained as determined by SRIM (See Fig 4.10 for instance) which is almost six times higher than the known critical threshold for keV single energy implantations.

Raman spectroscopy studies have been carried out by many researchers [15, 1, 16] to study the nature of radiation damage in ion-implanted and annealed diamond within the MeV range. These researchers reported that for low fluence implantations the damaged diamond is rich in point defects and anneals back to diamond while high fluence implantations result in fully amorphised layers which transform to graphite upon heat treatment. Orwa et al. [1] reported also that for MeV ion irradiation high fluence implantations followed by annealing resulted in the restoration of the original diamond structure.

Interestingly, previous studies [4, 5, 13, 6] involving primarily transmission electron microscopy based techniques have tackled the investigation of the microstructure of ion-irradiated and annealed diamond produced by MeV energies. Lai et al [4] used Raman scattering, electron energy loss spectroscopy (EELS) and high resolution electron microscopy (HRTEM) to investigate the microstructure changes produced by high energy and high fluence ion irradiation conditions in diamond. Thin specimens in their study were obtained using electrochemical etching at the end of the range. They reported that the top cap layer retained most of its crystallinity for room temperature implantations. They also showed that the end-of-range damaged layer did not recrystallize as diamond as reported by Orwa et al. [1]. Instead they found that the end-of-range damaged layer relaxed into a mixture of graphitic carbon and i-carbon, that is, a cubic structure of lattice parameter $a_0 \sim 4.25$ Å, after annealing at 600 ^{0}C. Hickey et al. [5] studied the implant damage in single crystal HPHT(High-pressure, high-temperature) diamond using the Focused Ion Beam (FIB)-SEM lift out method to get electron transparent thin specimens. They reported to have implanted HPHT diamonds with Si^+ at an energy of 1 MeV and at temperatures of 30 ^{0}C using

a fluence of 1×10^{15} ions cm^{-2} and annealing temperatures of 950 ^{0}C and 1050 ^{0}C. Post implantation annealing under an unusual flowing high-purity nitrogen (N_2) gas environment showed no signs of conversion either to an amorphous form of carbon or to graphite. Similarly, Fairchild et al. [13], in their search for the fabrication of ultrathin single-crystal diamond membranes, implanted type Ib HPHT diamonds at room temperature, using a low beam current of about 0.5 μA, high fluence of 5.0×10^{16} ions cm^{-2} and 1.70-2.00 MeV energy implants. They found that unetched/uncleaned as-implanted diamond amorphized, while the amorphized highly damaged region subsequently converted to graphite upon annealing. Also, in their follow-up studies [6] which involved the direct examination of defects in irradiated diamond by transmission electron microscopy using MeV energies, they reported that diamond transforms to an amorphous form of carbon when a critical threshold is surpassed. Then the amorphous carbon transforms to a moderately crystalline graphitic layer upon annealing for 24 h at 1350 ^{0}C.

Finally, T.E. Derry et al. [7] in their initial investigation of the ion implantation damage in annealed single crystal HPHT diamond using conventional ion milling to thin the sample down to electron transparency, and cross-section transmission electron microscopy to investigate the nature of the radiation damage produced by sub-MeV energies at low and high ion fluences, observed long dislocations threading into the bulk, much deeper than the expected damage depth, in the case of the lower fluences.

This study investigates the nature of the radiation damage generated within the collision cascades of multi-implantations of carbon ions in single-crystal diamond, spread over a range of energies in the keV range and using various total fluences with the Cold-Implantation-Rapid-Annealing (CIRA) routine, using cross-section transmission electron microscopy (CTEM, HRTEM and EELS) techniques and Raman spectroscopy. The iso-chemical ions were chosen for the sole purpose of restricting mainly the effects of implantation to radiation damage [17] as emphasized in this

study.

1.2 Thesis breakdown

Chapter 1 presents the motivation and the outline of this thesis.
Chapter 2 provides an overview of the theoretical background of this study. It gives a general review of the main allotropes of carbon, the physics of ion implantation, which includes the energy-loss mechanisms, the radiation damage and channelling.
Chapter 3 outlines the experimental details; this includes a thorough description of the specimen preparation and the theory of Raman spectroscopy and transmission electron microscopy. Chapter 4 deals with the analysis and the discussion of the results obtained from the radiation damage studies in diamond, while Chapter 5 summarizes the conclusion and gives recommendations for further work.

Chapter 2

Theoretical Background

2.1 Layout of the chapter

This chapter gives an overview of the theoretical background of this study. Section 2.2 focuses on the element C and gives in detail, some of the properties of graphite and amorphous carbon. Section 2.3 presents in-depth properties of diamond. Section 2.4 and section 2.5 discuss, respectively, the synthesis and some pertinent applications of diamond. Last but not least, this chapter ends with a brief description of the physics of ion implantation, radiation damage and channelling.

2.2 Carbon and its main allotropes

Carbon is considered as one of the most remarkable and important of the chemical elements, as it occurs naturally in three pure forms and in many compounds such as CO_2 or CH_4, to name a few. It is light and relatively small and this coupled with its ability to form single, double and triple bonding with itself and with other elements makes it exist in solid, liquid and gaseous phases. Furthermore, carbon is found in all living organisms and, as a result, it is the basis of all life on Earth and is also the basic building block of Organic Chemistry. The carbon atom has a ground-state configura-

tion of $1s^2 2s^2 2p^2$, i.e., the carbon atom has two core electrons, having opposite spins thus do not take part in any bonding. In addition, it has four valence electrons: the two 2s electrons have opposite spins while the 2p electrons have parallel spins; making the latter the only electrons available for bonding (an example of a divalent carbon is methylene). However, the carbon allotropes and the stable carbon compounds are not divalent but are rather tetravalent, that is, four valence electrons are available for bonding [18]. The tetravalency of carbon in the case of methane, as an example, is due to the hybridization[1] of the orbitals of the carbon atom, whereby one of the 2s electrons unpairs and gets promoted to the vacant $2p_z$ orbital. A carbon atom can undergo three different atomic hybrid configurations, i.e., sp^3, sp^2 and sp^1 shown in Fig. 2.1 [20]. When a carbon atom is tetrahedrally coordinated, as in diamond, its four valence electrons are each assigned to sp^3 orbitals, making a strong σ bond[2] to an adjacent atom [20]. When a carbon is trigonally coordinated, as in graphite, three of its valence electrons hybridise to form sp^2 orbitals, thus forming strong intra-layer σ covalent bonds with the neighbouring atoms. The fourth electron of the sp^2 atom lies in a π orbital with an axis normal to the bonding plane and forms weak π bonds, also called unsaturated bonding, with one or more neighbouring atoms [20, 21]. When a carbon is diagonally coordinated, as in acetylene, two of the four valence electrons hybridise to form sp^1 orbitals which form σ bonds and the other two electrons enter π orbitals in the y and z directions [21]. The crystal structure of hexagonal graphite consists of series of stacked parallel planes shown schematically in Fig. 2.2 [22]. As shown in Fig. 2.2, the ABAB stacking sequence[3] has an in-plane nearest-neighbour distance (inter-atomic distance within a layer) of 0.141 nm, an in-plane lattice parameter a_o of 0.246 nm, a c-axis parameter of 0.6708 nm and the interplanar separation (distance between individual planes in the graphite lattice) is $\frac{c}{2} \approx 0.335$ nm. In ad-

[1] mathematical process of replacing pure atomic orbitals for bonded atoms [19].

[2] a σ molecular orbital is formed by the lateral overlap of two sp hybrid orbitals while a π orbital is formed by the side to side overlap of the sp hybrid orbitals .

[3] atoms in alternate layers occupy equivalent positions [23].

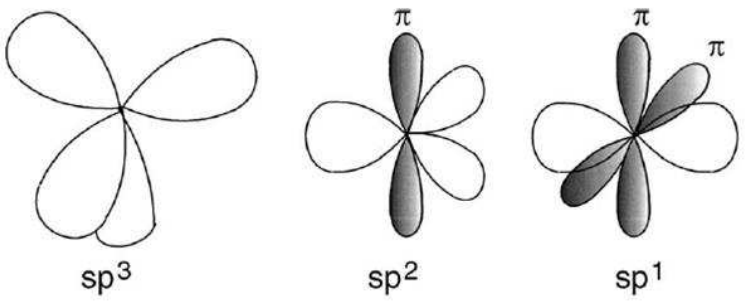

Figure 2.1: The sp^3, sp^2 and sp^1 hybridised bonding configurations. The unshaded and the shaded lobes denote strong bonds and weak bonds, respectively. sp^3, for example, signifies the overlap or combination of one s and 3p orbitals [21].

dition, the hexagonal graphite crystal is described by the D^4_{6h} or $P6_3$ space group symmetry and has four atoms per cell [11]. Note that there exists also a rhombohedral graphite [22], which is thermodynamically unstable, and whose crystal structure is described by the D^5_{3h}-R3m space group symmetry. It has the ABCABC stacking sequence (as in cubic diamond), an in-plane lattice parameter of 0.2256 nm, a c-axis lattice parameter of 1.0006 nm. Hexagonal graphite is the thermodynamically stable form of carbon at room temperature and ambient pressure, it is the stiffest material in nature, that is, it has the highest in-plane elastic modulus [11]. Graphite is opaque and can be etched off from diamond using a boiling solution of acids. The appropriate ratio is 3:4:1 of perchloric ($HClO_4$), sulphuric (H_2SO_4)and nitric (HNO_3) acids. Graphite is a semi-metal with a high conductivity and strength within the basal plane and low values along the c-axis [22, 21] (See Table 2.1). The other carbon allotropes include, among others, amorphous carbon, Lonsdaleite (hexagonal diamond), carbon nanotubes, fullerenes. Hexagonal diamond, known as Lonsdaleite, has the same den-

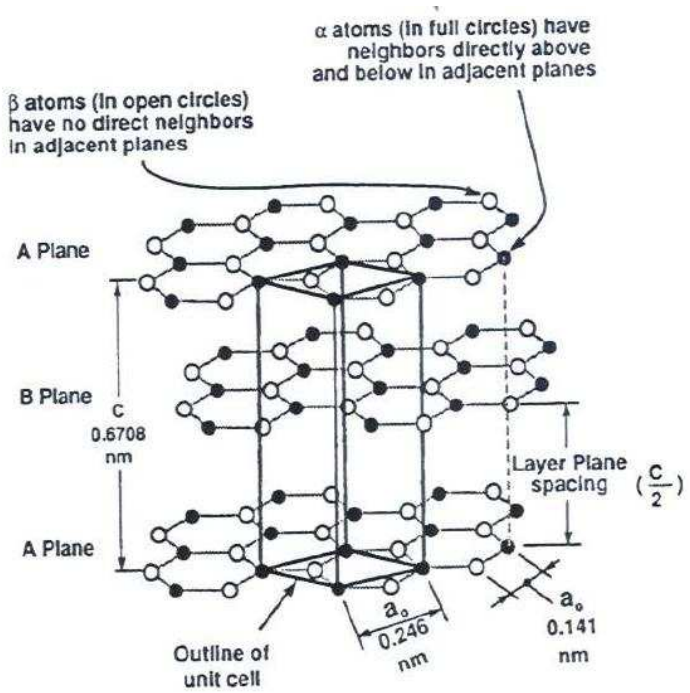

Figure 2.2: Crystal structure of graphite highlighting ABAB planar stacking arrangement and unit cell [23].

sity as cubic diamond whose properties are provided in detail in section 2.3 but they differ in the stacking order of the sp^3 bonded sheets, ABABAB-; that is the third layer superimposes the first layer [22, 24, 25]. Only amorphous carbon, graphite and diamond are relevant in our study and deserve further attention.

Amorphous carbon consists of a mixture of tetrahedral diamond-like (sp^3), trigonal planar graphite-like (sp^2) and even linear polymer-like (sp^1) bonding structures, with the possible presence of 60 at.% hydrogen and nitrogen [26, 27, 28]. The compositions of the various amorphous C-H alloy (nitrogen-free carbon) films are shown on a ternary phase diagram as in Fig. 2.3 [26].

Property	**ab (basal) value**	**c – axis value**
Lattice structure	Hexagonal	-
Pearson Symbol	hP_4 [29]	-
Strukturbericht designation	A9 [29]	-
Lattice constant (nm)	0.246	0.6708 [22]
Space group	$P6_3/mmc(D^4_{6h})$ [29]	-
Carbon-carbon bond distance (nm)	0.141 [22]	-
Density (300K)[g/cm^3]	2.26 [22]	-
Atomic number density (C atoms/cm^3)	1.14×10^{23} [30]	-
Debye temperature (K)	2500 [30]	950 [30]
Thermal conductivity (300K)[W/cm.K]	30 [30]	0.06 [30]
Specific heat (300K)[J/mol.K]	8.033-8.635 [22]	-
Binding energy [eV/C atom]	7.4 [30]	-
Bulk modulus (GPa)	286 [30]	-
Mohs hardness	0.5 [30]	9 [30]
Band gap (eV)	-0.04 [30]	-
Elastic modulus (GPa)	C_{11}=1060 [30]	C_{33}=36.5 [30]
compressibility (cm^2/dyn)	2.98×10^{-12} [30]	-
Carrier density (10^{18}/cm^{3}at 4K)	5 [30]	-
Electron mobility (cm^2/V.s)	20000 [30]	100 [30]
Hole mobility (cm^2/V.s)	15000 [30]	90 [30]
Resistivity [Ω.cm]	50×10^{-6} [30]	1 [30]
Melting point [K]	4450 [30]	-
Magnetic susceptibility[10^{-6}cm^3/g]	0.141 [30]	-
Highest Raman mode (cm^{-1})	1582 [11]	-
Dielectric constant (low ω at 300K)	3.0 [11]	5.0 [11]
Velocity of sound (cm/s)	$\sim2.63\times10^5$ [11]	2.63×10^5 [11]
Thermal expansion at 300K [/K]	- 1×10^{-6} [30]	$+29\times10^{-6}$ [30]

Table 2.1: Mechanical, thermal, optical and electronic properties of graphite.

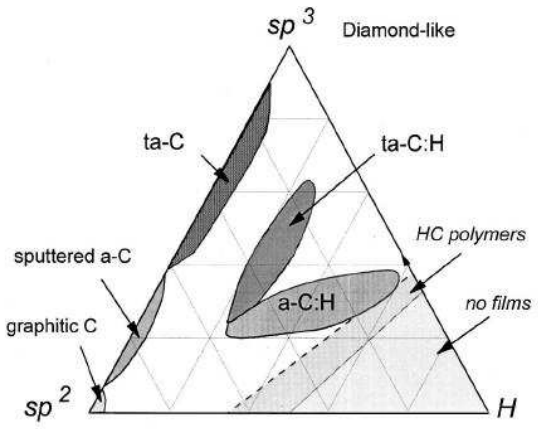

Figure 2.3: Ternary phase diagram of amorphous carbons. The three vertices correspond to diamond (sp^3), graphite (sp^2) and hydrocarbons [27].

In Fig. 2.3 of the ternary phase diagram, diamond-like carbon consists not only of a metastable form of amorphous carbon (a-C) but also consists of the hydrogenated alloys (a-C:H), containing a significant fraction of sp^3 bonds [20, 26].

The amorphous carbon (See Table 2.2 [26]) with highest sp^3 fraction (80-90%) are called tetrahedral amorphous carbon (ta-C) while the hydrogenated amorphous carbons (a-C:H) have small sp^3 fraction (40-60%), significant hydrogen levels, up to (30-50%) and a density less than that of graphite. Moreover, ta-C:H has up to 70% sp^3 and 30% hydrogen content. The ternary phase diagram (Fig. 2.3) shows a non-crystalline structure, that is, glassy carbon (graphitic carbon), which contains almost all sp^2 bonding and contains as well sp^2 layers in the form of ribbons [24]. It is also believed to be crystalline in two dimensions but amorphous in three dimensions [24]. The n(new)-diamond is a metastable, metallic form of carbon, with face-centred cubic structure, and with a lattice parameter similar to that of cubic diamond [31, 32].

	sp^3%	**H%**	**Density($g.cm^{-3}$)**	**Gap(eV)**	**Hardness (GPa)**	**Ref**
Diamond	100	0	3.515	5.47	100	[11]
Graphite	0	0	2.26	0	-	[22]
Glassy carbon	0	0	1.3-1.55	0.01	3	[33]
Evaporated C	0	0	1.9	0.4-0.7	3	[33]
Sputtered C	5	0	2.2	0.5	-	[34]
ta-C	80-88	0	3.1	2.5	80	[24, 35, 34]
a-C:H hard	40	30-40	1.6-2.2	1.1-1.7	10-20	[36]
a-C:H soft	60	40-50	1.2-1.6	1.7-4	10	[36]
ta-C:H	70	30	2.4	2.0-2.5	50	[37]

Table 2.2: Comparison of major properties of amorphous carbons with those of reference materials diamond and graphite. The single most important parameter determining amorphous carbon properties is the fraction of tetrahedrally bonded f(sp^3) carbon.

2.3 Properties of diamond

2.3.1 Crystal structure

Crystal structure is defined as the periodic arrangement of the atoms in the crystal. The description of the crystal structure can be done by associating with each lattice a group of atoms known as basis or motif units of the structure [38]. A lattice is a three dimensional, infinite array of points, the lattice points, each of which is surrounded in an identical way by neighbouring points, and which defines the basic repeating structure of the crystal. The diamond crystal structure consists of the face-centred cubic (fcc) (see Fig. 2.4 [39]), with a basis of atoms at (0,0,0) and $(\frac{1}{4}, \frac{1}{4}, \frac{1}{4})$, associated

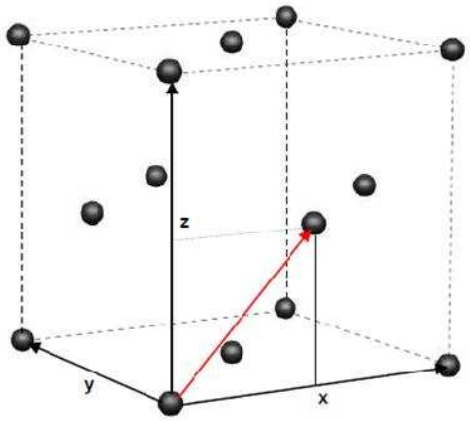

Figure 2.4: A typical representation of a face-centred cubic lattice, with lattice points represented by black spheres [40].

with lattices vectors of $(\frac{1}{2}, \frac{1}{2}, 0)$, $(\frac{1}{2}, 0, \frac{1}{2})$ and $(0, \frac{1}{2}, \frac{1}{2})$. The full diamond crystal lattice structure as shown in Fig. 2.5 [39, 40], is then obtained, with bases added at each point in the fcc lattice [39, 40]. The diamond structure has a highly symmetric space group O_h^7 or (Fd3m)[4] in international notation and can be viewed as two interpenetrating face-centred cubic structures offset by $(\frac{1}{4}, \frac{1}{4}, \frac{1}{4})a_0$ along the body diagonal, where a_0 is the lattice parameter and has a value of 3.567Å, at room temperature and atmospheric pressure [22]. A few other quantities [39, 42] can be explicitly derived from the lattice parameter. The carbon-carbon bond distance is equal to one-quarter of the cubic body diagonal, that is, $\sqrt{3}/4a_3 = \sqrt{3}/4 \times 3.567$Å$\approx$ 1.54Å. The conventional unit cell, which is the smallest volume exhibiting the symmetry of the lattice, contains eight atoms in total; each face atom is shared between two cells and each corner between eight, and the atomic number density is therefore d= $8/(3.567\times10^{-10})^3$ m^3 $\approx 1.763\times10^{29}$ atoms/m^3$\approx$ 1.763×10^{23} atoms/cm^3.

[4]The 'F' indicates that the structure is based on a face-centred (cubic) lattice ; d, 3 and m indicate the presence of a diamond glide plane, threefold rotation axis and a mirror plane respectively [41].

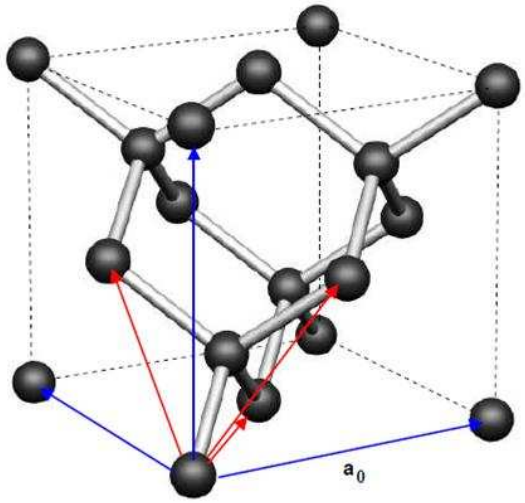

Figure 2.5: The diamond crystal lattice structure, with bases added at each point in the fcc lattice. The conventional unit cell vectors (x,y,z) are shown in blue while the primitive unit cell vectors ($V_1 = \frac{1}{2}\vec{i} + \frac{1}{2}\vec{j} + 0\vec{k}, V_2 = \frac{1}{2}\vec{i} + 0\vec{j} + \frac{1}{2}\vec{k}, V_3 = 0\vec{i} + \frac{1}{2}\vec{j} + \frac{1}{2}\vec{k}$ which define the minimum volume that can be translated to represent the diamond structure) are shown in red [40,41].

This atomic number density is the highest of any material at ambient pressure, thus making diamond the stiffest in three dimensions, hardest and least compressible of all substances [22]. The theoretical mass density for diamond is obtained by multiplying the atomic number density by the average atomic mass of the carbon atom, that is, d $= 1.763 \times 10^{29}$ atoms/m^3×(12.0107×1.66053×10^{-27}kg) $\approx$ 3516kg/m^3. Note that this theoretical value is slightly higher than the experimentally measured density (3515.2 kg/m ^{3} [22]) due to the presence of impurity atoms and crystal imperfections such as voids in real diamond samples. Each atom can be regarded as a sphere of radius one-eighth of the cubic body diagonal implying that the packing fraction[5] of the diamond structure is: $\frac{8\times 4/3\pi\times(\sqrt{3}/8a_0)^3}{a_0^3} = \sqrt{3\pi}/16 \approx 0.34$.

[5]The packing fraction is the fraction of space filled by spheres on each lattice point that are as large as they can be so as to touch but not overlap [40].

Property	**Value**
Lattice structure	cubic [29]
Pearson Symbol	CF8 [29]
Strukturbericht designation	A4 [29]
Lattice constant (nm)[300K]	0.35669 [29]
Space group	Fd3m-O_h^7 [29]
Carbon-carbon bond distance (nm)	0.15448 [22]
Density (300K)[g/cm^3]	3.515 [22]
Atomic number density (C atoms/cm^3)	1.763×10^{23}
Debye temperature (K)	2340 [22]
Thermal conductivity (300K)[W/cm.K]	$\sim$ 25 [30]
Specific heat (300K)[J/kg.K]	471.5 [29]
Mass of ^{12}C [kg]	$1.9926(47)\times10^{-26}$
Atomic weight of carbon [kg]	$1.9944(2)\times10^{-27}$
Bulk modulus (GPa)	440 [43]
Mohs hardness [N/mm^2(M-Mohs scale)]	10 [29]
Coefficient of thermal linear expansion(300K)[10^{-6}K]	1.8 [29]
Heat of formation [kJ/mol(300K)]	714.4 [29]
Standard entropy [kJ/mol.K(300K)]	2.428 [30]
Standard enthalpy of formation [kJ/mol.K(300K)]	1.844 [30]
Indirect Bandgap (eV)	5.47 [11]
Direct Bandgap (eV)	7.3 [42]
Breakddown voltage [kV/mm]	500 [29]
Elastic modulus (GPa)	700-1200 [30]
Volume compressibility (10^{-10}m^2/N)	18 [30]
Young's modulus [GPa]	910-1250 [30]
Electron mobility (cm^2/V.s)	1800 [29]
Hole mobility (cm^2/V.s)	1400 [29]

Table 2.3: Auxiliary properties of diamond

.

Resistivity [Ω.m].Type I and most Type II	10^{18} [30]
Resistivity [Ω.m].Type IIb	10^{3}-10^{5} [30]
Melting point [K]	4500 [11]
Poisson ratio	0.10-0.16 [30]
Raman frequency (first order) (cm^{-1})	$\sim$ 1332 [11]
Static Dielectric constant	5.7 [29]
Velocity of sound (cm/s)	$\sim 1.96\times10^{5}$ [11]
Refractive index	2.417 [44]
Knoop hardness [kg/mm^2]	5700-10400(overall)[30]
Breakdown field [V/cm]	10^{7} [11]
Saturated electron velocity [10^{7} cm/s]	2.7 [30]
Dielectric strength [V/cm]	10^{6} [30]

Table 2.4: Auxiliary properties of diamond (continued)

.

2.3.2 Classification of diamonds

Diamonds are classified according to the content and type of the dominant defect they present. Type I diamonds contain high concentration of nitrogen impurities, while type II diamonds are almost N-free or have little nitrogen impurities. Type I diamonds are subclassified into type Ia and type Ib dependent on the aggregation of nitrogen atoms in the lattice.

• Type Ia, which contains nitrogen in non-paramagnetic aggregated form ($\sim$ 2500 atomic ppm), is the most abundant in nature, i.e., more than 95% of all natural diamonds belong to this type [45, 46, 47]. A finer classification includes type IaA and Type IaB and type IaA/B. In type IaA diamonds, nitrogen exists in the form of nearest-neigbour substitutional pairs, that is, $([N_s - N_s]^0)$, the A centre, while in type

IaB nitrogen occurs in the form of four substitutional nitrogen atoms in a tetrahedral arrangement surrounding a vacancy, that is, ($[4N_s - V]^0$), the B centre [46, 47]. Type IaA/B diamonds not only contain A and B centres but also they have a group of three substitutional nitrogen around a vacancy, i.e., the N_3 centre. Furthermore, diamonds containing platelets (B'-defects) are known as IaB' [48]; type IaB' regular refers to diamonds with a quite high content of B'-defects; type IaB' irregular are diamonds that have a low content of B'-defects, while type IaB diamonds without B'-defects differ from type IaB diamonds which do not contain platelets [49, 50, 51].

• Type Ib diamonds contain single-substitutional nitrogen donor centres (N_s or C centre), with a concentration up to around 500 ppm. Type Ib diamonds are very rare in nature ($\sim$ 0.1 % of all diamonds), but most high-pressure, high-temperature (HPHT) and many chemical vapor deposition (CVD) diamonds belong to this category [46]. Type Ib diamonds have usually a deep golden-yellow colour which tends to be greenish when they contain a high density of substitutional nitrogen [45]. Note that unfamiliar Type Ic diamonds have been referred to as those which contain a high concentration of dislocations. Although labelled as Ic, this type of diamond is not related to nitrogen [48].

Type II diamonds are subclassified as type IIa and IIb and have a very low concentration of nitrogen.

• Type IIa diamonds have a concentration of nitrogen of about 1-2 atomic ppm. Type IIa diamonds are referred to as pure stones, but with about 0.25 ppm boron and are optically the most transparent of all diamonds [46].

• Type IIb diamonds are extremely rare in nature and are p-type semiconductors due to the presence of uncompensated single-substitutional boron acceptors (B_s^0) [47].

Table 2.5 taken from [39] summarizes the diamond classification.

Type	**Subtype**	**N concentration (atom cm^{-3})**	**Defect Centres**
I	aA	$\sim 10^{20}$	A
I	aB	$\sim 10^{20}$	N3, H3, B
I	b	$\sim 10^{20}$	C
II	a	$< 10^{17}$	Dislocations
II	b	$< 10^{17}$	Boron

Table 2.5: The types and subtypes of diamond, with their main defects.

2.4 HPHT diamond synthesis

The interconversion between diamond and graphite is not possible under ordinary conditions due to the existence of a large energy barrier between them. Hence, the only way to synthesise diamond from graphite or glassy carbon is to have recourse to the high-pressure, high-temperature method which attempts to reproduce the conditions under which natural diamonds are formed [52, 53].

However, first attempts showed that the transformation of graphite, within the diamond stable region, applying simply HPHT synthesis was not good enough because the yield decreased with increasing temperature. Fortunately, the use of some catalyst/solvent during the process helped to dissolve carbon faster and transport it to the growing surface under lower HPHT conditions, that is, between 5 GPa and 10 GPa, in the temperature range $\sim 1300^0$C-2300^0C (see Fig 2.6 [25]). The samples (large type Ib yellow diamond) in this study have been grown using iron/cobalt solvent/catalyst and this involves "indirect heating" with the carbon source, separated from the solvent and the seed under a growth temperature lying between the melting point of the solvent/catalyst/carbon system and the diamond-graphite equilibrium temperature [54]. Hence, the existence of a temperature gradient between the carbon source and the seed drives carbon from the higher temperature region to the cooler seeded region where it precipitates homoepitaxially on the diamond seed [54, 55].

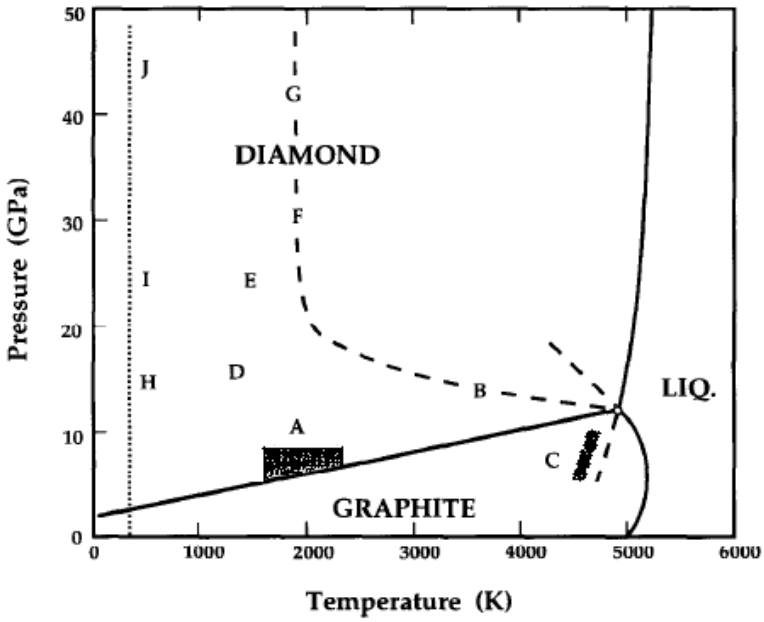

Figure 2.6: Pressure/Temperature phase and transition diagram for carbon. Letters A, B, C, D, E, F and G show different regions within the phase diagram. The solid lines represent the equilibrium phase boundaries. Region A is where the commercial synthesis of diamond from graphite by catalysis is feasible. "Region B is the P/T threshold of very fast (less than 1ms) solid-solid transformation of graphite to diamond, Region C is the P/T threshold of very fast reversible phase transformation of diamond to graphite, region D is the region where single crystal hexagonal graphite transforms to retrieval hexagonal-type diamond, region E marks the upper ends of shock compression/quench cycles that convert hex-type graphite particles to hex-type diamond, region F designates the upper ends of shock compression/quench cycles that convert hex-type graphite to cubic-type diamond, region B-F-G indicates the threshold of fast P/T cycles that convert either type of graphite or hexagonal diamond into cubic-type diamond, and, region H-I-F denotes the path along which crystal hex-type graphite compressed in the c-direction at room temperature loses some graphite characteristics and acquires properties consistent with diamond-like polytypes, but reverses to graphite upon release of pressure" [26].

2.5 Application of diamond

2.5.1 The doping of diamond

The development of diamond electronic devices will be effective if and only if diamond can be doped both p- and n-type. In order to achieve this, dopants must satisfy two conditions, that is, they must be soluble and have shallow electron energy levels [20]. In this regard, while p-type doping has been achieved where boron is an effective, reliable and controllable acceptor which fits well into the diamond lattice; n-type doping of diamond has been rather problematical over the last couple of decades. Indeed, while substitutional boron atoms form acceptor centres in diamond situated at 0.37 eV above the valence band maximum, substitutional nitrogen atoms form donor centres at 1.7 eV below the conduction band minimum [56], which is too deep to provide an adequate supply of electrons within the conduction band, at room temperature [57]. Moreover, the only well established donor in diamond which can be used technologically is substitutional phosphorus, with no shallow levels for most practical applications [58, 59, 60]. Furthermore, phosphorus donors with a range of activation energies varying from 0.4 to 0.62 eV have been measured [61, 59, 62] and further studies determined that phosphorus donors have an activation energy of 0.63 eV [63]. Fig. 2.7 [64] shows that phosphorus donors lie shallower than the nitrogen donors (1.7 eV), thus, diamond electronic devices made out of it are still poor, at room temperature, most likely because phosphorus incorporation is characterized by distortions in the diamond lattice [65].

2.5.2 Other applications

Some other applications of diamond are as follows:

• The hardness of diamond (the hardest material known) has seen it being exploited in materials science as wear-resistant coating on other devices, abrasive, cutting and

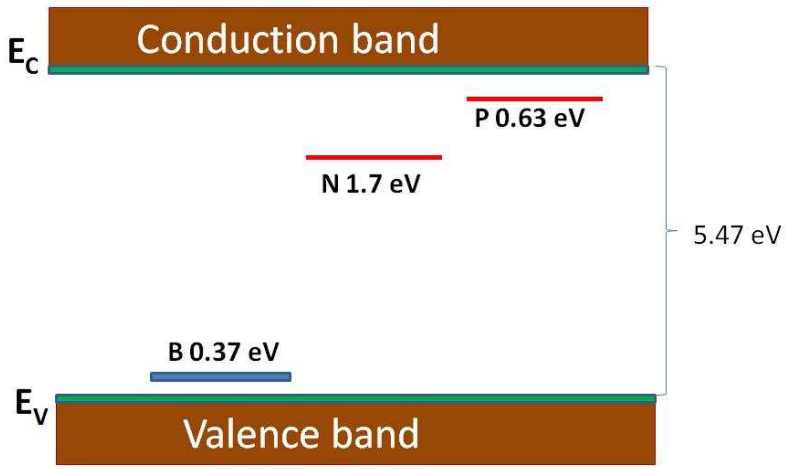

Figure 2.7: Activation energies for some impurities in diamond.

polishing tools, hardness indenter and pressure amplifiers to produce the highest static pressures known on earth [44]. In addition, the fact that diamond surfaces exhibit low friction against living tissue combined with its strong atomic bonding leads to sharper edges (one to two order of magnitude) than the finest steel edges. Thus diamond surgical blades are of the best quality, as the saying goes, "The diamond knife appears to cut epithelial cells rather than tearing them, as does the shearing action of the razor knife" [44].

• The high thermal conductivity, the high breakdown field and the high carrier mobilities of diamond are the ingredients of high-power, high frequency devices [66]. In addition, the high thermal conductivity and electric resistivity make diamond an ideal heat sink for high-power electronic devices.

• The high elastic constants of diamond can be exploited in surface acoustic wave (SAW) applications [66].

• The negative electron affinity (NEA) of diamond hydrogen-terminated surfaces allows emission of low-energy (cold) electrons and thus can be used as cold cathodes and electron field emitters, or field-effect transistors [66]. Note that electron affinity

refers to the minimum energy required to dislodge an electron from a material with negative electron affinity suggesting that an electron in the conduction band does not encounter any barrier when escaping into the vacuum [67].

• The radiation hardness and high breakdown field of diamond associated with its wide bandgap can be utilized to manufacture detectors for UV radiation, particularly in medical applications based on radiation dosimetry [66].

• The chemical inertness of diamond enables it to be applied in harsh environments such as in various electro-chemical applications [66].

• The optical applications include the use in robust optical windows transparent over a wide range of wavelengths ranging from UV to IR thanks to the optical transparency of pure diamond from the ultra-violet into the infrared and microwave regions of the electromagnetic spectrum [66].

2.6 Ion Implantation

2.6.1 Introduction

Ion implantation is a superb method for the doping of semiconductors in a wide variety of applications. It modifies the near surface properties of materials with accurate control of dopant composition and structural modification at any selected temperature not achievable using diffusion or growth methods [68, 69]. Particularly, the Cold Implantation Rapid Anneal (CIRA) scheme has been the most widely used to dope diamond with boron in a controlled manner by means of ion implantation [62]. However, ion implantation being a harsh, non-equilibrium method used to introduce atoms into a material [70], introduces disorder in the preexisting lattice atomic arrangement, known as radiation damage. This is responsible for trapping and compensating charge carriers thus degrading the electrical behaviour. Radiation damage can be repaired by applying suitable annealing in order to activate the dopant atoms

and reconstruct the lattice structure of the material [71, 72]. The method of introducing energetic ions into a target material requires a machine that generates and accelerates ion beams and steers them onto a target surface. A detailed description of such a machine, commonly known as an Ion Implanter, is given in the section 3.3.2.

2.6.2 Energy-loss mechanisms

1. Introduction

The following compilation on the energy-loss mechanisms is mainly based on the texts of Dresselhaus et al. [11] and Feldman and Mayer [73]. The passage of energetic ions through any solid results in an interaction with both the atomic (nuclear) and electronic clouds. Once an energetic ion is implanted in any solid, it gradually loses its kinetic energy via scattering events due to the Coulombic interaction of the ion with both the atoms and electrons of the target. In general, the slowing down process in a solid can be divided into two dominant independent processes, namely the nuclear energy loss and electronic energy loss components.

The former process is dominated by elastic collisions between ions and the target atoms, and results in significant deviation in the projectile trajectory. The latter process consists of inelastic interactions of incident ions and electrons of the target via ionisation and excitation, and results in no change in the projectile trajectory [74, 75]. Furthermore, the ion-solid interaction is generally treated in terms of "stopping power", described as the energy loss of the ion per unit path length or defined as the energy, dE, lost by an ion traversing a distance dx. The stopping power is given by

$$\frac{dE}{dx} = N \int T d\sigma \tag{2.1}$$

where:

- $d\sigma$ represents the collision cross section,
- T is the energy lost by the ion in the course of the event,

• N is the density of scattering centers of the host material.

The stopping cross section, ε, can be derived from Eqn. 2.1 as

$$\varepsilon = \frac{1}{N}\frac{dE}{dx} = \int T d\sigma \tag{2.2}$$

2. Nuclear energy loss

In the ion-nucleus interaction, nuclear stopping is caused by a collision between two atoms, that is, the positively charged ions are Coulombically repelled by the positive cores of the target lattice atoms, and can be described by classical kinematics [73] where conservation of energy and momentum apply. Fig. 2.8 [73] shows a schematic representation of an elastic collision, in a laboratory frame of reference, between a projectile atom of mass M_1 and a target atom which is initially at rest.

• Before the collision: The projectile atom has mass, velocity, and energy M_1, υ and E_0; the target atom has mass M_2.

• After collision: The projectile and the target atoms have velocities and energies υ_1, E_1 and υ_2, E_2, respectively. θ and ϕ are scattering and recoil angle, respectively.

The expressions for the conservation of energy and momentum parallel and perpendicular to the direction of incidence are given by Eqns. 2.3, 2.4 and 2.5 :

$$\frac{1}{2}M_1\upsilon^2 = \frac{1}{2}M_1\upsilon_1^2 + \frac{1}{2}M_2\upsilon_2^2 \tag{2.3}$$

$$M_1\upsilon = M_1\upsilon_1\cos\theta + M_2\upsilon_2\cos\phi \tag{2.4}$$

$$0 = M_1\upsilon_1\sin\theta - M_2\upsilon_2\cos\phi \tag{2.5}$$

Solving the system of Eqns. 2.3, 2.4 and 2.5 gives Eqn. 2.6, the ratio of particle

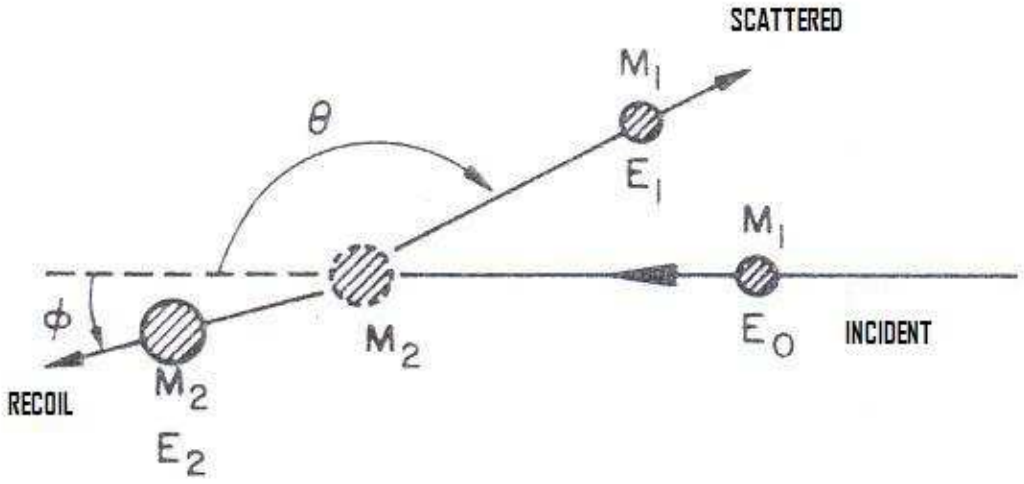

Figure 2.8: Schematic representation of an elastic collision, in a laboratory frame of reference, between a projectile atom of mass M_1 and a stationary target atom of mass M_2 [73].

velocities:

$$\frac{\upsilon_1}{\upsilon} = \frac{[\pm(M_2^2 - M_1^2 \sin^2\theta)^{\frac{1}{2}} + M_1 \cos\theta]}{M_1 + M_2} \tag{2.6}$$

For $M_1 < M_2$ (where the plus sign holds), the ratio of the projectile energies is given by Eqn. 2.7, that is,

$$\frac{E_1}{E_0} = \left[\frac{(M_2^2 - M_1^2 \sin^2\theta)^{\frac{1}{2}} + M_1 \cos\theta}{M_1 + M_2}\right]^2 \tag{2.7}$$

The energy ratio κ is called the kinematic factor and is given by

$$\kappa = \left[\frac{(M_2^2 - M_1^2 \sin^2\theta)^{\frac{1}{2}} + M_1 \cos\theta}{M_1 + M_2}\right]^2, \tag{2.8}$$

where the scattering angle θ is given by

$$\cos\theta = \frac{1 - (1 + \frac{M_2}{M_1})(\frac{T}{2E_0})}{\sqrt{1 - \frac{T}{E_0}}}. \tag{2.9}$$

Thus, the energies of the projectile before and after scattering , E_0 and E_1, respectively are related by

$$E_1 = \kappa E_0 \tag{2.10}$$

and

$$T = E_0 - E_1 \tag{2.11}$$

is the recoil energy transferred from the projectile to the target. A general expression of the recoil energy E_2, transferred from the projectile to the target is given by

$$T = \frac{4M_1M_2}{(M_1 + M_2)^2} E_0 \cos^2\phi; \qquad \phi < \frac{\pi}{2} \tag{2.12}$$

The maximum energy transferred, which occurs at θ=0 when the target mass is less than the projectile mass, and at θ=π when the target is more massive than the projectile, is thus given by

$$T = \frac{4M_1M_2}{(M_1 + M_2)^2} E_0 \tag{2.13}$$

It is easy to derive from Eqns. 2.9 and 2.12 useful relationships of the recoil energy transferred from the projectile and the scattering and the recoil angles, in the special case of equal incident and target atom masses (as we will be implanting carbon ions into diamond). The three useful relationships are as follows:

$$T = E_0 \cos^2\phi \tag{2.14}$$

$$\cos\phi = \left(\frac{E_2}{E_0}\right)^{1/2} \tag{2.15}$$

$$\cos\theta = \left(\frac{E_1}{E_0}\right)^{1/2} \tag{2.16}$$

In addition,

$$\tan\phi = \tan\theta/2, or \quad \phi = \theta/2 \tag{2.17}$$

For simplicity [76], the cross section of the ion-nucleus interaction is given by Eqn. 2.18 of the Simple Rutherford Scattering, i.e.:

$$\sigma(\theta) = \left(\frac{Z_1 Z_2}{E}\right)^2 \frac{4}{\sin^4\theta} \frac{\left\{\left[1 - \left(\left(\frac{M_1}{M_2}\right) sin\theta\right)^2\right]^{1/2} + \cos\theta\right\}^2}{\left[1 - \left(\left(\frac{M_1}{M_2}\sin\theta\right)^2\right]^{1/2}\right.} \tag{2.18}$$

For $M_1 \ll M_2$, Eqn. 2.18 can be expressed in terms of a power series, as follows:

$$\sigma(\theta) = \left(\frac{Z_1 Z_2}{E}\right)^2 \left[\sin^{-4}(\theta/2) - 2\left(\frac{M_1}{M_2}\right)^2 + ...\right] \tag{2.19}$$

It is important to mention that the cross section of Eqn. 2.19 decreases strongly with increasing scattering angle ($\sin^{-4}\theta/2$) and it increases with decreasing projectile energy (E^{-2}), thus predicting significant nuclear scattering in the vicinity of the projected range R_p. In the ion-nucleus interaction, the energies lost by the incident ions are transferred to the target atoms that are subsequently recoiled away from their lattice sites. If the recoil atoms have sufficient energies, meaning their energies are greater than the target atoms' displacement energy, then they may induce a series of collision cascades, prompting point and even line defect generation, called radiation damage. The radiation damage that follows ion implantation will be presented in more detail in section 2.8.3.

3. Electronic energy loss

The electronic stopping arises from interactions between the electrons associated with the incident ion and the electronic cloud of the target atom [73, 77]. In this study, we used a low energy regime, that is, the keV range, where electronic stopping can be said to be similar to a viscous drag force which is proportional to the ion

velocity and is given by the Thomas-Fermi treatment as

$$\left(\frac{dE}{dx}\right)_e = \frac{\xi_e \times 8\pi e^2 a_0 Z_1 Z_2}{\left(Z_1^{2/3} + Z_2^{2/3}\right)} \frac{\upsilon}{\upsilon_0} \tag{2.20}$$

where:

- υ is the velocity,
- υ_0 is the Bohr velocity ($Z_1 e^2/\hbar$),
- $a_0 = \left(\hbar^2/mc^2\right) \times 0.8853$, and
- $\xi_e \simeq Z_1^{1/6}$ (of order of 1-2).

Eqns. 2.20 can be rewritten in terms of scaling parameters (dimensionless parameters), ε (energy) and ρ (range) [78] as

$$\left(\frac{d\varepsilon}{d\rho}\right)_e = k\varepsilon^{1/2} \tag{2.21}$$

with

$$k \simeq \frac{0.079 Z_1^{1/6} Z_1^{1/2} Z_2^{1/2} \left(M_1 + M_2\right)^{3/2}}{\left(Z_1^{2/3} + Z_2^{2/3}\right)^{3/2} M_1^{3/2} M_2^{1/2}}$$

The dimensionless parameters for energy, ε, and range, ρ, are obtained using a screened coulomb potential [79] and are given by Eqn. 2.22 and Eqn. 2.23, respectively,

$$\varepsilon = E \frac{a M_2}{Z_1 Z_2 e^2 (M_1 + M_2)} \tag{2.22}$$

$$\rho = RN4\pi a^2 \frac{M_1 M_2}{\left(M_1 + M_2\right)^2} \tag{2.23}$$

where

- $a = a_0 \left(Z_1^{2/3} + Z_2^{2/3}\right)^{1/2}$
- Z_1 and Z_2 are the atomic numbers of the incident ion and the target ion respectively.
- N is the number of target atoms per unit volume.
- R is the total path length for an incident ion with initial energy E_0 slowing down in a target solid.

Note that the energy lost by the incident ion energy in this regime is dissipated through the electron cloud as acoustic phonons.

In the intermediate energy regime (1-10MeV), the electronic stopping reaches a maximum value then decreases with further increase in the incident energy. It is in this range where the ion velocities are comparable to those of the orbital electrons in the target atoms, thus leading to an enhancement in electronic energy loss due to exchange of electrons between the two [80].

For higher energy, that is, for incident energies greater than 10 MeV and for which the ion velocity is greater than that of the orbital electrons, electronic stopping is described by a quantum mechanical treatment, the so-called Bethe-Bloch formalism.

The intermediate and higher energy regions are not included in the present work as a maximum energy of 150 keV was used in all the implantations.

4. Dependence of the nuclear and electronic energy loss on the energy of the projectile

In this description of the energy dependence of nuclear and electronic energy loss, three important values of the critical energies, E_2, E_3 and E_4 are given in Fig. 2.9 [11] and they were calculated for the special case of the implantation of carbon into diamond which correspond to the irradiation conditions of this study.

In the low energy regime, nuclear stopping is dominant, it increases and reaches a maximum at energy $E_2 < 5$ keV then decreases to equal the electronic stopping power at energy $E_3 \sim 15$ keV. Electronic stopping power on the other hand, increases linearly with velocity over a very wide range [81] and reaches its maximum, outside the keV range, at energy $E_4 \approx 2$ MeV, and subsequently decreases as E^{-1} for energies greater than 2 MeV. This is well beyond the range used here (≤ 150 keV), as already mentioned.

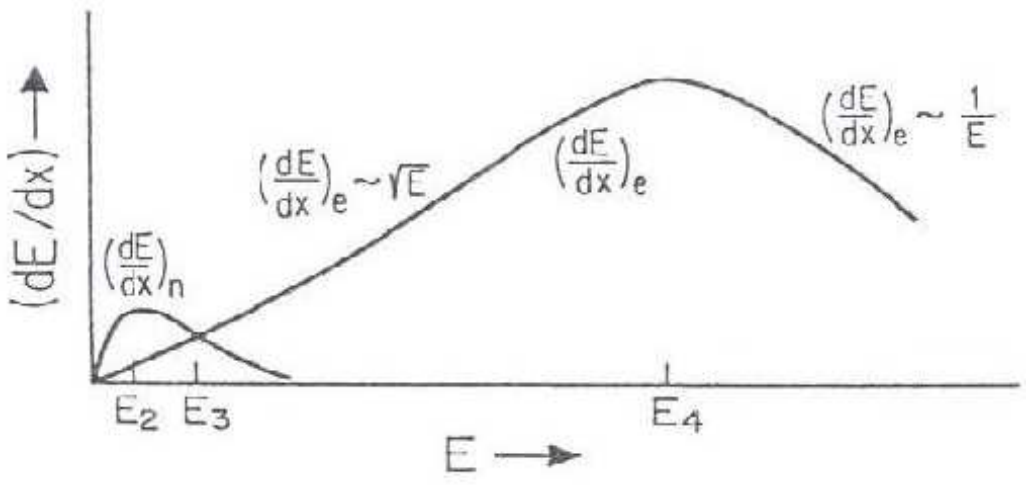

Figure 2.9: Dependence of the nuclear and electronic energy loss on the energy of the projectile where $E_2 < 5$ keV, $E_3 \sim 15$ keV and $E_4 \approx 2$ MeV [11].

5. Range and Gaussian distribution of implanted ions

The reciprocal integral of the energy loss defines the ion range R as

$$R = \int_{E_0}^{0} \frac{dE}{dE/dx} \tag{2.24}$$

where E_0 is the initial ion energy.

The ion range R is the total distance that the ion travels in coming to rest as shown in Fig. 2.10 [81] and the projected range R_p is the mean penetration depth of the ion normal to the surface. Generally, Eqn. 2.25 is a fair empirical correction (only for semiconductors) for a wide range of implantations [81].

$$\frac{R}{R_p} = 1 + \frac{M_2}{3M_1} \tag{2.25}$$

The slowing down of an ion in an amorphous or fine-grain solid polycrystalline is a statistical process, implying that the final locations of ions in that solid are also of statistical nature. Thus, in order to gain a simple picture of the implant profile, one may use a Gaussian approximation (see Fig.2.11 [82]) which gives the implant

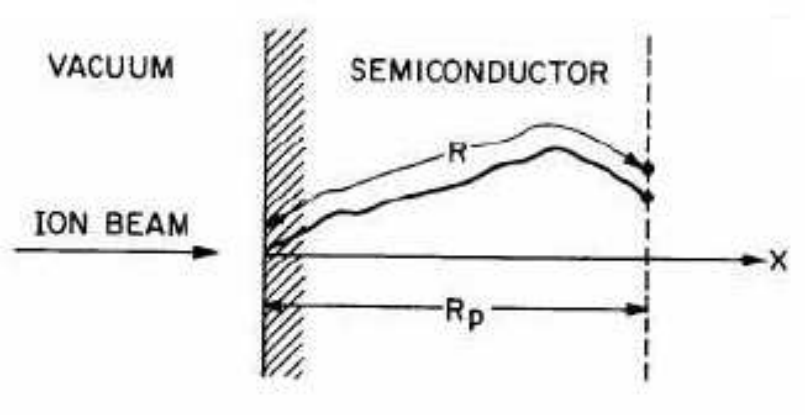

Figure 2.10: The relationship between the projected range R_p and the total ion path R [81].

density n(x) [11] (note here that the lateral motion has been ignored) as

$$n(x) = \frac{\Phi}{\sigma_p\sqrt{2\pi}} exp\left[-\frac{(x-R_p)}{2\sigma_p^2}\right] \tag{2.26}$$

where:

• x is the position of the incident ions in the target solid and it is measured along the direction of the beam

• Φ is the fluence

• R_p is the projected range

• σ_p(or ΔR_p) is the standard deviation in the projected range R_p. ΔR_p, also referred to as the range straggling is the half-width at half maximum of the implant distribution. Note that for many ion-target combinations the Gaussian approximation is not a good one, e.g. because the ion distribution is very skew or very broad.

2.6.3 Radiation damage

In general, energies used in most medium energy ion implanters (50-250 keV) are high enough to break chemical bonds and dislodge target atoms from their original

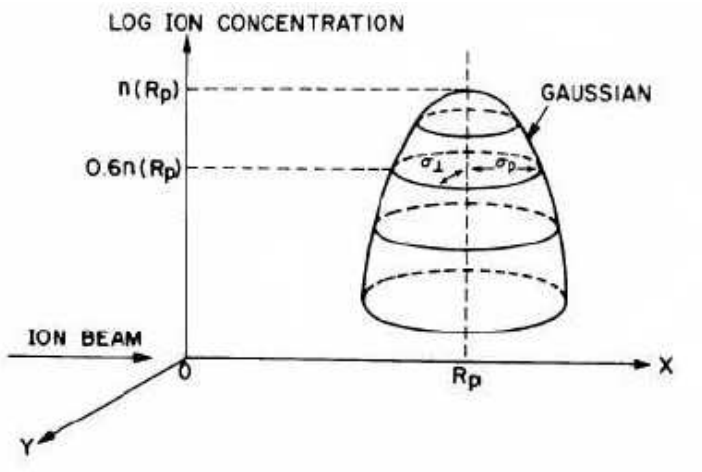

Figure 2.11: Two dimensional Gaussian of the stopped atom distribution [82].

lattice positions leaving behind a lattice vacancy [11]. The condition *sine qua non* is that the energy transferred from the projectile must be greater than the displacement energy, E_d, which is the minimum energy necessary to create a vacancy in the lattice. E_d is typically in the order of tens of eV [83]. This discussion follows books by Carter et al [78] and Billington et al [84]. The collision between projectile of energy E_0 with a stationary target atom is a primary knock-on atom effect which leads to changes in energies of the projectile E_1 and target atoms (E_2). If the energy E_2 of the primary knock-on atom is greater than E_d, it assumes the role of the projectile and then another target atom will be removed from its equilibrium lattice position, while the main projectile atom will continue with a reduced energy $E_1 = E_0$-E_2. The primary knock-on atom will be dislodged with an energy E_3, which is lower than the energy transfer E_2 due to the expansion of energy in the escape process. Moreover, if the energies E_1 and E_3 are also greater than E_d, then the projectile atom and the primarly knock-on atom will further lead to the release of more knock-on atoms and secondary knock ons, respectively, until the energy of each particle has been reduced below E_d where subsequent displacements are no longer allowed. Thus, all

the displaced atoms, within a volume surrounding the ion trajectory, create a highly disordered region known as collision/displacement cascade. This disorder introduced by ion implantation is called radiation damage.

The density of radiation damage depends on the implantation conditions, that is, the type of implanted ion (light/heavy ion), the implantation fluence, the properties of the target material, not to mention the diffusion during or after the implantation [45]. It is also known that the radiation damage increases with fluence (more ions produce more damage), thus, low fluence implantations result in isolated regions of damage while high fluence ones give rise to overlapped regions of damage, leading in some cases to the formation of new phases [11]. Furthermore, because of their larger stopping powers, heavy mass ions of a given energy cause more local lattice distortions at the end of range such as localized amorphous zones while a complete amorphized layer can be obtained when fluences above a critical ion fluence are used. In the case of diamond, ion-implantation studies [85, 86] have shown that the temperature at which diamond is held during irradiation plays a crucial role and there exist at least three different temperature regions which influence the diffusional mobility of the intrinsic point defects (vacancies and interstitials) that are created within the collision cascades. These temperature regimes include:

• A low temperature region (< RT) where neither the vacancies nor the interstitials can diffuse over large distances; they become 'frozen in'.

• A intermediate temperature region (between 320 and 800K) where the vacancies are immobile while the interstitials are mobile. This gives rise to a vacancy-rich (low material density) layer, caused by the outdiffusion of interstitials [85].

• A high temperature region (above 800 K) where, in contrast, both vacancies and interstitials are mobile. Carbon implantations under this regime have resulted in an imperfect diamond growth, characterised by a high density of dislocations caused most likely by the agglomeration of the intrinsic point defects [87]. For the specific case of the doping of diamond, using dopant ions having approximately the same

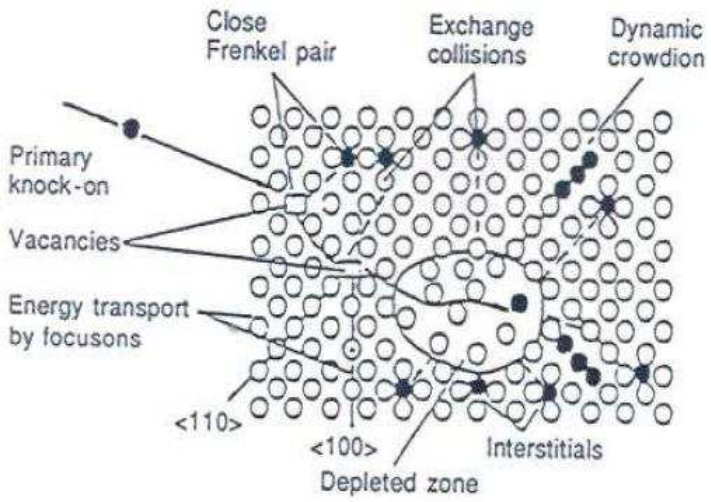

Figure 2.12: Example of typical defects by ion implantation [11].

mass as the carbon atoms, the radiation damage is primarily made of intrinsic or self point defects.

Generally, Fig. 2.12 [11] shows typical defects by ion implantation and include, among others, vacancies, interstitials and simple complexes like Frenkel pairs. A vacancy is an unoccupied crystal structure site, an interstitial is an atom between sites which comprises a substitutional defect that replaces a host atom with a foreign impurity while an interstitial defect, either native or foreign, consists of an atom displaced from its normal site [41, 55]. Frenkel pairs are pairs formed by a vacancy and an interstitial, where both of them are included in the bulk of the sample [77].

An example of a well- known defect complex in diamond is the <100>-split interstitial ('dumbbell') as shown in Fig. 2.13 [88] where two atoms share a single atomic site. According to both experiment and theory, this defect whose Raman peak is 1630 cm^{-1}, is believed to be the most stable configuration obtained during ion implantation and subsequent annealing [89, 90, 91]. Another prominent defect complex in diamond arises when vacancies cluster together to form what Prins [92]

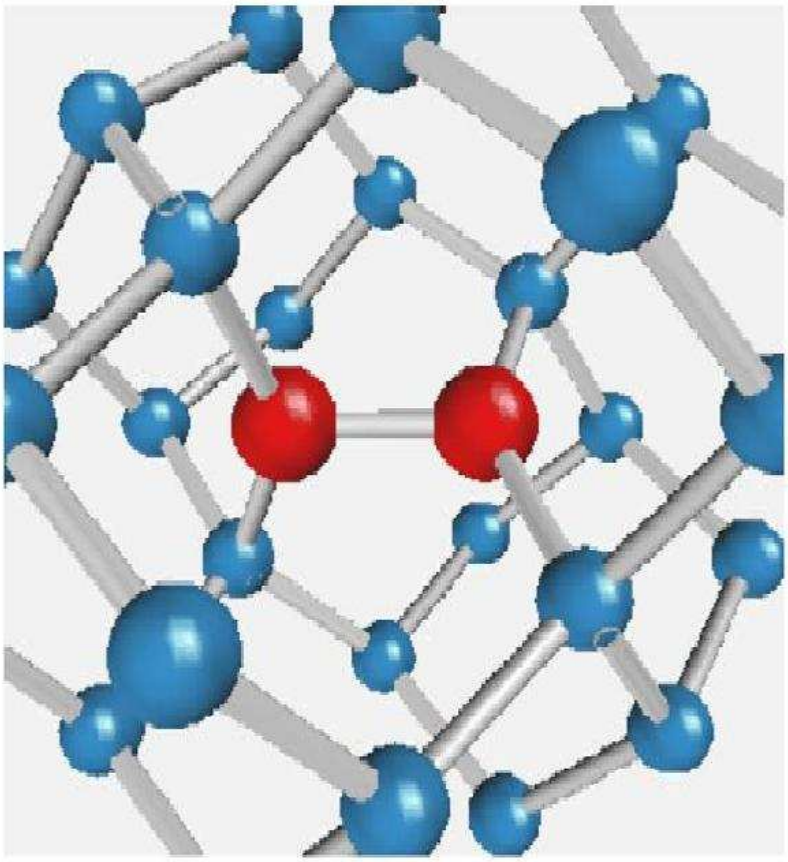

Figure 2.13: Structure of the <100>-split interstitial, showing the two atoms (in red) forming the interstitial pair, and their neighbours (in blue) [88].

has termed "vacloids", that is, an extended vacancy-region, acting like single donor centres. For more details, Table 2.6 [47] gives a more less exhaustive list of parameters of some point defects in natural and HPHT diamonds. Last but not least, a word of terminology ends this section on radiation damage. Indeed, it seems relevant to have used the term "radiation effects" instead of "radiation damage" when referring to radiation-induced property changes in materials, which are non-achievable otherwise, because the latter implies mostly unwanted effects. However, for historical reasons in connection with both the effects of nuclear particle bombardment on the properties of solids and the structural material used in nuclear reactors, and the fact that the "ra-

Defect	**Model**	**Symmetry**	**Optical absorption(eV)**	**Position**
A Centre	$[N_s\text{-}N_s]^0$	D_{3d}	~ 4	E_c- 4eV
B Centre	$[4N_s\text{-}V]$	T_d	-	-
C Centre	N_s^0	$C_{3\nu}$	-	E_c- 1.7eV
Boron	B_s^0	T_d	-	E_v+ 0.37eV
R2 Centre	I^0	D_2	1.685, 4.0	-
R1 Centre	$[I\text{-}I]^0$	C_{1h}	-	-
GR1 Centre	V^0	T_d	1.673	$\sim E_c$- 3.2eV
ND1 Centre	V^-	T_d	3.150	$\sim E_c$- 3.2eV
Divacancy	$[V\text{-}V]^0$	C_{2h}	2.543	-
VN Centre	$[N_s\text{-}V]^0$	$C_{3\nu}$	2.156	-
W15 Centre	$[N_s\text{-}V]^-$	$C_{3\nu}$	1.945	-
H2 Centre	$[2N_s\text{-}V]^-$	$C_{2\nu}$	1.257	-
H3 Centre	$[2N_s\text{-}V]^0$	$C_{2\nu}$	2.463	-

Table 2.6: Intrinsic/extrinsic point defects in natural and HPHT diamond and their known properties.

diation effects" result from damage sustained by the crystalline lattice, we preferred to retain the older term of radiation damage [84].

2.6.4 Channelling

The influence of the crystal lattice orientation on the trajectories of the penetrating ion is channelling [93]. This phenomenon often occurs while implanting in crystalline targets where the beam is incident along a low index crystallographic direction leading to a deeper penetration of ions into the crystal before coming to rest. By low index crystallographic directions, one implies those which offer wider channels (least

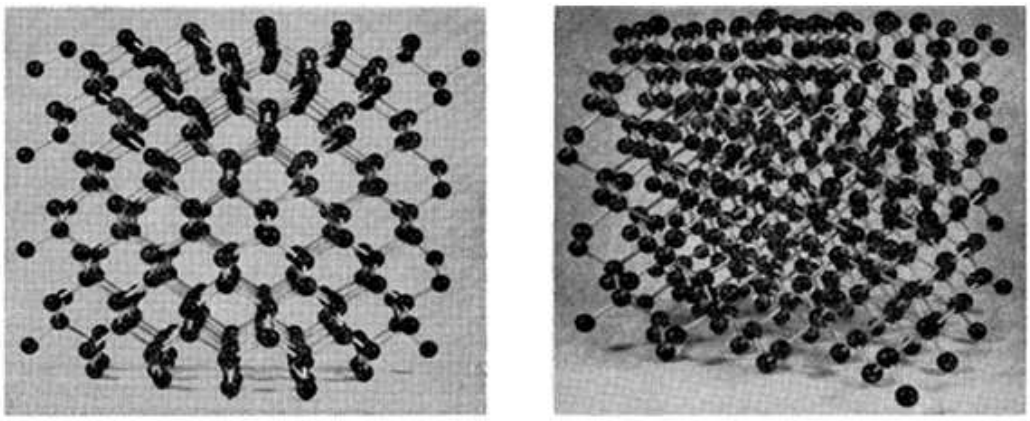

Figure 2.14: Model depicting the diamond lattice. The panel on the left hand side shows a <110> direction, while the right hand side one shows the diamond lattice viewed along a random direction [95].

resistance to the ion motion), that is, along the most open directions as shown in Fig. 2.14. A satisfactory way of minimizing the effects of channnelling and which we used in all our implantations, is to tilt the diamond sample by about 7° to the incident beam direction [94] as shown in the right hand side panel of Fig. 2.14 [95]. However, studies by Simonton et al. [96] have shown that even a 7° angle employed in commercial/research ion implantation of crystalline materials does not prevent completely the effects of channelling. This is due according to them, to unavoidable scatter-in (indirect) and direct channelling effects.

Chapter 3

Experimental Techniques

3.1 Layout of the Chapter

As highlighted in the title of the thesis, X-TEM specimens were the starting point of our investigation. The X-TEM specimens must be slices cut perpendicular to the surface below which the irradiation damage is being studied. The diamond slices must be reduced to about 40 μm as described in Section 3.2 before final thinning by ion milling can be attempted. This can only be achieved by careful mechanical polishing, a process which may raise the diamond sample temperature into the annealing region. This would compromise the rapid annealing to a known temperature, which is part of the desired procedure. It is necessary therefore to polish the slices down first, then implant them into the thin edge, then anneal according to the desired regime. Fortunately the implant depth (about 0.25 μm) is very much less than the specimen thickness of $\sim$ 40 μm, which still appears to be a large area specimen from the ion implantation point of view.

This chapter outlines the experimental techniques used in this study. Section 3.2 emphasizes the mechanical polishing of our diamond samples. Section 3.3 outlines the ion implanter used in creating the desired damage while section 3.4 discusses the annealing setup designed for repairing the damage. Section 3.5 presents ways of prepar-

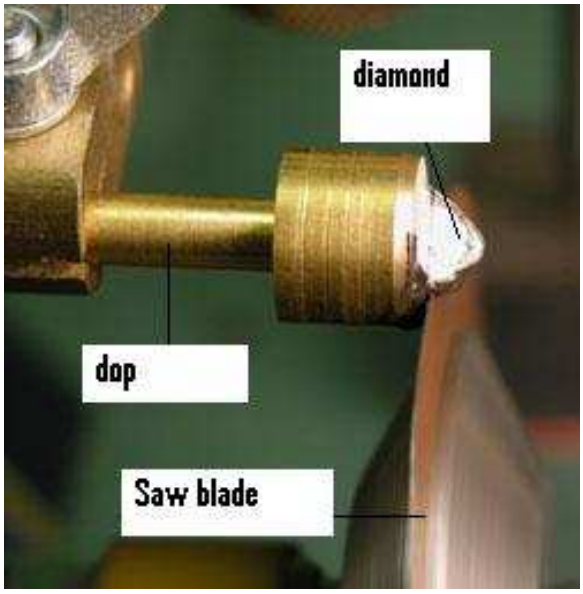

Figure 3.1: Photograph of a diamond saw [97].

ing and thinning the diamond samples down to electron transparency. Section 3.6 reviews the relevant experimental techniques used to characterize the ion-irradiated and annealed diamond samples.

3.2 Sample preparation (Mechanical Polishing)

The diamond samples used in this study were supplied by De Beers Industrial Diamond Division (Pty). They included four natural type Ia and four synthetic type Ib diamonds. The synthetic ones were half octahedron in shape, with single substitutional nitrogen concentration of about 100 ppm. In order to get rigid parallel sided thin diamonds, rough diamonds of about 1 carat (200 milligrams) in weight were first cut by means of a saw or a laser then they were polished less than 2° off the principal planes, using a cast iron disc. The sawing process is done by pressing rough diamonds mounted in a dop (See Figure 3.1 [97]) onto a blade.

The blade is a paper-thin wheel of phosphor bronze which rotates, in a downward

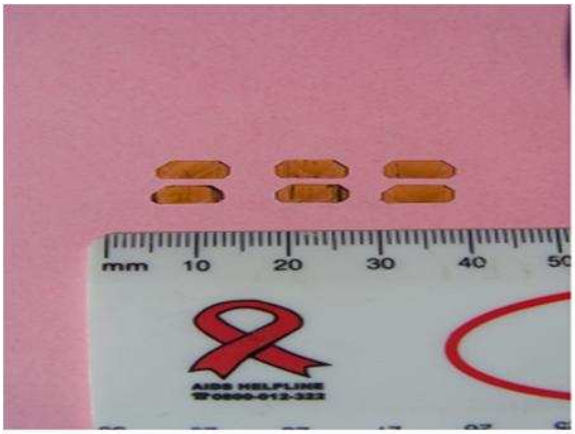

Figure 3.2: Photograph of three pairs of 110 flakes of HPHT diamonds of $\sim$ half mm thickness.

direction against the diamond, at about 4000 revolutions per minute (rpm) and its rim is charged with a mixture of diamond powder and light oil. The dop has a built-in large weight whose role is to apply pressure to the diamond during the sawing process. Figure 3.2 shows three pairs of 110 flakes of HPHT diamonds, one of which was sawed along the <100> direction and the other two pairs were laser cut along the same direction. Note that due to the high anisotropy of diamond, sawing is only achieved along the {100} or {110} plane in a definite direction [98]. In addition, sawing along the {111} plane is impossible so in order to obtain (111) faces of diamond, one resorts to cleaving and laser cutting with the former being possible due to the fact that the {111} plane has the lowest strength [99], while the latter can just be done in any direction.

The three pairs of synthetic diamonds are large flat diamond samples with thickness of about half a millimetre, each trapezium-shaped with dimensions of $7\times5\times2.5$mm where 7,5 and 2.5 mm refer to parallel sides and height of trapezium, respectively. Laser cutting was much faster than sawing diamond. For instance, it took about four hours to cut through a rough diamond of about 1 carat whereas just a few minutes were used to laser cut it. After sawing or laser cutting, the rough edges of the dia-

monds of about half a millimetre were smoothed off down to $\sim$ 200-300 μm by rubbing them back and forth against an alloy steel disk with coarse diamond powder of about 6-12 μm which leads to a rapid removal of diamond material followed by a finer powder so as to have smooth diamond surface at the end. The smoothed off diamond samples were then held into position for mechanical polishing through brazing, since their small thickness made it difficult to use any other technique. Thermal expansion mismatch was avoided by mounting them onto a large diamond, designated as reference diamond surface, using a three components brazing alloy around the sample. The reference diamond surface and the sample were then heated in a vacuum furnace to the brazing alloy temperature of about 560-580^{0}C for soldering [100]. It is worth mentioning that the reference diamond surface was polished beforehand in order to have parallel faces and high finishing surface, so as to ensure good contact. Also great care was taken to prevent any brazing alloy to creep underneath the sample to avoid specimen thickness measurement inaccuracy. This was achieved by etching off any excess dried brazing alloy that surrounded the sample. These manipulations, and polishing, were carried out by Mr. Mik Rebak and Mr. Tshepo Colby Mashego based at iThemba LABS (Gauteng).

Finally the diamonds were mechanically polished, using the setup highlighted in Figure 3.3 [101], by pressing the assembly of reference diamond and sample, initially mounted in a holder, against a scaife. The scaife was a cast iron disc rotating at about 3000 rev min^{-1} and was used to jig and polish the sample down to 40 μm, periodically adjusting the X-direction micrometer to maintain the '0' (X-Y direction) inclinometer settings [100, 102, 103].

In order to obtain the desired thickness, the amount of the removed material was monitored throughout the mechanical polishing process via a digital, five decimal high gauge micrometer. After the polishing, some of the samples were cleaned by boiling them for about 30 minutes in a three component acid as described in section 2.2. The cleaned diamonds were then rinsed in double-distilled deionized water and

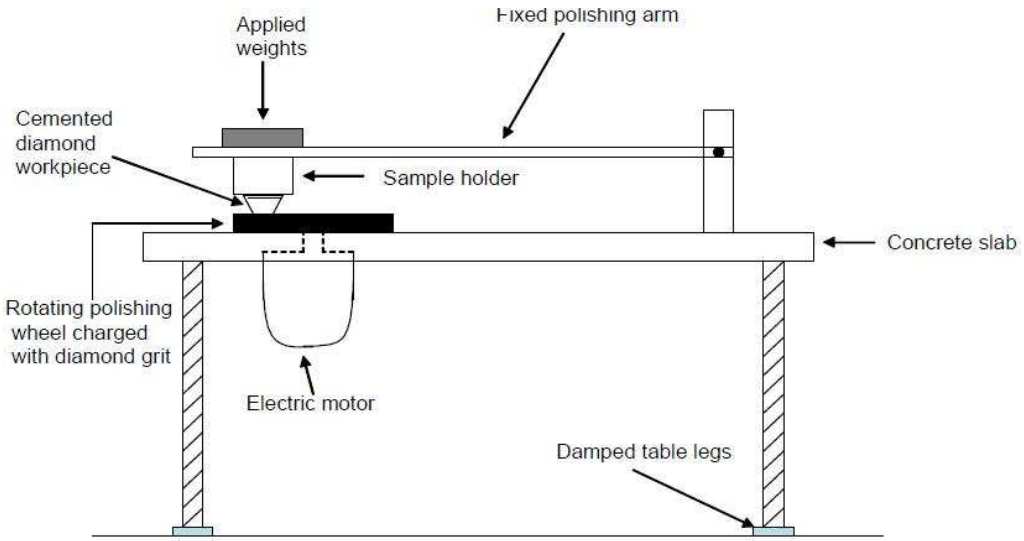

Figure 3.3: A schematic diagram of a simplified set up used for the mechanical polishing of diamond surfaces [101].

then dried off by blowing dry nitrogen gas over their surfaces. The dried samples were safekept in polythene bags, while awaiting to be implanted.

The mechanism behind the diamond polishing has fascinated many authors over almost a century. In 1920, Tolkowsky [104] investigated the anisotropy in wear and suggested that abrasion is the main wear mechanism during the polishing of diamond, using a scaife, irrespective of the polishing directions. Wilks and Wilks [105] measured the abrasive resistance on three crystallographic planes and pointed out that the anisotropy of the wear depended on the crystallographic plane and on the direction of polishing. Wilks and Wilks [105] agreed wholeheartedly with Tolkowisky's model of wear mechanism. They suggested that the polishing proceeds via a microcleavage process both in the 'soft' and 'hard' directions. Wilks and Wilks [105] also found that for low-index planes of diamond, that is, the cube plane {100} and the dodecahedral plane {110}, the cube directions <100> showed a high wear rate than the <110> directions. Consequently <100> and <110> crystallographic directions have been referred to as 'soft' and 'hard' directions for these two crystallographic

planes. In addition, the octahedral plane {111} is quasi-impossible to wear even though it has a slightly threefold symmetry [106]. Therefore, attempting to polish this plane is achieved by tilting off the face of the principal plane by 1 or 2° towards the dodecahedron [11$\bar{2}$] direction [105, 107]. Hird et al. [106, 108] have described the 'soft' directions as those in which easy wear occurs and characterized by a high heat and relatively a low vibration. Also, they have reported in the 'hard' directions of polishing, a poor finish accompanied by grating noises, high vibration, and damage to the scaife as well as that of the diamond being polished. Similary, Yarnitsky et al. [109] and Rebak et al. [100], to name a few, confirmed Tolkowsky and Wilks' findings. The former reported that the abrasion of diamond proceeds mainly by a microfracture/micro-chipping process in the 'soft' and 'hard' directions while the latter reported as well that microchipping and chemical absorption of carbon into iron are the main wear processes in diamond. In contrast to the earlier studies, Couto et al. [110] found out that the faces polished along 'hard' directions showed rough structure indicating that the material was removed by fracture and chipping on a nanometer scale while the faces polished along 'easy' directions had superposition of several grooves whose width and depth were 20-100 nm and 2-12 nm, respectively and these could not be explained by a fracture/chipping mechanism.

In addition, systematic studies [103, 111, 106, 108], among many others, have used electron microscopy based techniques for the analysis of debris produced during the diamond polishing. They have reported that polishing in 'hard' and 'easy' directions is governed by two different wear mechanisms. Their results were consistent with a model of a shear-induced transition of sp^3 to sp^2 carbon material in the 'soft' <100> directions on the cube plane {100}. This model is in stark contrast with that of Tolkowsky, Wilks and Wilks et al. presented earlier, but is usually accepted. In the hard <110> directions on the cube plane {100}, the wear process occurs by micro-fracture.

3.3 Ion implantation

3.3.1 Introduction

This work involved mainly the study of radiation damage caused by ion irradiation or ion implantation on diamond. Ion implantation is designed to alter the near surface properties of semiconductor materials without changing their bulk properties. This requires a machine that generates an ion beam and steers it onto the target material where the ions come to rest less than a micron below the surface. A modified Varian/Extrion model 200-20A2F ion implanter was used for implantations for this research. Before modification, this type of implanter was specifically designed as a production tool for the manufacturing of ion implanted, semiconductor devices at various doping levels. Generally, keV implantations use incident ions in the range of $\sim$ 10-300 keV for modifying the property of semiconductor materials to a depth of $\sim$ 10^2-10^4Å[11]. All the ion implantation experiments were performed at iThemba LABS (Gauteng). In this study, singly charged carbon ions were implanted edge-on, according to the CIRA (Cold-Implantation-Rapid Annealing) routine. A special holder, as shown in Fig 3.4, was fabricated making it easier to mount the thin diamond sample edge-on to the incoming ion beam. Multiple implantations, in contrast to single implantations, were performed at the liquid-nitrogen target temperature (77K), followed by a rapid thermal annealing. The implantation parameters and the different fluences used are presented in Table 3.1 [72] which is the fractional fluence at the different energies. The spread of the implantation energies and fluences done in the multi-implantation recipe are used to spread the radiation damage over a larger width [85]. Detailed multi-implantation parameters were derived from the fractional fluence at the different energies of Table 3.1 and presented in Table 3.2. Note that low/high fluence implantations are below/above the critical amorphization threshold. The term 'amorphization' describes the structural reorganization occurring in

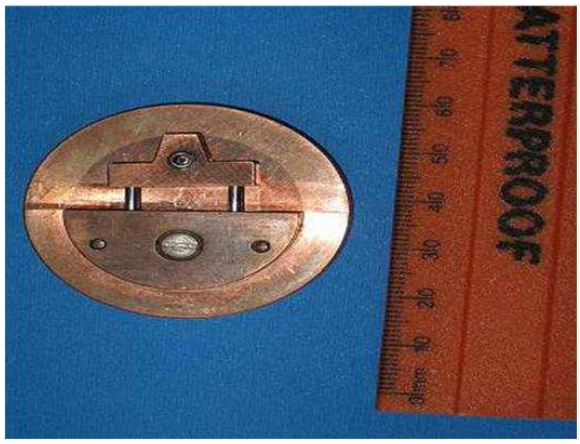

Figure 3.4: A photograph of thin diamond holder.

Implanted Ion	**Implant Energy (keV)**	**Normalised Fluence**
^{12}C	150	1
^{12}C	120	0.652
^{12}C	80	0.548
^{12}C	50	0.3

Table 3.1: Implantation parameters: Fractional fluence at the different energies.

the damaged layer [69] while the critical amorphization threshold is defined as the fluence at which annealing cannot restore the damaged layer to a form close to its pristine state, but instead, results in the transformation of the layer to 'graphite' upon annealing [112]. The ion fluence (or ion dose) and the dose rate are respectively, 'the total number of ions incident per unit area of the target material and the rate at which the implantation occurs, often expressed in terms of the beam current density i_b in units of $\mu A/cm^2$'[11]. The total fluences for the $^{12}C^+$ used in this study were 1.0×10^{15}, 2.5×10^{15} and 5×10^{15} ions/cm^2 (low fluence implantations i.e. below the fluence for the critical amorphization which was found by Spits [72]

Implanted ion	**Ion Energy**	**Low fluences**	**High fluences**
-	[keV]	(ions/cm^2)	(ions/cm^2)
-	-	Fluence component	Fluence component
^{12}C	150	0.4×10^{15}	2.80×10^{15}
^{12}C	120	0.2608×10^{15}	1.8256×10^{15}
^{12}C	80	0.2192×10^{15}	1.5344×10^{15}
^{12}C	50	0.12×10^{15}	0.84×10^{15}
TOTAL	**FLUENCE:**	$\mathbf{1.0\times10^{15}}$	$\mathbf{7.0\times10^{15}}$
^{12}C	150	1×10^{15}	2.4×10^{15}
^{12}C	120	0.652×10^{15}	1.5648×10^{15}
^{12}C	80	0.548×10^{15}	1.3152×10^{15}
^{12}C	50	0.3×10^{15}	0.72×10^{15}
TOTAL	**FLUENCE:**	$\mathbf{2.5\times10^{15}}$	$\mathbf{6.0\times10^{15}}$
^{12}C	150	2×10^{15}	-
^{12}C	120	0.304×10^{15}	-
^{12}C	80	1.096×10^{15}	-
^{12}C	50	0.6×10^{15}	-
TOTAL	**FLUENCE:**	$\mathbf{5\times10^{15}}$	-

Table 3.2: Detailed implantation parameters.

to be $\approx 5.2\times10^{15}$ ions/cm^2 for the implantation parameters used in Table 3.1.) and the fluences 6.0×10^{15} ions/cm^2 and 7.0×10^{15} ions/cm^2 (which represent high fluence implantations, meaning above the fluence for the critical amorphization threshold). The specific fluence data of Table 3.2 were deducted from the normalised fluene numbers given in Table 3.1. In addition, the dose rate for all the implantations was $\sim$ 1 μA cm^{-2} and the diamond samples were tilted by about 7° to the incident beam

direction for the minimization of channelling as discussed in Section 2.6.4. The diamond samples were also cooled to liquid nitrogen prior to implantation. Finally, after implantation, each diamond sample was rapidly removed from the target holder and kept under liquid nitrogen in a dewar, while waiting to be annealed. The rapid thermal annealing technique is discussed in section 3.4.

3.3.2 Instrumentation

Fig.3.5 highlights the major components of the Ion Implanter followed by its operational principles summarized from the Instruction manual production Ion Implanter model 200-20A2F [113]. The modified Varian/Extrion model 200-20A2F uses a Freeman-type ion source consisting of a tungsten filament which is heated by the high filament current and generates electrons thermionically. The electrons collide with the gas molecules resulting in the ionization of the charge that leads to a plasma within the ion source chamber. A beam of ions which is generated by the hot cathode arc discharge ion source is extracted from the source by the electrostatic field set up between the source exit aperture and an extraction electrode. These ions are subsequently accelerated to an energy of 25 keV and admitted to a 90° double focusing mass analyzing magnet in the high voltage terminal. The ionization of the charge in the ion source chamber creates usually more than one ion species at the same time depending on the source supply gas selected. Thus, the mass analyzing magnet is used for ion selection. It separates the different ion species based on their charge-to-mass ratio. As a result, only the desired species is allowed to pass through the resolving aperture diameter and proceed to the acceleration tube. All the other ions in the beam will follow different paths determined by their charge-to-mass ratio. Ions with smaller charge-to-mass ratio will be steered into smaller orbits while ions with larger charge-to-mass ratio follow larger arc trajectories and these unselected ions will be collected on the analyzer chamber walls or on either side of the resolving aperture which is located in the image plane. The ion source, mass ana-

lyzer and variable slit systems as shown in Fig. 3.5 [113] are contained in a high voltage terminal which is located inside a grounded enclosure, to promote safety to personnel. On emerging from the resolving aperture, the ion beam enters the linear acceleration tube to optimize beam focusing and minimize X-rays generated by electron backstreaming. The main acceleration of the ion beam, which emerges with an energy between 25-200 keV is provided by the field in the acceleration tube. The beam diverges slightly as it passes through the acceleration region due to its limited focusing action until it reaches the lens located at the entrance of the scanner box. The lens of the 200-20A2F ion implanter is an electrostatic quadrupole triplet which is used to focus the beam to a 1 cm^2 in the target chamber. After passing through the lens, the converged beam enters a set of scanning plates in the deflection region. The electrostatic deflection plates first deflect the beam in the vertical (Y) plane and then in the horizontal (X). This set of deflection plates is used to generate a raster or uniform implant over a large area [114]. Finally, the specimen is attached to a sample holder which is mounted onto the target chamber. Different holders can be mounted at the end station and the sample can be kept at liquid nitrogen temperature (LN_2), room temperature or even higher temperatures thanks to the presence of an active cooling system or heater within the temperature control system. The focused beam current is measured directly in a deep Faraday cup (center cup) before the implant. It has four corner cups, mounted in front of the target holder to allow the beam to be sampled during the implant. In addition, the current registered by each of the four Faraday cups may be used to check the scan uniformity.

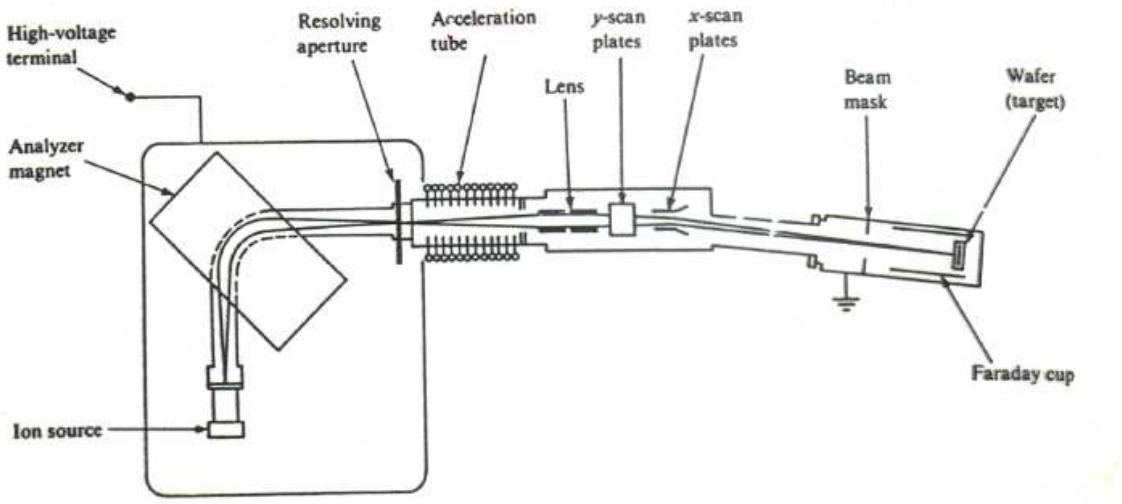

Figure 3.5: A schematic diagram of the model 200-20A2F Ion Implanter [113].

3.4 Annealing

3.4.1 Introduction

The radiation damage created by ion implantation reaches thermodynamic equilibrium once the source of irradiation is removed, thus the equilibrium concentration of radiation effects depends on the temperature at which the sample is held during implantation. Post-implantation annealing or thermal treatment has been proved to reduce or repair the radiation damage and at the same time activate the dopant atoms in semiconductor materials. Annealing is commonly carried out isochronally or isothermally. In the former, the temperature of the sample is raised in step-like temperature pulses of constant duration Δt, from implant temperature to successively higher temperatures T_i, T_{i+1},... while in the latter, the temperature of the sample is raised a from implant temperature to a fixed temperature. Note that in both annealing procedures, after each pulse, the sample is cooled down to room temperature for

measurement of the property of interest. In addition, successful annealing of diamond is carried out in vacuum or under protective gas, otherwise if diamond is annealed in air to about 770 K, it 'ignites and disappears' [115]. Thus, the as-implanted diamonds held at liquid nitrogen temperature were rapidly transferred to a fixed temperature of 1600 K (under a protective flow of high purity argon gas) and annealed for 30 min and allowed to cool down to room temperature. The examination of the residual defects was carried out at room temperature.

3.4.2 Cold-Implantation-Rapid-Annealing Technique

Prins [85] devised a route for the optimization of the doping of diamond which he called the cold-implantation-rapid-annealing (CIRA) technique. In the CIRA technique one implants a fluence below the critical threshold, at liquid nitrogen target temperature (77 K), spreading the implantations over a range of energies and fluences in a non channelling direction followed by rapid thermal annealing. The model he proposed [116] to describe the reaction rate of annealing in diamond assumed that the radiation damage created in the collision cascades consists primarily of individually displaced atoms and vacancies. One can say that implanting at 77 K 'freezes in' and evenly mixes the interstitial atoms and vacancies while the multi-implantations make the depth-width of the damage as large as possible. After implantation, subsequent rapid thermal annealing (RTA) to at least 500-1000 ^{o}C is required to allow the self-interstitial atoms to become mobile and combine with vacancies thus reducing the residual radiation damage while dopant atoms doing the same are caught in substitutional sites [117, 118].

It was postulated [119] that there exists a volume around the vacancy whereby an interstitial atom has no alternative but to combine with the vacancy, and therefore interstitial sites within this volume have been termed 'catch-sites'. Similarly, in the surroundings of this 'catch-volume', there exist sites 'from which an interstitial can either jump into a catch-site or away from the catch-volume into an adjacent inter-

stitial site' [119, 71] and these have been called 'meet sites'.

Assuming that, on average, 'an interstitial has to make μ_m jumps to reach a meet-site, the average number of jumps μ_c needed to reach a meet-site and jump into a catch-site' [71] is given by

$$\mu_c = \mu_m \left(1 + q exp\Big[\frac{E_C - E_D}{k_B T} \Big] \right) \tag{3.1}$$

where k_B is the Boltzmann's constant; q is the ratio of the number of accessible interstitial sites to catch-sites surrounding a meet site; E_C is the activation barrier that an interstitial has to scale when jumping from a meet-site into a catch-site while E_D is the activation barrier which it has to scale when it diffuses and T is the temperature. Note that the number of jumps to reach a meet-site is inversely proportional to the number of vacancies N_v and is defined as

$$\mu_m = \frac{Q}{N_v} \tag{3.2}$$

The optimization of the CIRA routine consists of ensuring that residual radiation damage is negligible after annealing. The reduction of radiation damage can only be achieved by making sure the interstitials only combine with the vacancies. In an ideal situation one wants all the dopant atoms to move into vacancies and the self-interstitials to mop up the rest [117]. However, in practice, dopant and self-interstitial atoms may diffuse out of the implanted layer of depth-width ω created during liquid nitrogen implantations and thus do not participate in the vacancy annihilation. Also, they may be trapped by other defects or agglomerate to form complex defects.

If μ_e describes all interstitial interactions which do not involve any vacancy annihilation and μ_c the average jumps to meet up and annihilate a vacancy, then, the

average probability P_c that an interstitial will annihilate a vacancy can be written as

$$P_c = \frac{\mu_e}{\mu_e + \mu_c} \tag{3.3}$$

The probability P_c depends on the interstitial distribution within the depth-width layer ω. In addition, as soon as $\mu_c < \mu_e$, no interstitial atoms will escape from the layer, therefore, the probability of Eqn. 3.3 can be written as

$$P_c = \frac{\mu_e}{(1-\Phi)\mu_e + \mu_c} \tag{3.4}$$

where Φ lies between 0 and 1. Substituting eqns. 3.1 and 3.2 into Eqn. 3.4 leads to

$$P_c = \frac{\mu_e N_v}{(1-\Phi)\mu_e N_v + Q\left(1 + qexp\left[\frac{E_C - E_D}{k_B T}\right]\right)} \tag{3.5}$$

The probability of Eqn. 3.5 will be greatly increased near 1 when μ_e is as large as possible. This is achieved by proceeding to multiple implantations, which increases the depth-width of the implanted atoms and as a consequence increases μ_e [117]. It is noteworthy mentioning that the parameters of the CIRA process contribute to make the probability P_c to be closer to 1. This reduces drastically the residual radiation damage thus minimizing the unwanted compensating trapping of charge carriers.

3.4.3 Instrumentation

The rapid thermal annealing (RTA) furnace used was an electrical horizontal split tube furnace (STC) as shown in Fig. 3.6 , with a maximum operating temperature of 1500 ^{0}C. Its four silicon carbide rods heating elements are arranged symmetrically around a separate ceramic worktube to ensure excellent thermal uniformity. The conventional method of annealing consists of dropping the as-implanted sample down a vertical tube furnace against an upward flow of argon. This was not possible with very thin diamond samples of about 30 μm, as they would not have sufficient weight

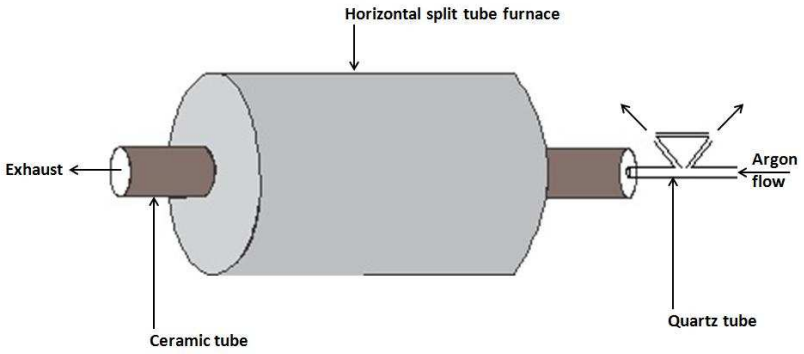

Figure 3.6: Horizontal Split Tube Furnace.

to fall through an upward stream of argon. Thus, a novel technique of rapidly annealing very thin diamonds, with an argon gas gun was designed and is described briefly below.

A long quartz tube was inserted in the separate ceramic worktube with one of its ends connected to a constant flow of high-purity argon so as to avoid an oxidizing atmosphere. This effectively prevents unwanted oxidisation/graphitization and possibly the disappearance of the as-implanted diamond sample. The annealing temperature was set, and allowed to settle. Once this was achieved the as-implanted diamond sample was swiftly removed from a liquid nitrogen dewar bath and then transferred into the pre-heated furnace as quickly as possible and annealed for about half an hour at 1600 K under a constant flow of high-purity argon. The rapid transfer of the as-implanted diamond was made possible by blowing it in using a stream of argon gas which was already flowing through the quartz tube. In addition, the enlarged quartz tube of Fig. 3.7 was designed in such a way that the as-implanted sample would be captured in the central bulk, i.e., precisely in the middle of the four symmetrical silicon carbide heating elements where the temperature is maximum.

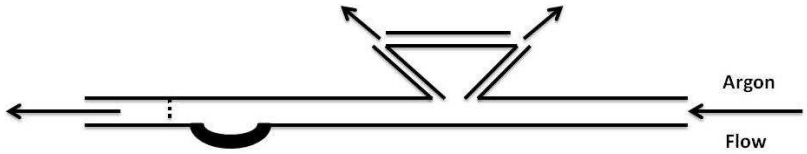

Figure 3.7: Schematic diagram of the quartz tube. Some argon flows continuously out of the entry funnel, preventing the ingress of air

3.5 Ion Milling

3.5.1 Introduction

Ion milling is a slow process in hard materials. In order to apply it to diamond specimens it was necessary to reduce their thickness to about 40 μm by mechanical thinning techniques as described in Section 3.2. Ion milling is a widespread final specimen preparation technique which suits cross-sectional transmission (TEM) specimens in that it thins the latter down to electron transparency. Cross-sectional specimens for TEM observations were prepared as follows: After the diamond slices of about 40 μm were implanted edge-on, at liquid nitrogen temperature followed by rapid thermal annealing for 30 minutes in a argon atmosphere, pairs of thin slices were glued edge against edge onto a copper support TEM grid. Then 3 mm round discs were cut out corresponding to the dimensions of the copper grid using a laser. Thus implanted and unimplanted diamond samples could be easily compared. The glue used consisted of two-component Gatan epoxy which was mixed according to the standard ratio, i.e., 1 hardener to 10 resin. The glued samples were then heated in an oven at 170° for about 15 minutes for hardening. The final thinned samples were argon ion beam milled at the NMMU (Nelson Mandela Metropolitan University) in a Gatan Precision Ion Polishing System (PIPS, model 691) using 5 keV argon ions at an incident angle of 5° with respect to the diamond sample surface. Figure 3.8

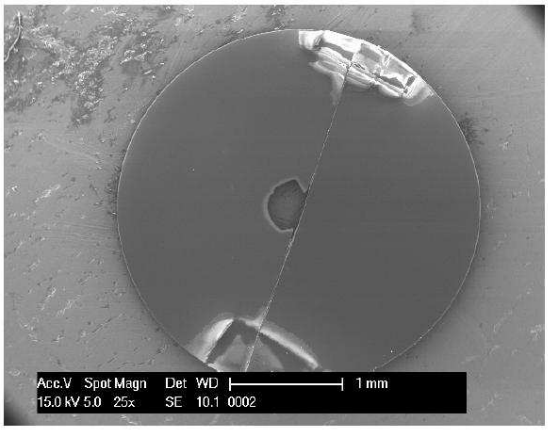

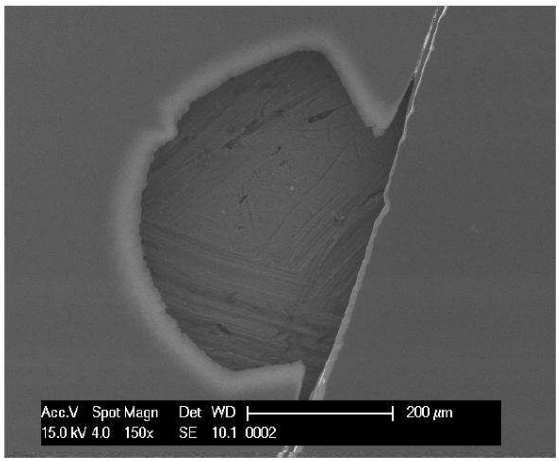

Figure 3.8: Scanning electron microscope (SEM) images of the cross-sectional ion milled diamond TEM sample. TEM investigations were carried out at the edge of the hole at the diamond/diamond interface.

shows low and high magnified scanning electron microscope (SEM) images. As the diamond samples were implanted edge-on, the electron transparent regions would be at the edge of the hole at the diamond/diamond interface.

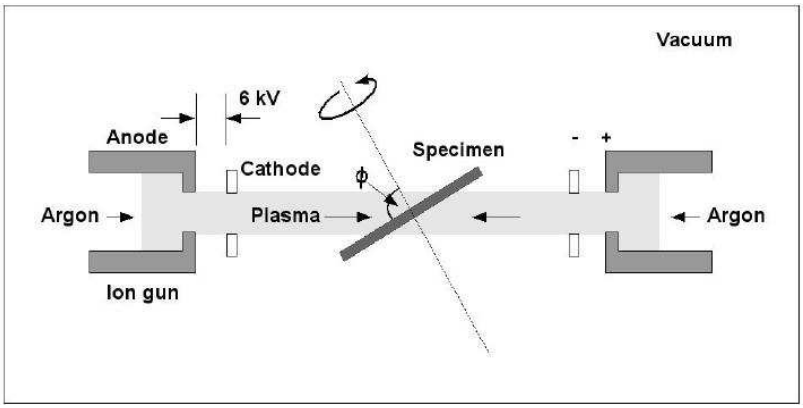

Figure 3.9: A schematic illustration of an ion-beam thinning device [121].

3.5.2 Instrumentation

Ion milling involves an argon ion bombardment of a 3 mm round TEM disc specimen in order to sputter material from the area of interest. The main variable in this process is the sputtering coefficient, defined as the number of sputtered atoms per incident atom, which depends on the angle of incidence, the accelerating voltage, the nature of the impinging ions, the ion milled material as well as the background atmosphere [120]. Using electric discharge a beam of argon ions up to 6 keV is generated and accelerated towards the specimen to be ion-milled as shown in Figure 3.9 [121]. Note that argon is used in the ion milling system because it has a high sputtering yield and it does not participate in inducing any chemical reactions. In addition, accelerating voltage of about 2.5-6 keV and small angle of incidence less than 6° are used to prevent compositional thinning. It is also important to keep the ion milling environment under vacuum of (10^{-5}- 10^{-6}) bar and possibly cool down the specimen using liquid nitrogen. On the other hand, some of the disadvantages of ion milling include its slow process in strong materials and its introduction of unwanted radiation damage which may be easily confused with the very defects under investigation.

3.6 Focused ion beam milling(FIB) SEM

A focused ion beam (FIB) SEM (Scanning electron microscope) can be described as a SEM with a built-in ion mill or an ion gun with a SEM attachment [122]. The FIB system typically uses a beam of Ga ions which is steered over the specimen surface at an accelerating voltage of a few keV. Cross-sectional TEM samples were prepared using the lift-out method with the aid of a dual-beam FIB that is equipped with a nanomanipulator. The stages in making cross-sectional TEM samples with the lift-out method [123] (See Figure 3.10 [122]) are itemized as follows:

- The specimen is first viewed using the SEM attachment in order to select a region of interest to be thinned.
- To avoid surface damage by the Ga^+ ion beam, a protective coating of carbon or platinum is deposited on the specimen surface over the region of interest from which the region is to be cut.
- Two 'FIB boxes' separated by a 1 μm lamella are milled into the specimen on either side of the selected region.
- Then a sharp tungsten needle, called a nanomanipulator, which is attached to piezoelectric drive motors is inserted. The one used was computer-controlled which made it easy to bring it gently into contact with the lamella. Note that the point of contact of the tungsten needle with the thin-film lamella is reinforced by the deposition of a small amount of platinum or amorphous carbon. The deposition is done with either the ion or electron beam in combination with a gas injection system. For the specimen used in this work, carbon deposition was used as the protective layer.
- Using the ion beam, the lamella is completely separated from the substrate and transferred to a TEM specimen 'grid' (See Figure 3.11) [123] within the

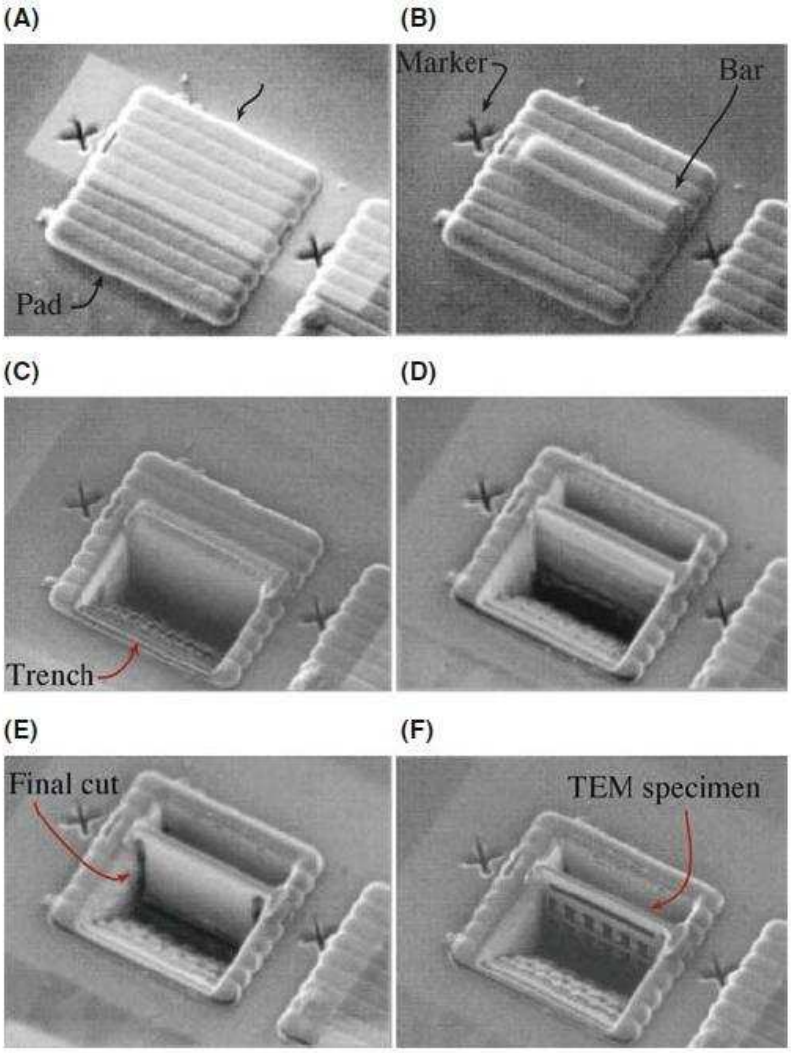

Figure 3.10: Stages in making cross-sectional TEM samples using the lift-out method. (A) The area of interest has been marked. (B) A Pt bar is deposited to protect this area from the Ga beam. (C,D) The two trenches (FIB boxes) are cut. (E) The bottom and sides of the slice are (final) cut. (F) The TEM specimen is extracted and polished after welding it onto the TEM specimen grid [122].

vacuum chamber. The TEM specimen grid is a half-ring, 3mm in diameter and the lamella is joined to the grid by platinum or tungsten deposition.

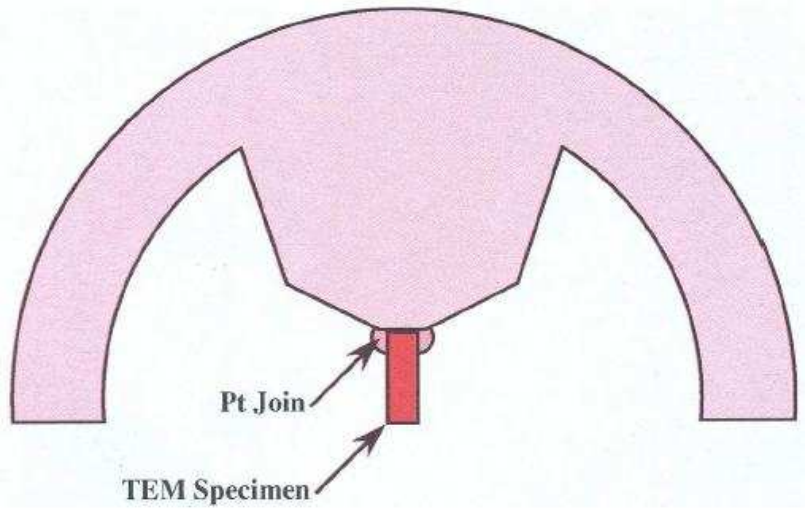

Figure 3.11: Schematic drawing of a 3 mm diameter half-ring, used for mounting a thin TEM specimen lamella in the lift-out method [123].

- The final thinning of the 1 μm thick lamella is performed using a much lower ion beam current and ion energy to reach ∼20-50 nm thickness which is thin enough for HRTEM.

3.7 Characterization Techniques

3.7.1 Raman spectroscopy

Introduction

When monochromatic light is incident on an atom or a molecule, most of the radiation will be transmitted, some will be absorbed, while a very small fraction will be scattered by the molecules in directions different from that of the incoming radiation. About 0,01% - 0.1% of the radiation will be elastically scattered, that is, no energy is lost and the frequency of the incident and scattered radiation will be the same. This type of scattering is the so-called Rayleigh or Classical scattering, which is of

no interest in Raman spectroscopy.

A minute fraction (10^{-6} - 10^{-4}) of the scattered radiation will be inelastically scattered. The inelastic scattering of light by matter was theoretically predicted in 1923 and the first experimental observation was made by C.V. Raman in 1928 [124]. He discovered that the visible wavelength of a minute fraction of the radiation scattered by certain molecules differs from that of the incident radiation and thus the shift in wavelength depends on the chemical structure of the molecule responsible for the scattering. The effect, known as the Raman effect, was due to the interaction of the photons of incoming light with the vibrations and rotations of the molecules [124].

Raman spectroscopy has been proved to be a non-destructive technique which is useful in condensed matter physics and chemistry in that it identifies the symmetries of molecular structure and bonding and the energies associated with the fundamentals excitations of the solid [11]. Particularly, Raman spectroscopy has the ability of distinguishing clearly between the different carbon allotropes thus, its choice in the characterization of unimplanted, as-implanted and implanted and annealed diamond samples [83].

An overview of both the classical approach and the quantum mechanical approach which describe the Raman effect is given in the next section. The following discussion is based mainly on these texts [39, 125, 126, 127, 128, 129, 130, 131, 132, 133, 134].

Classical Approach

The classical approach assumes that the Raman effect arises from the interaction of the incident electromagnetic photon with the dipole moment of the molecules of the illuminated material under investigation. The molecule's dipole moment is dependent only on the electric field component of the electromagnetic radiation. The exposure of a polarizable molecule to an external electric field E leads to the distortion of the molecule's equilibrium electronic distribution. This results in the creation

of induced dipoles μ_i within the molecules. These induced dipoles may undergo a normal molecular vibration thus emitting radiation. The following discussion assumes that the scattering molecule is 'regarded as a collection of atoms undergoing simple harmonic motion' [39]. For small fields, the induced dipole moment μ_i is proportional to the electric field vector

$$\mu_i = \alpha \boldsymbol{E}, \tag{3.6}$$

where α is the polarizability of the molecule. The polarizability is a measure of the capability of inducing a dipole moment by an electric field and determines the deformability of the electron cloud of a molecule by an electric field. Eqn. 3.6 can be written in matrix form as

$$\begin{bmatrix} \mu_x \\ \mu_y \\ \mu_z \end{bmatrix} = \begin{bmatrix} \alpha_{xx} & \alpha_{xy} & \alpha_{xz} \\ \alpha_{yx} & \alpha_{yy} & \alpha_{yz} \\ \alpha_{zx} & \alpha_{zy} & \alpha_{zz} \end{bmatrix} \begin{bmatrix} E_x \\ E_y \\ E_z \end{bmatrix} \tag{3.7}$$

Note that since both μ_i and $\boldsymbol{E}$ are vectors, α is generally a tensor. In this case α is called the polarizability tensor, which plays key roles in Rayleigh and Raman scattering. The tensor is defined by an array of nine components α_{ij}. It is symmetric, that is, the off-diagonal components are related by

$$\alpha_{xy} = \alpha_{yx} \qquad \alpha_{yz} = \alpha_{zy} \qquad \alpha_{zx} = \alpha_{xz} \tag{3.8}$$

Thus the tensor has at most six distinct components, three off-diagonal and three diagonal. The visualization of the tensor is possible by forming an associated ellipsoid, using the six components, i.e.,

$$\alpha_{xx}X^2 + \alpha_{yy}Y^2 + \alpha_{zz}Z^2 + 2\alpha_{xy}XY + 2\alpha_{yz}YZ + 2\alpha_{zx}ZX = 1 \tag{3.9}$$

The ellipsoid of Eqn. 3.9 represents the molecular polarizability. Particularly, if the coordinate axes coincide with the principal axes X, Y, and Z of the ellipsoid then

Eqn. 3.9 reduces to a simpler form

$$AX^2 + BY^2 + CZ^2 = 1 \tag{3.10}$$

where $\alpha_{xy} = \alpha_{yz} = \alpha_{zx}$=0 and the diagonal components α_{xx}=A, α_{yy}=B, and α_{zz}=C, are called the principal values of the molecular polarizability.

The electrical field generated by the incident radiation with time is described as

$$E = E_0 \cos 2\pi\nu_0 t \tag{3.11}$$

where ν_0 is the frequency of the incident radiation and E_0 is the amplitude of the electric field for the material. Eqn. 3.6 and Eqn. 3.11 combine to give the induced fluctuating dipole moment

$$\mu_i = \alpha_k E_0 \cos 2\pi\nu_0 t \tag{3.12}$$

The polarizability of electrons in the molecule will be modulated by molecular vibration [126] so that

$$\alpha_{ij} = (\alpha_{ij})_0 + \sum \left(\frac{\partial \alpha_{ij}}{\partial Q_k}\right)_0 Q_k + \frac{1}{2} \sum \left(\frac{\partial^2 \alpha_{ij}}{\partial Q_k \partial Q_l}\right) Q_k Q_l + ..., \tag{3.13}$$

where $(\alpha_{ij})_0$ is the polarizability tensor in the equilibrium position, Q_k is the kth normal mode associated with vibrations of wavelength ν_k. If a molecule has simple harmonic vibrations near the equilibrium position, with a frequency ν_0 then higher order terms of Eqn. 3.13 can be ignored to give

$$\alpha_k = \alpha_0 + \left(\frac{\partial \alpha}{\partial Q_k}\right)_0 Q_k, \tag{3.14}$$

where Q_k is given by

$$Q_k = Q_k^0 \cos 2\pi\nu_k t, \tag{3.15}$$

with Q_k^0 being the normal coordinate amplitude and the superscript 0 refers to derivatives taken at the equilibrium configuration. Substituting Eqn. 3.15 into Eqn. 3.14 gives

$$\alpha_k = \alpha_0 + \left(Q_k^0 \cos 2\pi\nu_k t\right) \left(\frac{\partial \alpha}{\partial Q_k}\right)_0. \tag{3.16}$$

The expression of the total dipole moment is obtained by substituting Eqn. 3.16 into Eqn. 3.12, i.e.,

$$\mu_i = \alpha_0 E_0 \cos 2\pi\nu_0 t + \left(\frac{\partial\alpha}{\partial Q_k}\right)_0 Q_k^0 E_0 \cos 2\pi\nu_0 t \cos 2\pi\nu_k t. \tag{3.17}$$

Applying trigonometric sum rules $\cos(A)\cos(B) = \frac{1}{2}[\cos(A+B) + \cos(A-B)]$, Eqn. 3.17 can be expressed as

$$\mu_i = \alpha_0 E_0 \cos 2\pi\nu_0 t + \left(\frac{\partial\alpha}{\partial Q_k}\right)_0 Q_k^0 E_0 \times \left[\cos 2\pi(\nu_0 - \nu_k)t + \cos 2\pi(\nu_0 + \nu_k t\right]. \tag{3.18}$$

The first term $\alpha_0 E_0 \cos 2\pi\nu_0 \mathrm{t}$ of Eqn. 3.18 is the elastic Rayleigh scattering, which is at the same frequency as the incident radiation. The second term and the third terms are Stokes and anti-Stokes scattering, which occur at $\nu_0 - \nu_k$ and $\nu_0 + \nu_k$, respectively. In addition, the fact that $\left(\frac{\partial\alpha_{ij}}{\partial Q_k}\right)_0$ is generally much smaller than α_0 in Eqn. 3.18 implies that Raman scattering is much weaker than Rayleigh scattering and thus must be carefully measured. In practice, anti-Stokes lines are also appreciably less intense than the corresponding Stokes lines and as a consequence, Raman spectroscopy uses only the Stokes part of the spectrum.

The intensity of the Raman scattering is given by

$$I_R = \mu\left(\nu_0 \pm \nu_k\right)^4 \alpha_k^2 Q_k^2 \tag{3.19}$$

where μ is a constant. The intensity of Eqn. 3.19 is expressed in watts and it varies with the fourth power of the observed frequency for normal Raman scattering. Furthermore, the intensity of the scattered light is also proportional to the square of the derived tensor α_k also known as the Raman tensor and is expressed as

$$\alpha_k = \left(\frac{\partial\alpha_{ij}}{\partial Q_k}\right)_0 \tag{3.20}$$

If $\left(\frac{\partial\alpha_{ij}}{\partial Q_k}\right)_0 \neq 0$ then the polarizability must change during vibrations making the excited molecule Raman active. Note that modern Raman spectrometers use photons/second to measure the intensity instead of watts. Frequency is often expressed

in terms of wavenumbers (a wavenumber is the number of waves in a 1 cm-long wave-train, representing radiation energy) rather than Hertz, using $\overline{\nu} = \frac{\nu}{c} = \lambda^{-1}$, where c is the speed of light, λ the wavelength, and λ^{-1} is the wavenumber of the radiation. In addition, the photon energy is related to the wavenumber by E= hc$\overline{\nu}$. For instance, using this equation, one can compute the corresponding energy of a wavenumber of 1000 cm^{-1}. Its value is 2.0×10^{-20} J or 0.12 eV which is found using the conversion constant hc = 2.0×10^{-23} J cm.s, where h is Planck's constant (6.626×10^{-34} J.s).
Hence Eqn. 3.19 can be written as

$$I_R = \mu' \left(\overline{\nu}_0 \pm \overline{\nu}_k\right)^4 \alpha_k^2 Q_k^2, \tag{3.21}$$

where the factor c^4 is contained in the constant μ'.
The Raman shift $\overline{\nu}_k$ (in cm^{-1}), also labelled as $\Delta\overline{\nu}_k$, is the abscissa of the Raman spectrum and is defined as the difference in wavenumbers (cm^{-1}) between the observed radiation and that of the exciting source. Similarly, the ordinate is proportional to the intensity of the Raman scattering, with arbitrary units.

The classical theory of Raman spectroscopy has many limitations. Although it can be applied succesfully for qualitative analysis of molecular vibrations, it cannot simply be applied to molecular rotations and it is not able to identify clearly the relative intensities of the corresponding Stokes and anti-Stokes Raman lines, which is tackled in the quantum mechanical approach.

Quantum mechanical approach

The quantum mechanical approach is based on time-dependent perturbation theory where the Raman scattering can be considered as a light-matter interaction. In this process, the incident photon interacts with the phonon in the matter, which can either be in vibrational or rotational modes or a combination of both.

The vibrational and rotational energies of a molecule are quantized according to

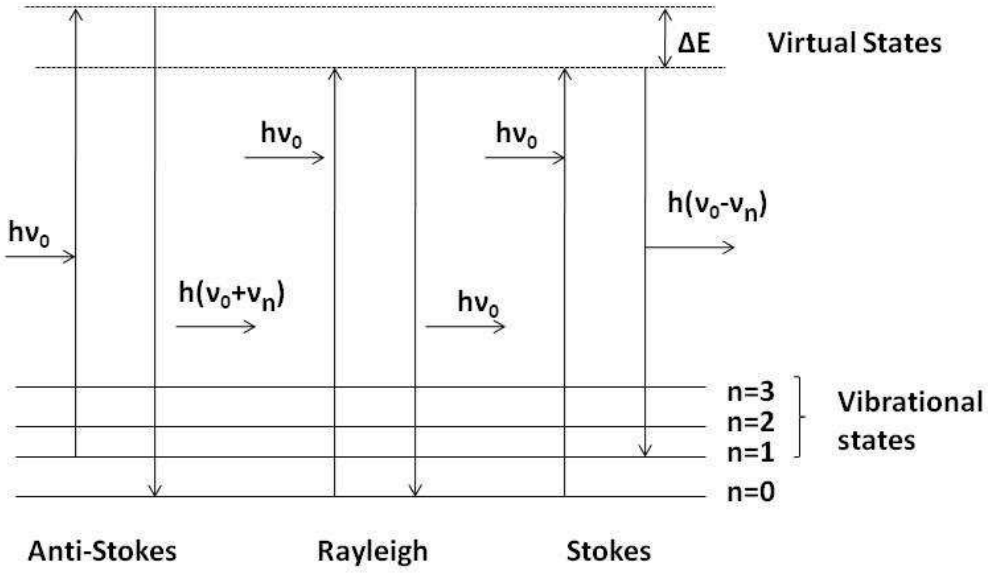

Figure 3.12: Illustration of the vibrational energy level transitions, induced by a photon of energy hν_0, redrawn after [40].

Eqn. 3.22, that is,

$$E_\nu = h\nu\left(n + \frac{1}{2}\right) \tag{3.22}$$

where n = 0, 1 ,2 ,3, ... is the quantum number.

The Raman effect can be considered as a two-photon process whereby a photon of incident radiation is absorbed or emitted by a molecular system as a result of an upward or downward transition between two energy levels (See Figure 3.12 [39]).

Overall, the permitted transitions obey the selection rule ΔJ = 0, $\pm$ 2 where ΔJ = 0 corresponds to Rayleigh scattering, ΔJ = 2 corresponds to Stokes scattering (phonon creation) and ΔJ = -2 corresponds to anti-Stokes scattering (phonon annihilation) where J is the total angular momentum quantum number.

As shown in Figure 3.12, Rayleigh scattering occurs when the energy of the scattered photon is the same as that of the incident photon (the excited vibration returns to its initial level). Stokes Raman scattering is created when the energy of the scattered photon is lower than that of the incident photon (the photon frequency decreases from ν_0 to ν_0-ν_n). In anti-Stokes Raman scattering, the energy of the scattered photon is higher than that of the incident photon (the photon frequency increases from ν_0 to ν_0+ν_n). This is possible because the molecular system may be initially in an excited state and then makes a transition from a virtual state[1] to a lower energy state.

The relative intensity between the Stokes and anti-Stokes Raman lines is given by

$$\frac{I_{Stokes}}{I_{anti-Stokes}} = \frac{I_{\overline{\nu}_0-\overline{\nu}_k}}{I_{\overline{\nu}_0+\overline{\nu}_k}} = \frac{\left(\overline{\nu}_0-\overline{\nu}_k\right)^4}{\left(\overline{\nu}_0+\overline{\nu}_k\right)^4} exp\left(\frac{hc\overline{\nu}_k}{k_BT}\right) \tag{3.23}$$

Eqn. 3.23 makes it possible to determine the temperature of the sample by contact-free measurements.

Instrumentation

This section describes the Raman spectrograph used in our Raman scattering measurements. In addition, a brief description of the laser source and the sample illumination is itemized below.

• The source used is a laser source of intense, coherent monochromatic radiation. The argon ion-laser with excitation wavelength of 514.5 nm was used throughout this work. Note that the argon ion (wavelength of 488.0 or 514.5 nm) and the Krypton ion (wavelength of 530.9 or 647.1 nm), which emit in the green and the blue region of the spectrum, respectively, have advantage over other sources (for instance, Helium-neon, Diode, Nd-Yag) due to the fact that the Raman scattering varies as the fourth power of the frequency.

[1] An imaginary transition state which does not correspond to an eigenstate of the molecule, a practical convenience by which the energy exchange between the radiation field and the molecule during the scattering process can be split-up into one-photon transitions [130]

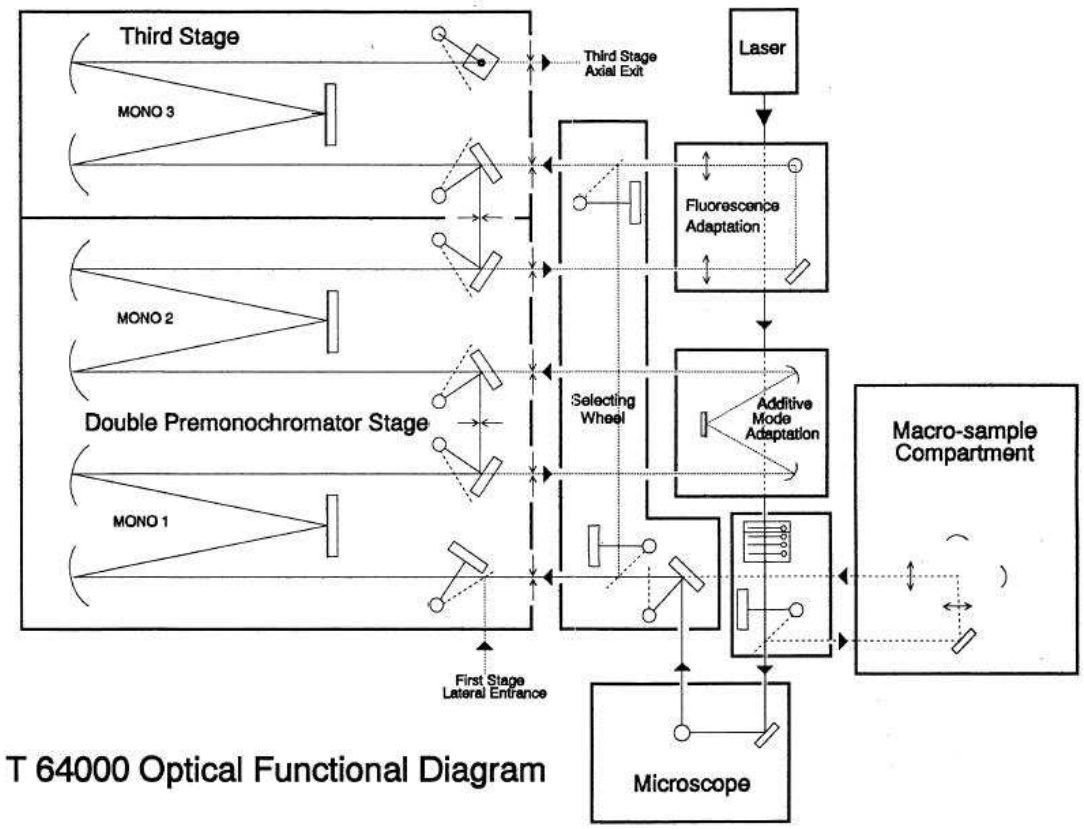

Figure 3.13: Schematic diagram of the Jobin-Yvon T64000 spectrograph showing the beam path. From Jobin-Yvon T6000 Raman Spectrograph Instructional manual.

• The sample illumination system used consists just of ordinary glass.

• The Raman spectrograph Jobin-Yvon T64000 (See Figure 3.13) uses dispersive Raman whose role is to separate the weak Raman scattered light from the Rayleigh-scattered light. The laser light is directed into the spectrometer by optical mirrors. The filtered beam of light is then focused on the sample using an Olympus BX40 microscope attached to the spectrograph, using either an ultra long working distance 50X objective or 100X objective. A narrow band-pass filter removes unwanted laser plasma lines and allows only the selected wavelength into the microscope. The scattered light from the sample is directed into the spectrometer, capable of measuring

the distribution of a signal in a particular wavelength and processing it in single spectrograph mode, triple substractive mode or triple additive mode. Raman spectra were acquired in this study with the aid of Jobin-Yvon T64000 Raman spectrometer, operated in single spectrograph mode. The 1800 grooves/mm grating was preferred over the 600 lines/mm grating because the former has the highest spatial resolution though it has a narrow spectral range compared to the latter grating. The Jobin-Yvon T64000 spectrometer, being a triple monochromator dispersive system, disperses light via the gratings onto a liquid nitrogen cooled CCD detector, which detects the scattered light and produces a Raman spectrum. The Raman data collection is done through Labspec 4.18 scientific software, supplied by Jobin-Yvon for further analysis. The following details are worth mentioning: All the Raman experiments were carried out at room temperature, the beam spot diameter and the beam power used were $\sim$ 1 μm and 150 mW, respectively. Furthermore, a microscope with a 100X objective was used while a nitrogen cooled CCD detector is often used for optimization.

3.7.2 Transmission Electron Microscopy

Introduction

Transmission electron microscopy (TEM) is a useful method for characterizing the radiation effects in crystals. Particularly, its strength and reliability come from the easy access to its results, that is, it gives direct images of the radiation damage under investigation.

Basic principles

The electron microscope can be considered as an update of visible-light microscopes, with the former exploiting the wave properties of electrons to improve over the maximum resolution of the latter which is limited to about 200nm. The resolution of a visible-light microscope is described as '*the minimum distance between two points at*

which they can be visibly distinguished as two points' [133] and is given by the Abbe equation i.e.,

$$R = \frac{0.61\lambda}{n \sin \alpha} \tag{3.24}$$

where λ is the wavelength of the radiation, α is the half-angle (angular aperture of the lens) subtended by the objective lens at the object, and n is the refractive index of the medium between the object and the objective lens. The product $n\sin\alpha$ is called numerical aperture (NA) and it is '*an important characteristic of any objective lens system*' [123]. Eqn. 3.24 suggests the use of shorter wavelengths of the visible light ($\sim$ 400nm) and larger numerical aperture ($\sim$ 1.3 for an oil-immersion objective lens system) to achieve greater resolutions. Thus, the best resolution of a visible light microscope is about 0.2 μm.

WAVE PROPERTIES OF ELECTRONS

An electron beam generated by an electron gun can be focused with the help of electromagnetic lenses, due to the particle-like and wave-like character of electrons. The dual wave-particle nature of electrons is expressed by the de Broglie relationship for the wavelength of any particle, that is,

$$\lambda = \frac{h}{m\nu}, \tag{3.25}$$

where h is the Planck's constant, m and ν are the mass and the velocity of the particle, respectively. The electron energy (in Joules) is given by

$$eV = \frac{m\nu^2}{2}, \tag{3.26}$$

where e is the charge of the electron. Substituting Eqn. 3.26 into Eqn. 3.25 leads to the non-relativistic electron wavelength equation, that is,

$$\lambda = \frac{h}{\sqrt{2meV}}. \tag{3.27}$$

At accelerating voltages higher than 100 keV, the relativistic correction should be taken into account in the de Broglie Eqn. 3.28 to give

$$\lambda = \frac{h}{\sqrt{2meV\left(\frac{1+eV}{2m_0c^2}\right)}}, \tag{3.28}$$

where c and m_0 are the velocity of light and the rest mass of electron, respectively. Note that the non-relativistic and the relativistic wavelengths associated with a transmission electron microscope whose accelerating voltage is 100 keV, for instance, can be obtained from Eqns. 3.26 and 3.28 and are 0.0386 Å and 0.0370 Å, respectively [122]. The corresponding resolvable power of an ideal transmission electron microscope, that is, one which does not have aberrations, is about 2 pm which is less than the Bohr radius of the atom. Thus, resolution in that range should image individual atoms, making transmission electron microscopes one of the powerful and versatile instruments used for the microstructural characterization of materials. In practice, notable aberrations of the objective lens are the spherical, chromatic and astigmatism which limit the divergence angle of the beam for a sharp focus to a small fraction of a degree [123]. These aberrations reduce the just-calculated fine resolution of an ideal transmission electron microscope from about 2 pm to about 0.2 nm.

INSTRUMENTATION

A modern transmission electron microscope comprises an illumination system, an objective/stage and the imaging system. A block diagram of such a transmission electron microscope highlighting its main components is shown in Figure 3.14 [135].

The illumination system comprises the electron gun and the condenser lenses. The electron gun is the main component of the illumination system which emits electrons by such as a lanthanum hexaboride (LaB_6), a zirconium oxide/tungsten (Zr/W) Schottky or a tungsten field emission source. Tungsten field emission is used where high coherence lattice imaging, high gun brightness and high spatial resolution microanalysis are needed. As for the condenser lenses, they form a fine probe

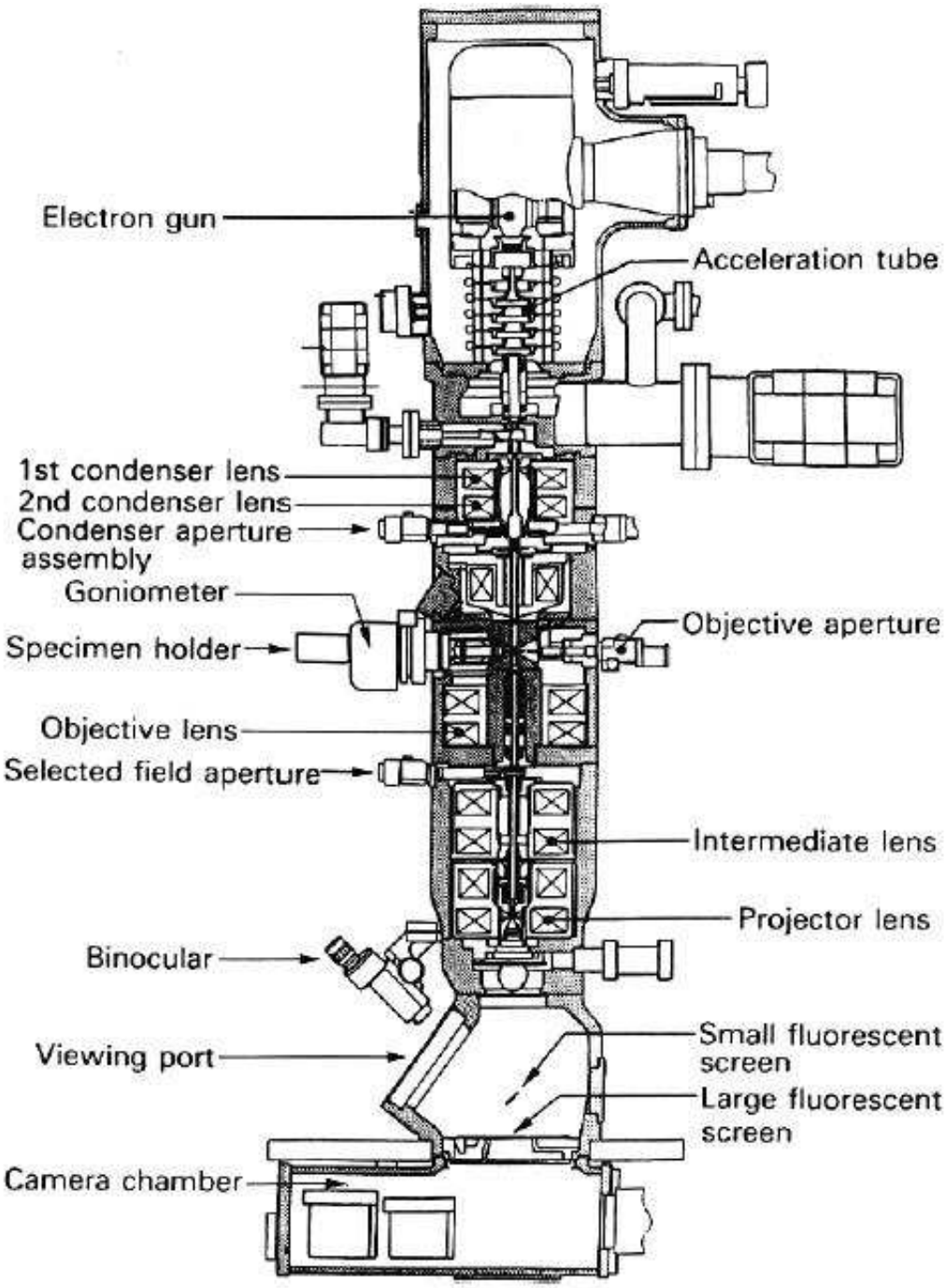

Figure 3.14: A block diagram of a TEM [135].

(broad/focused beam of electrons) taken from the gun and transfer it to the specimen. The illumination system can be operated in two principal modes, i.e., parallel and convergent beam. The former mode is used primarily for TEM imaging and selected-area diffraction (SAD), while the latter is used mainly for scanning (STEM) imaging via electron spectroscopy and convergent-beam electron diffraction (CBED).

The objective and the specimen stage system are the heart of the TEM where all the beam-specimen interactions take place. In addition, the objective lens determines the limit of image resolution, and is therefore key to the TEM process.

The imaging system consists of intermediate and diffraction lenses whose role is to magnify the image or diffraction pattern (DP) produced by the objective lens. The magnified image or DP is then projected with the aid of a projector lens onto a viewing screen. The recording of the image/DP is done either by direct exposure of a photographic emulsion or an image plate inside the vacuum or via a charge coupled device (CCD) camera while awaiting the quantitative data processing.

Furthermore, chemical analysis can be done using both energy-dispersive X-ray spectroscopy (EDS) and electron energy loss spectroscopy (EELS). The latter not only provides local chemical information but also electronic structure of the specimen via plasmon excitations and core electron excitations.

IMAGING MODES OF A TEM

Electrons interact strongly with thin-film specimen by elastic and inelastic scattering (See Figure 3.15 [123]), but the elastic scattering is more important in that it dominates the contrast observed in the transmission electron microscope. Three types of contrast are worthwhile noting. The first is the diffraction contrast, also called amplitude or strain contrast, which measures the intensity of diffracted waves across a thin specimen. The diffraction contrast (bright-field and dark-field images) is commonly used in radiation damage studies [136]. The second is the phase contrast performed in atomic resolution microscopes whereby the phase of the diffracted electron wave is

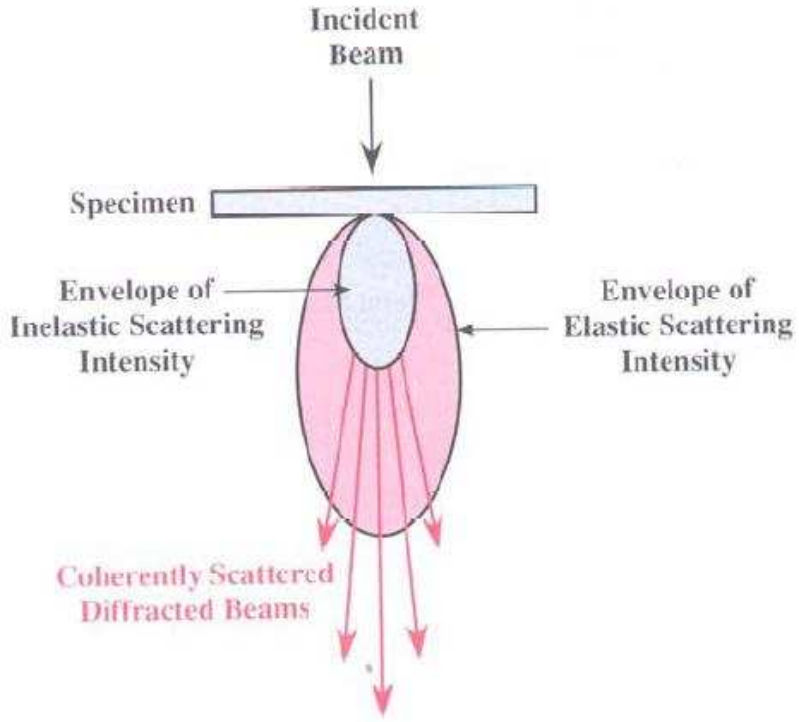

Figure 3.15: Schematic diagram of the electron scattering processes [123].

'*preserved and interferes constructively or destructively with the phase of the transmitted wave*' [135]. The phase contrast is particularly sensitive to atom distribution in the specimen thus making it possible to image directly the crystallographic lattice itself which is useful for discovering crystallographic details of the nature of the defects. The last one is the mass thickness or atomic number contrast which is due to variations in mass-thickness and mostly performed in STEM when dealing, for instance, with biological soft tissues samples.

Dark-field and Bright-field Imaging

Dark-field and bright-field imaging are termed conventional imaging contrary to the phase contrast imaging performed in HRTEM. On the one hand, the bright-field imaging consists of masking all diffracted beams of electrons by the objective aperture and hence only the direct transmitted (un-diffracted) beam is used for the imaging

process. As the electrons interacting with the defects deflect away, the defects appear dark on a bright image background. The dark-field imaging on the other hand involves selecting one of the diffracted beams of electrons. The diffracted beam interacts with the atoms or defects of the thin film specimen sample thus making the defects appear bright on a dark image background. The dark-field imaging intensity is lower than that of the bright-field imaging and this results in better contrast [137]. It is worth mentioning that good strong diffraction in both bright-field and dark-field images can be obtained under two-beam conditions, also called 'strong' two-beam conditions. In these conditions, the foil is tilted to allow one set of diffracting planes at or very close to the Bragg condition [136]. In addition, complementary contrast under two-beam conditions, which is sensitive to weak lattice strains, yields to symmetry and dislocation loop investigations.

Selected-Area diffraction (SAD)

The basic ideas of electron diffraction are based on Bragg's diffraction law, that is,

$$n\lambda = d_{hkl} sin\theta, \tag{3.29}$$

where n is an integer, λ is the incident wavelength of the electron beam, d_{hkl} is the inter-planar spacing and θ is the diffraction angle. Selected-area diffraction (SAD) is particularly useful because it allows direct correlation between the structural image and the electron diffraction pattern (DP). But thin samples of less than 100 nm are required to obtain transmission diffraction as a result of the weak penetrating power of electron beams [43]. In addition, it is known that electron diffraction is not very sensitive to minute amounts of amorphous components incorporated in a diamond substrate, thus EELS is recommended in such cases as it has the ability of distinguishing changes in the carbon bonding configurations [43]. Most importantly, the separation of the diffraction spots on the viewing screen can be used in the determination of the inter-planar spacing in crystals. Figure 3.16 [122] illustrates the geometry of a selected area diffraction pattern, showing the 'camera-length' L, the

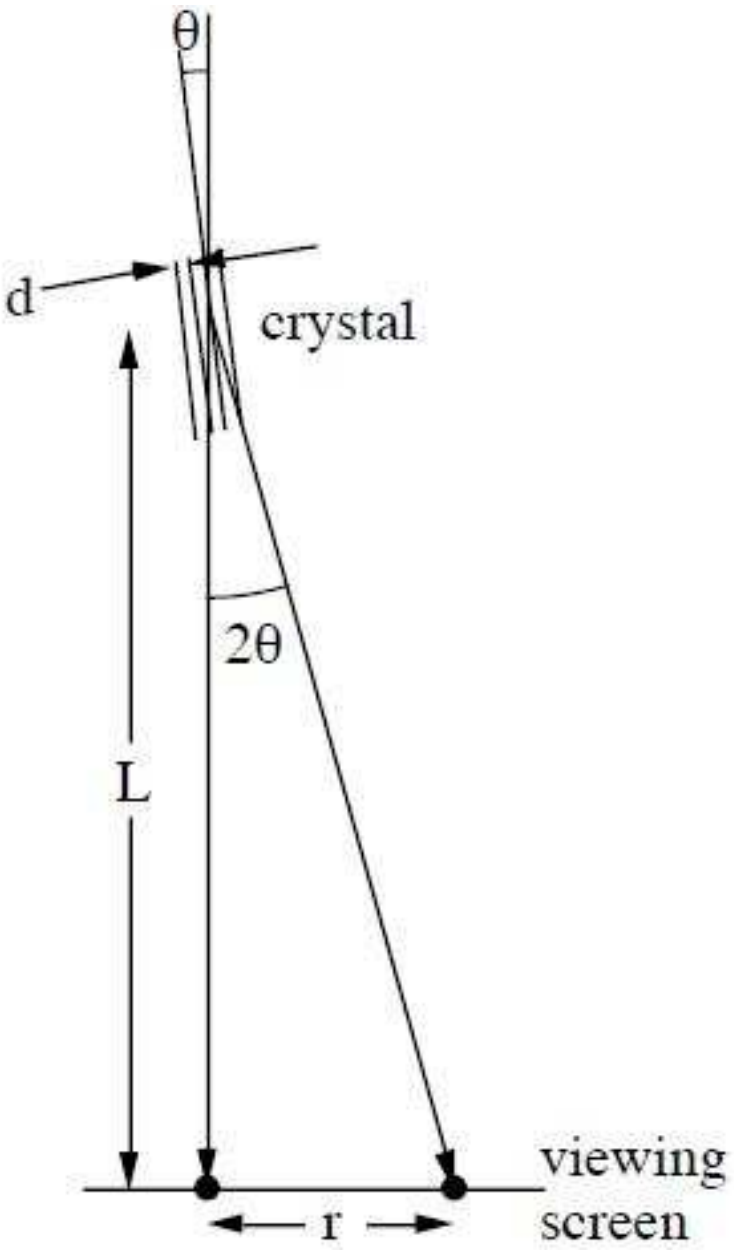

Figure 3.16: Schematic diagram of the geometry of a selected area diffraction [122].

distance between the crystal and the photographic plate of the camera. Applying Bragg's law, we have:

$$2d \sin\theta = \lambda \tag{3.30}$$

For small angles or low order diffraction,

$$\sin\theta \sim 1/2 \tan 2\theta \tag{3.31}$$

According to the geometry of Figure 3.16,

$$\tan 2\theta = \frac{r}{L} \tag{3.32}$$

Substituting Eqn. 3.32 into Eqn. 3.31 and then into Eqn. 3.30 provides the 'camera equation':

$$rd = \lambda L \tag{3.33}$$

where λL is the 'camera constant'. It is easy to see that knowing the camera constant λL, the inter-planar spacing can be determined by measuring the separation of diffraction spots, r. Furthermore, the indexing of diffraction patterns is made possible by measuring the angle between the spots.

HIGH RESOLUTION TRANSMISSION ELECTRON MICROSCOPY

While conventional TEM imaging uses the diffraction contrast which measures the intensity of the diffraction waves, high resolution transmission electron microscopy (HRTEM or HREM) based on the phase-contrast imaging uses both transmitted and diffracted beams, which interfere with each other to image directly the crystallographic lattice of a thin-film specimen [43]. Thus crystallographic details of the nature of the radiation damage can be ascertained. Note that HRTEM requires very thin samples of about 20 nm thick so as to get atomic structural information. For instance, in this work, ion milled diamond samples viewed previously using conventional TEM were further milled to meet HRTEM requirements.

ELECTRON ENERGY LOSS SPECTROSCOPY

Electron energy-loss spectroscopy (EELS) involves measuring the energy distribution of electrons that have traversed a thin specimen in a TEM. This is achieved by

mounting a magnetic-prism spectrometer, also called the magnetic sector, after the projector lenses of a TEM which acts as a prism to separate electrons of different energies. Electrons which lose energy to the specimen move more slowly in the magnetic sector and thus are the most deflected. It is only electrons with a particular energy that are deflected through the slit placed just at the focal plane of the magnetic sector of a 'serial spectrometer'. A scintillator mounted after the slit records the intensity of the electrons that have passed through the slit. Note that 'parallel spectrometers', best known in Parallel-Collection EELS (PEELS) are the most used in that they have a greater rate of data acquisition than the 'serial' ones. In addition, PEELS gathers simultaneously the whole energy range unlike 'serial' spectrometers which used to record sequentially each energy loss channel slowly and tediously [122]. In a typical EELS spectrum, the distribution of the electron intensity measured in arbitrary units (a.u) is plotted against the energy loss measured in eV. The most prominent feature in an EELS spectrum is the zero-loss peak corresponding to purely elastic scattering. Inelastic scattering is divided into low-loss and core-loss regions of the rest of the spectrum. The core-loss regions correspond to higher energy of the order of 30-800 eV and imply the ionization of atoms via core excitations. Low-loss regions relate to plasmon scattering of the order 10-30 eV which involves the promotion of interband transitions from occupied valence states to conduction states. The theoretical plasmon energy is predicted by the free-electron model [135]:

$$E_p = \hbar\omega_p \tag{3.34}$$

with

$$\omega_p = \left(\frac{4\pi e^2 \rho}{m_e}\right)^{\frac{1}{2}} = 5.64 \times 10^4 (\rho)^{\frac{1}{2}} \tag{3.35}$$

where ω_p is the plasmon frequency, e is the electron charge, ρ the electron density [electrons per m^3] and m_e the effective mass of the electron. Combining Eqn. 3.34 and Eqn. 3.35 leads to:

$$E_p = \hbar \times 5.64 \times 10^4 (\rho)^{\frac{1}{2}} \tag{3.36}$$

For CVD diamond, the bulk plasmon peak energy has been observed experimentally at 33 eV [138]. From Eqn. 3.36, one can see that the plasmon energy is affected by the free-electron density and its knowledge can help in identifying the different phases of carbon.

Chapter 4

Results and Discussion

4.1 Layout of the Chapter

This chapter presents and discusses the computer simulations performed before the implantation, to predict the spatial and distribution of the damage final ion concentration of carbon into diamond, together with the experimental findings obtained using complementary characterization techniques such as transmission electron microscopy and Raman spectroscopy.

4.2 Simulation of ion implantation

Computer simulations of the ion-implantation process were done with the SRIM [139](Stopping and Range of Ions in Matter)-2008 computer package, using a value of 50 eV [6] for the displacement energy, to simulate the ion range and damage distributions produced by the carbon ion multi-implantation, whose parameters are given in Table 3.1. The Transport and Range of Ions in Matter (TRIM), and, by extension SRIM package, is known to '*statistically follow the trajectories of many ions shot into the target material, by not only calculating the collision history of each ion with the target atoms during the slowing down, but also by accumulating the vacancies and*

interstistials thus created, yielding, among others, absolute values of the amount and depth profiles of damage caused by ion-implantation to a given fluence' [89]. It is, thus, desirable, if not essential in any radiation damage experiment to know before implantation, the spatial distribution of both the damage and final ion concentration, especially after Prawer et al.[140] have shown that the SRIM computer package is most applicable for low-temperature implantations (where diffusion is minimized) as performed in this study.

However, one should bear in mind that SRIM overestimates the implant and damage ion concentration as it does not take into account the following: the channelling of ions, the binary collisions, the recombination of point defects, the phase changes and the thermal annealing [11]. Figure 4.1 shows the vacancy distribution produced by the carbon ion multi-implantation into diamond.

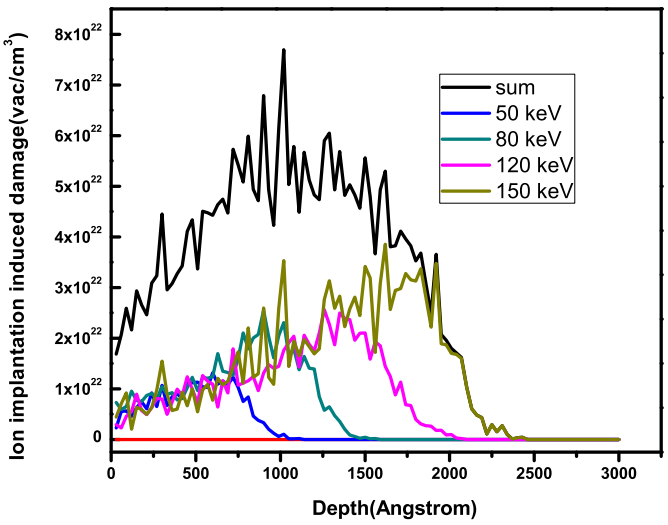

Figure 4.1: A SRIM-2008 derived damage density produced by the carbon ion multi-implantation into diamond whose parameters are given in Table 3.1 and calculated for a total fluence of $7\times\ 10^{15}$ ions cm^{-2}.

Summing up the vacancy distributions of all the implants which comprise the multi-implantation recipe versus the depth, gives the resultant vacancy distributions. One can see from Figure 4.1 that the average damage density is roughly the same from the surface to about 2000 Å while the average projected range predicted by the Monte Carlo program or the width of the implanted layer is $\sim$ 2500 Å. In addition, the mean depth of implanted carbon ions, with mono-energies between 100 and 300 keV, into carbon targets is about 1000-3000 Å [11], thus making keV implantations a near-surface phenomenon as opposed to MeV implantations where damage is buried deeper in the specimen of the order of few μm due to the fact that implantation energies control depth profiles.

4.3 Conventional transmission electron microscopy

All the cross-section transmission electron microscopy (XTEM) and one plan-view specimens were examined using conventional bright-field and electron diffraction techniques in a 200 keV Philips CM20 TEM (Transmission Electron Microscope). Some of the XTEM specimens were prepared using a conventional preparation method, that is, mechanical thinning followed by ion milling and the other specimens were prepared using the lift-out FIB-SEM (Focused Ion Beam-Scanning Electron Microscope) technique. It is known that the electron beam used in TEM analyses, apart from providing useful structural information, may also introduce some unwanted radiation damage in the surface or bulk structure of a specimen thus altering its desired properties. In this regard, Koike et al.[141] have shown that the displacement of carbon atoms by an incident electron beam along the <110> direction only takes place above an accelerating voltage of 200 keV. Thus, all the thin diamond slices used in this study, which fulfilled this condition, were imaged safely in the 200 keV Philips CM20 TEM.

4.3.1 X-TEM results of unimplanted, as-implanted and implanted and annealed samples obtained using conventional preparation methods.

The TEM image in Fig. 4.2 of unimplanted HPHT (High-pressure, high-temperature) synthetic diamond type Ib exhibits a high density of ripples most likely created by the argon ion milling process. These artifacts introduced by the argon ion milling may contribute to misleading interpretation of X-TEM results as observed in the present investigation.

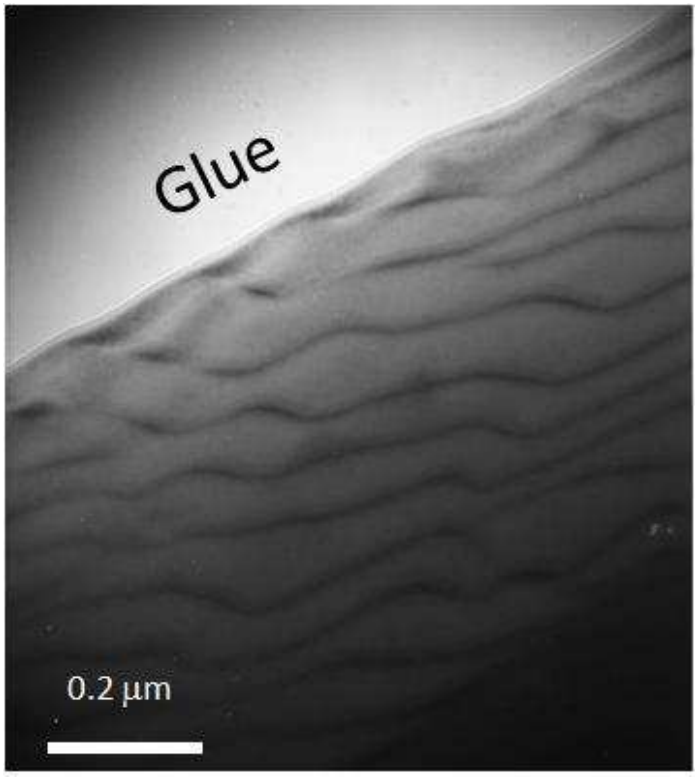

Figure 4.2: Cross-sectional bright-field TEM image of unimplanted type Ib HPHT synthetic diamond. The surface region of the diamond contains a high concentration of ripples. A two-beam diffraction condition was used to record the image.

The TEM micrograph of etched/cleaned C^+-implanted diamond (HPHT, type Ib), to a low fluence of 5×10^{15} ions cm^{-2} and annealed at 1600K (CIRA, that is, implanted at LN_2 and rapid thermally annealed to 1600 K) in Figure 4.3 (a) does not exhibit any visible defects due to the ion implantation and annealing. The etching/cleaning process consisted of boiling the damaged diamond in an oxidising acid solution for 15-30 min and rinsing in deionised water. In the case of the as-implanted diamond with carbon ions to a high fluence of 6×10^{15} ions cm^{-2} and unannealed shown in Figure 4.3 (b), the implantation damage in the form of a dark band is clearly visible. The middle of the dark band is about 0.2 μm from the implanted surface. The dark band was analysed by using electron diffraction (see insert) and found to be crystalline rather than amorphous.

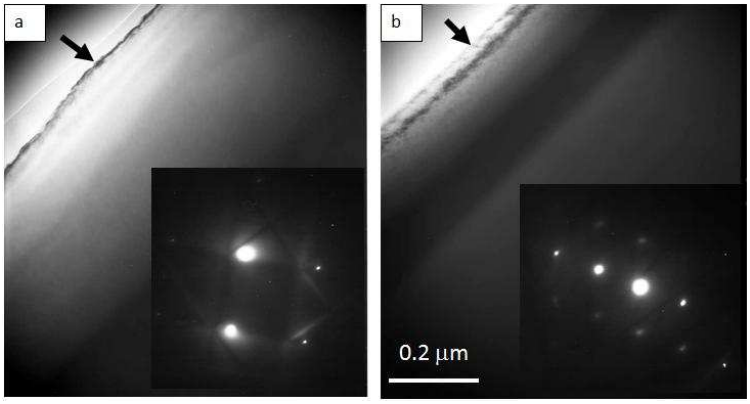

Figure 4.3: (a) Cross-sectional bright-field TEM images of etched C^+-implanted diamond to a low fluence of 5×10^{15} ions cm^{-2} and annealed at 1600K and (b) Cross-sectional bright-field TEM images of etched C^+-as-implanted diamond to a high fluence of 6×10^{15} ions cm^{-2} and unannealed or rather warmed to room temperature. The corresponding selected area diffraction patterns are shown in the inserts. The implanted surfaces are indicated by the arrows. The white line (fringe) through the arrowhead of Figure 4.3 (a) is a result of an out-focus image. Two-beam diffraction conditions were used for both images.

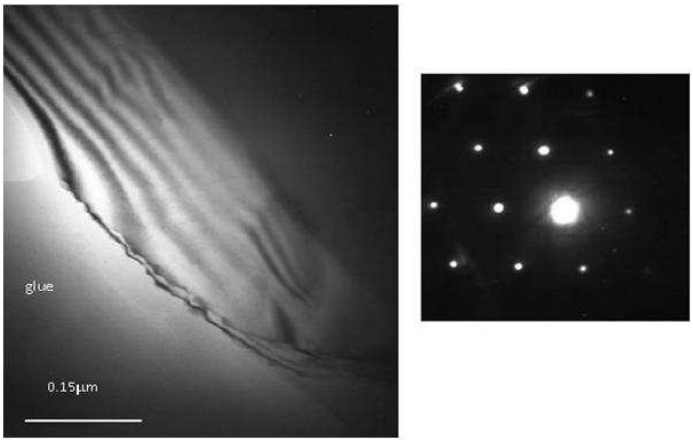

Figure 4.4: Cross-sectional bright-field TEM micrograph of unetched C^+-implanted diamond to a fluence of $1\times\ 10^{15}$ ions cm^{-2} and rapidly annealed at 1600 K (CIRA) with corresponding selected area diffraction pattern. The sample has a wedge shaped edge as a result of ion milling and therefore show a number of thickness fringes close to the edge.

The TEM micrograph of unetched C^+-ion implanted diamond to a fluence of $1\times$ 10^{15} ions cm^{-2} in Figure 4.4 exhibits a number of thickness fringes but does not show any visible defects due to the ion implantation followed by annealing. Furthermore, the TEM micrograph of C^+-implanted diamond to a fluence of 1×10^{15} ions cm^{-2} in Figure 4.5 does not show any ion implantation damage. The defects visible as fringes close to the edge-consist of stacking faults and curved dark lines most likely caused by the argon ion thinning process.

Using the FIB-SEM method has revealed various defects including platelets and dislocation loops (See Figure 4.11). A FIB section was removed from the implanted and annealed type Ia diamond. This sample was already mounted on a TEM grid and ion milled using argon ion. The FIB section was removed from away from the electron transparent region. Both diffraction patterns show the reflections of diamond which indicate that the ion-implanted diamond to the low fluence of $1\times\ 10^{15}$ ions cm^{-2}

recovered its crystallinity upon annealing at 1600 K.

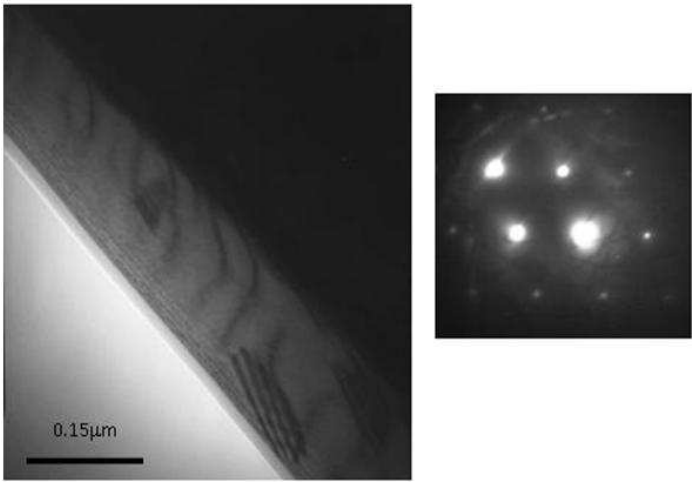

Figure 4.5: Cross-sectional bright-field TEM micrograph of unetched C^+-implanted diamond to a fluence of 1×10^{15} ions cm $^{-2}$ with corresponding selected area diffraction pattern. This is the same sample as in Fig. 4.4 but viewed at a different position. The sample has a thin region produced by ion beam thinning, showing - defects in the form of fringes close to the edge. The fringes consist of stacking faults and curved dark lines most likely caused by the argon ion milling process.

Figure 4.6 (a) shows a cross-sectional bright-field TEM image of an unetched C^+-implanted diamond to a high fluence of 7×10^{15} ions cm^{-2} at liquid nitrogen temperature and rapidly annealed at 1600 K.

Microdiffraction analysis of the implanted layer indicated that it was amorphous, however, it contains regions of nanocrystalline graphite, as evidenced by the 002 arcs of graphite in the selected area diffraction (SAD) pattern in Figure 4.6 (b). The SAD pattern was recorded by placing part of the aperture over the implanted layer only, excluding the single crystalline diamond substrate. The SAD pattern of the substrate in Figure 4.6 (c) shows the 111 reflections of diamond. The interface region between the amorphous implanted layer and diamond substrate has dark defect contrast which is due to the implantation damage at the tail of the projected ion range.

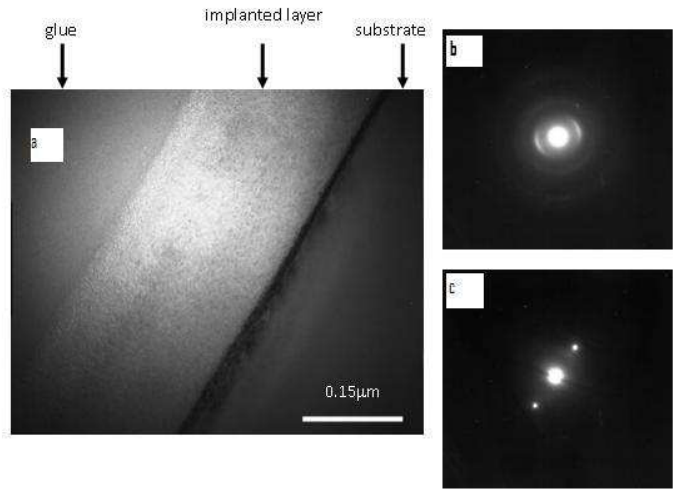

Figure 4.6: (a) Cross-sectional bright-field TEM micrograph of unetched C^+-implanted diamond to a fluence of 7×10^{15} ions cm^{-2} at liquid nitrogen temperature and rapidly annealed at 1600 K with SAD patterns from the implanted layer (b) and diamond substrate (c). The dark defect contrast at the interface region between the amorphous implanted layer and diamond substrate is due to the implantation damage at the tail of the projected ion range. The SAD pattern (b) from the amorphous implanted layer exhibits the 002 arcs of graphite. The SAD pattern of the substrate in (c) shows the 111 reflections of diamond.

4.3.2 Plan-view TEM results of ion beam thinned unimplanted samples acquired using conventional preparation methods.

Plan-view TEM investigations of as-implanted synthetic type Ib and un-implanted natural type Ia diamonds performed by using conventional thinning techniques had two-fold objectives: firstly the assessment of any radiation damage to the diamond lattice caused by both the ion milling process and transmission electron microscope procedure, and secondly to follow the evolution of as-implanted diamond surface,

which would be impossible to achieve with CIRA processed diamonds samples (which were rapid annealed after cold implantation.)

Figure 4.7 (a) corresponding to bright-field TEM micrograph of unimplanted synthetic HPHT type Ib diamond does not show any visible extended defects while Figure 4.7 (b) which represents bright-field TEM micrograph of natural type Ia unimplanted diamond shows a high density of platelets with no visible presence of line defects. Figure 4.7 (a) and (b) display broad dark lines in the image which are bend contours and thickness fringes which are more visible in the latter. The sharp diffraction pattern spots of Figure 4.7 (a) are characteristic of crystalline diamond thus ruling out any substantial damage inflicted to the sp^3 bonds during argon ion milling and transmission electron microscopy procedures.

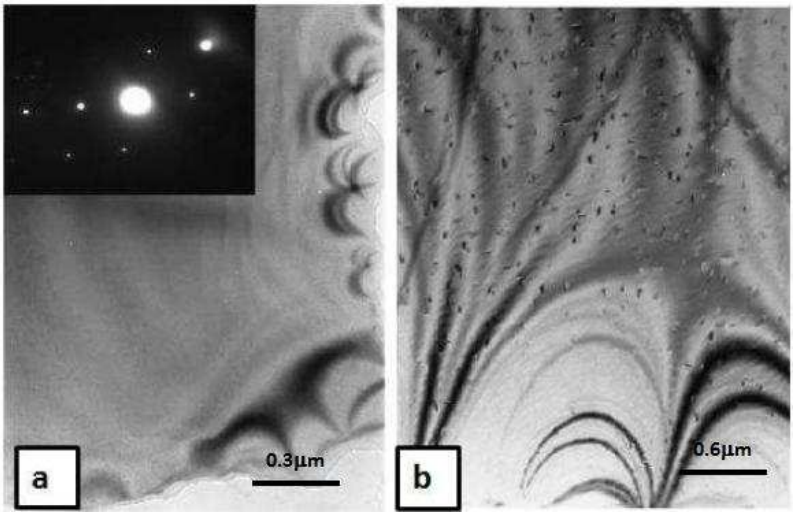

Figure 4.7: Bright-field TEM micrographs of unimplanted diamonds: (a) unimplanted synthetic HPHT diamond with corresponding selected area diffraction pattern in the insert. No extended defects are visible and the diffraction pattern spots are sharp. (b) Unimplanted natural diamond recorded in a thin region of the foil. A high density of platelets is visible. No dislocations are present. The broad dark lines in the image are bend contours and thickness fringes.

The TEM micrographs of unimplanted natural diamond (type Ia) shown in Figures 4.8 (a) & (b) are enlarged images recorded with two different operating reflections of the small platelets visible in Figure 4.7 (b). These figures show a high density of platelets, exhibiting the typical contrast of both edge-on and inclined platelets on {100} planes. The operating reflections in Figures 4.8 (a) & (b) are $\mathbf{g} = 111$ and $\mathbf{g} = 220$ respectively, with the electron beam along the <110> direction. These platelets observed in unimplanted type Ia diamond consist of planar defects which were generally thought in the sixties [142] to be entirely of nitrogenous origin but later found to be produced by the aggregation of self-interstitials [143] with a minute, but essential content of nitrogen [115].

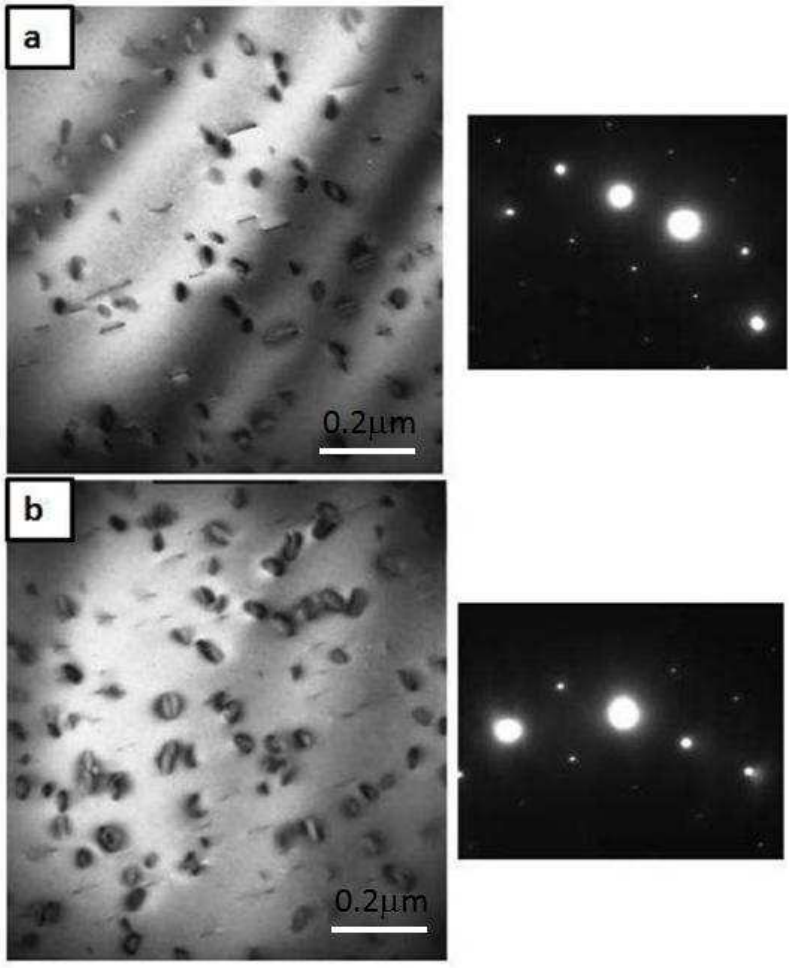

Figure 4.8: Bright-field TEM micrographs of unimplanted natural diamond (type Ia) with corresponding selected area diffraction patterns. A high density of platelets on {100} planes, showing the typical contrast of both edge-on and inclined platelets, is visible. The operating reflections are $\mathbf{g} = 111$ in (a) and $\mathbf{g} = 220$ in (b) with the electron beam along the <110> direction.

4.3.3 X-TEM results of as-implanted, low and high fluences C^+-implanted diamond samples obtained using FIB-SEM preparation method.

All transmission electron microscopy (TEM), High Resolution Transmission Electron Microscopy (HRTEM) and Electron Energy Loss Spectroscopy (EELS) specimens were prepared using a Helios Nanolab 650 FIB/SEM and the analyses were carried out in a double Cs-corrected JEOL-ARM 200F HRTEM equipped with a Quantum Gatan Image Filter.

The TEM bright-field micrograph in Figure 4.9 was acquired from a 3 mm disc of synthetic type Ib diamond. It was first ion milled and analysed in a TEM for the assessment of any radiation damage that might have occurred, caused by the ion milling process or by the electron beam of the transmission electron microscope. After ion milling and TEM analysis, the sample was then plan-view implanted with single energy of 150 keV carbon ions at RT. A low dose rate of 1.2 μA/cm^2 was used during implantation. Initial results of as-implanted diamond with high fluence of 7×10^{15} ions cm^{-2} near the edge of the milled hole, electron transparent regions, did not reveal any visible defects due to the ion irradiation. In addition, further away from the milled hole, there appeared to be some contrast, possibly due to the strain from the radiation damage in thicker regions of the sample. This prompted us to use FIB-SEM sample preparation method to extract a thin lamella from the implanted region of the sample away from the ion milled hole and further polished it down to about 50 nm so as to meet EELS and HRTEM very thin specimen requirements for advanced investigations. The X-TEM bright-field micrograph of Figure 4.9 revealed an 80.3 nm thick amorphous diamond layer within the ion irradiated volume following the breakage and/or distortion of the C-C bonds, in agreement with SRIM simulation shown in Figure 4.10. In addition, above the amorphous carbon zone one can see a

quasi- crystalline diamond layer, extending from the surface up to about 130 nm. No amorphous /graphitic tracks supposedly created during the passage of the carbon ions in the electronic stopping zone were observed as predicted by the Morehead and Crowder model [144]. This layer may consist of point defects which cannot be imaged by transmission electron microscopy.

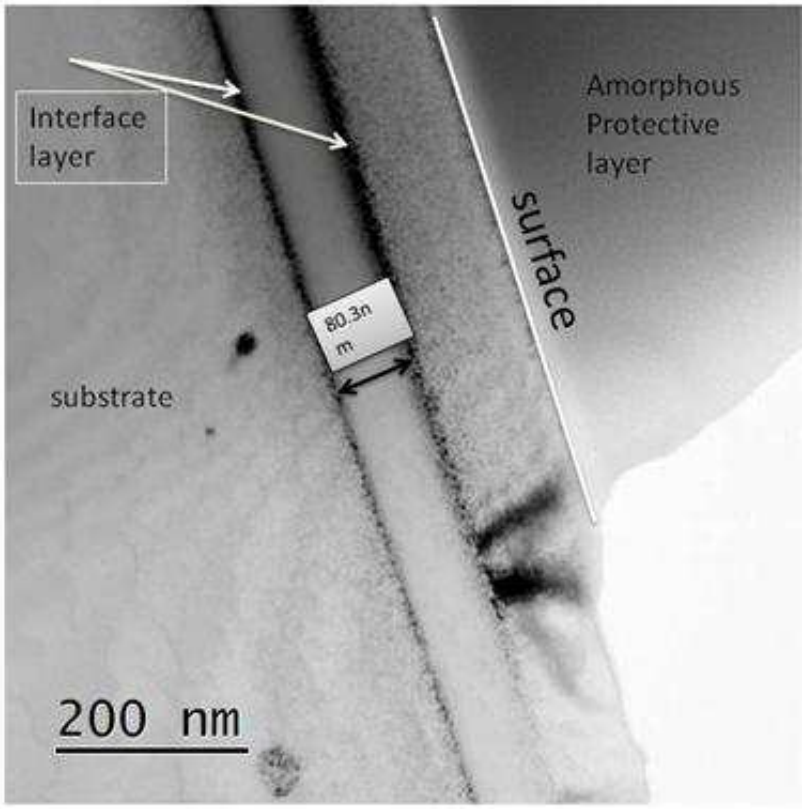

Figure 4.9: Cross-sectional bright-field micrograph of unetched C^+-as-implanted diamond (HPHT, type Ib) to a fluence of 7×10^{15} ions cm^{-2} showing an amorphous region 80.3 nm thick at a depth of about 130 nm.

The theoretical damage distribution plotted against the penetration depth was calculated with the aid of SRIM -2008 [139] and is presented in Figure 4.10. The average projected range predicted by the Monte Carlo program is about 250 nm, while the highest level of damage lies at a depth of about 160 nm. It is interesting to

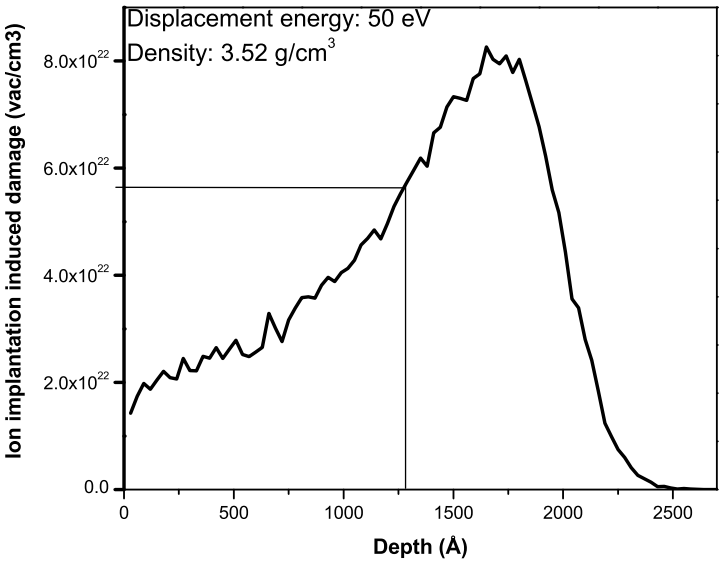

Figure 4.10: A SRIM-2008 derived damage density of C^+-implanted diamond at 150 keV to a high fluence of 7×10^{15} ions cm^{-2}.

observe that the damage density as calculated by SRIM exceeds the critical threshold of 1×10^{22} vac/cm^3 from the surface. One can see that the amorphous layer is created only at a depth of 130 nm which correspond to a damage density of $\approx 6\times10^{22}$ vac/cm^3 as observed in Figure 4.10. Future work would consist of annealing the sample to 1600 K to see if the near surface layer becomes amorphous. The width of the implanted layer is (80±5) nm, in good agreement with the experimental findings (See Figure 4.9). The figure of (80±5) nm was obtained by the Gaussian fitting method which overestimated the width by tens of nm.

The TEM micrograph in Figure 4.11 is the equivalent of that of Figure 4.4 with one exception: the former lamella was acquired using a Helios Nanolab 650 FIB/SEM and investigated in a double Cs-corrected JEOL JEM-ARM200F HRTEM equipped with a Quantum Gatan Image Filter while the latter image was investigated using conventional bright-field imaging technique in a Philips CM-20 operating at 200 keV

with conventional polishing and ion milling sample preparation methods. Figure 4.11 exhibits a number of thickness fringes, result of preferential gallium ion milling and does not show any visible defects due to the ion implantation followed by annealing in the form of amorphous pockets in the implanted layer. Moreover, visible line and planar defects, from the surface right through the bulk of the diamond sample, are present. Two types of defects are visible in Figures 4.11 and 4.12. These are dislocation loops on three sets of inclined {100} planes and platelets on three sets of inclined {100} planes displaying stacking faults fringes. The reason why all three sets of loops and platelets are visible in this image is because a multi-beam diffraction condition was used for imaging with all six 220 type reflections excited and with the electron beam along the <111> direction. The sharp nature of the diffraction spots in the SAD patterns (see insert in Figure 4.11) indicate that the ion-implanted diamond to the low fluence of 1×10^{15} ions cm^{-2} remained crystalline upon annealing at 1600 K. It is noteworthy mentioning that the platelets and loops present in Figure 4.11 survived the high annealing temperature at 1600 K. The dislocation loops and platelets alluded to in section 4.3.1, which are partially shown in Figure 4.11, are presented in more detail in the TEM micrographs of Figure 4.12 (a). The magnified image in Figure 4.12 (b) is an enlarged image extracted from the middle of image (a), for clarity. These extended defects in the form of platelets (with stacking faults), are typical of type Ia natural diamond used in this study.

The TEM micrograph of C^+-implanted diamond (HPHT, type Ib) at liquid nitrogen temperature with a high fluence of 6×10^{15} ions cm^{-2}, warmed to room temperature first and then annealed at 1600 K is shown in Figure 4.13 (a). We anticipated that this should create an amorphous layer. The TEM micrograph does not show the amorphous layer because it was etched away in the oxidising acid solution. In addition, it was boiled in an oxidising acid which is known to etch away any graphitic carbon.

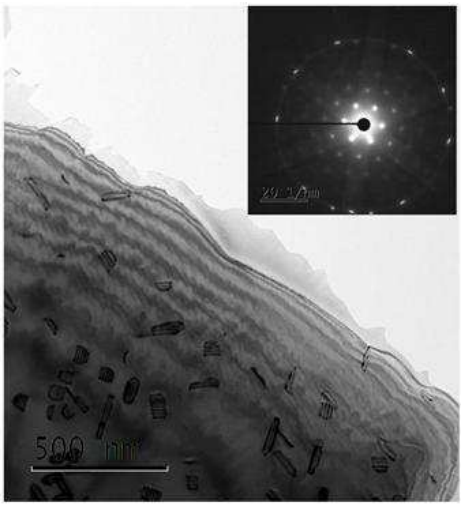

Figure 4.11: Cross-sectional bright-field TEM micrographs of unetched C^+-implanted diamond to a low fluence of 1×10^{15} ions cm^{-2} and annealed at 1600 K with corresponding selected area diffraction pattern in the insert. The SAD (Selected Area Diffraction) pattern shows the 110 reflections of diamond.

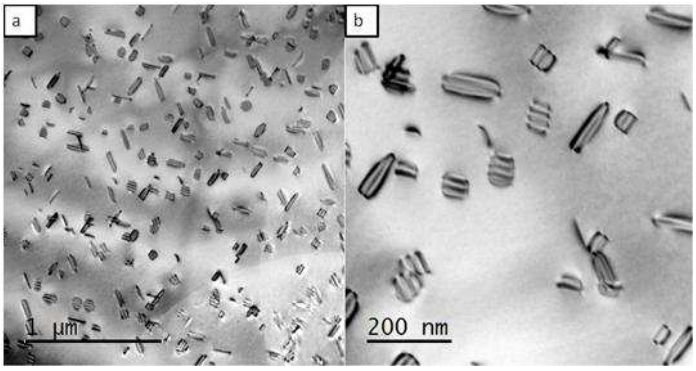

Figure 4.12: Cross-sectional bright-field TEM micrographs of unetched C^+-implanted diamond to a fluence of 1×10^{15} ions cm^{-2} and annealed at 1600 K beyond the implanted range. The magnified image in (b) is an enlarged image extracted from middle of image (a), for clarity. A high density of loops on inclined {111} planes and platelets on {100} planes are visible. The electron beam is along the <111> direction.

The TEM micrographs in Figure 4.13 (b) of diamond (HPHT, type Ib) implanted with carbon ions to a low fluence of 2.5 $\times$ 10^{15} ions cm^{-2} and rapidly annealed does not show either any visible radiation effects and has reverted back to the diamond structure. The TEM micrograph in Figure 4.14 is equivalent to that of Figure 4.6 (a)

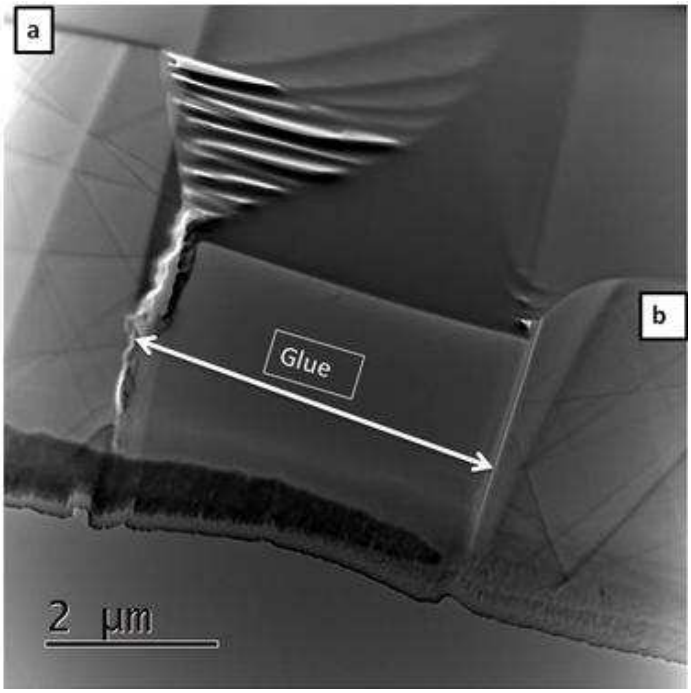

Figure 4.13: Cross-sectional bright-field TEM micrographs of etched C^+-implanted diamond (a) to a fluence of 6×10^{15} ions cm^{-2} warmed to room temperature then annealed at 1600 K and (b) implanted to a fluence of 2.5 $\times10^{15}$ ions cm^{-2} and rapidly annealed at 1600 K.

but with the former prepared using a lift-out cross-section sample preparation method and investigated in a double Cs-corrected JEOL JEM-ARM200F HRTEM while the latter image was investigated using conventional bright-field imaging technique in a Philips CM-20 operating at 200 keV with conventional polishing and ion milling sample preparation methods. An EELS spectrum images maps indicate that it was amorphous (See Figure 4.14 (b)). This result indicates that the amorphous layer of

Figure 4.14 (a) lies from the implanted surface to 250 nm , in agreement with the Monte Carlo simulations shown in Figure 4.1. The interface between the implanted layer and the substrate (shown by the horizontal arrow) consists of disordered carbon. A more detailed account of this disordered carbon will be given in section 4.5.

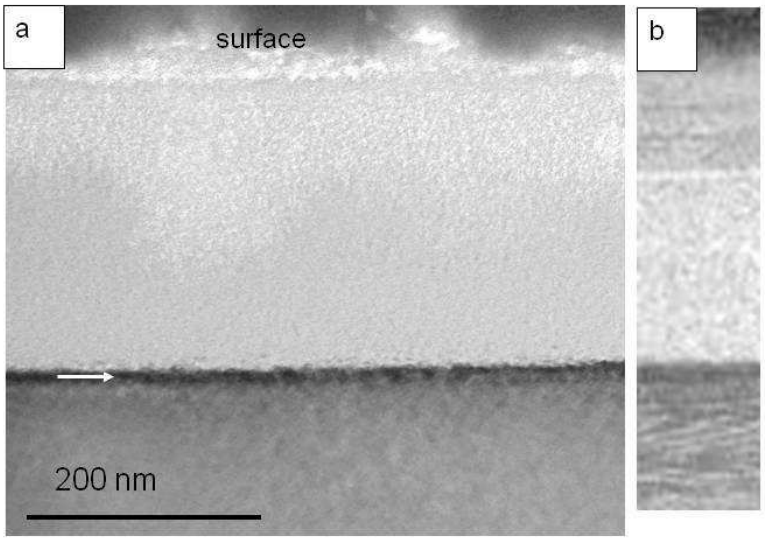

Figure 4.14: (a) Bright-field TEM micrograph of unetched C^+-implanted diamond (HPHT, type Ib) with high fluence of 7×10^{15} ions cm^{-2} and annealed at 1600 K. (b) EELS spectrum image map- obtained by using the $\pi^\star$ peak (284.1-289.9 eV), corresponding to the (sp^2), in the EELS spectrum of the implanted layer.

4.4 EELS results of un-implanted, as-implanted, low and high fluences C^+-implanted diamond.

The EELS core-loss spectra extracted from unimplanted diamond layers shown in Figure 4.15 (a), Figure 4.16 and Figure 4.17 (a) are all characteristic signatures of that of natural diamond, that is, the absence of any peak below around 291 eV followed by the presence of the core-loss K-edge peak at 291 eV which is associated

with the excitations of $\pi^\star$ states of sp^3 with no pronounced drop to low signal for at least 14 eV [145, 146, 147]. The Core EELS spectrum acquired from as-implanted diamond with carbon ions to a fluence of 7×10^{15} ions cm^{-2} at 150 keV, RT, shown in Figure 4.15 (b) shows no sp^2 bonded carbon whose edge lies close to 285.5 eV. The carbon K-edge is at 291 eV which indicates a high degree of disorder in the implanted zone. It is clear that no graphitic carbon is created during ion irradiation.

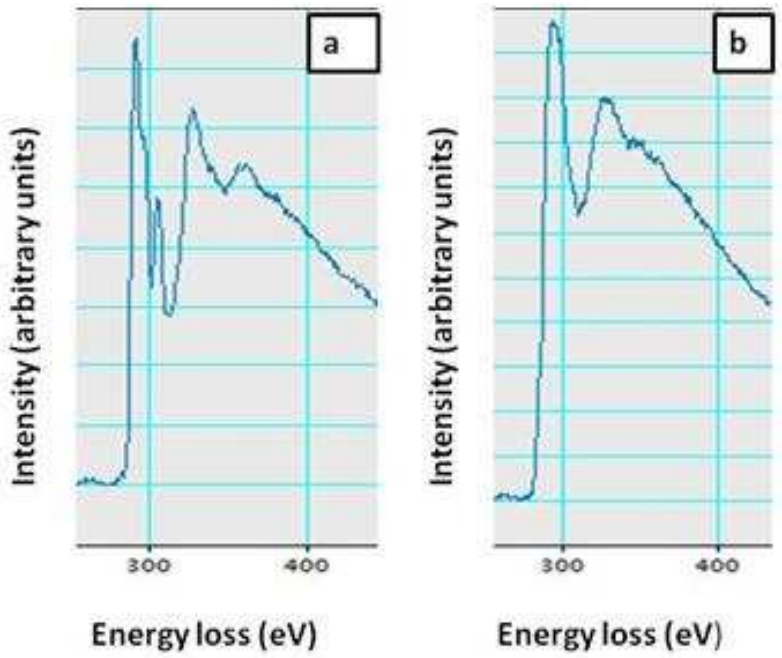

Figure 4.15: (a) Core EELS spectrum acquired from diamond substrate, away from the implanted layer. (b) Core EELS spectrum acquired from C^+-as- implanted diamond to a fluence of 7×10^{15} ions cm^{-2} at 150 keV, room temperature.

The line shape of K-edge in the spectrum acquired from diamond implanted with carbon ions to a low fluence of 1×10^{15} ions cm^{-2} and annealed at 1600 K (CIRA) which is shown in Figure 4.16 is similar to that of unimplanted natural diamond thus corroborating the findings of TEM in conjuction with selected area diffraction which showed that the damaged diamond in the aforementioned conditions reverted back

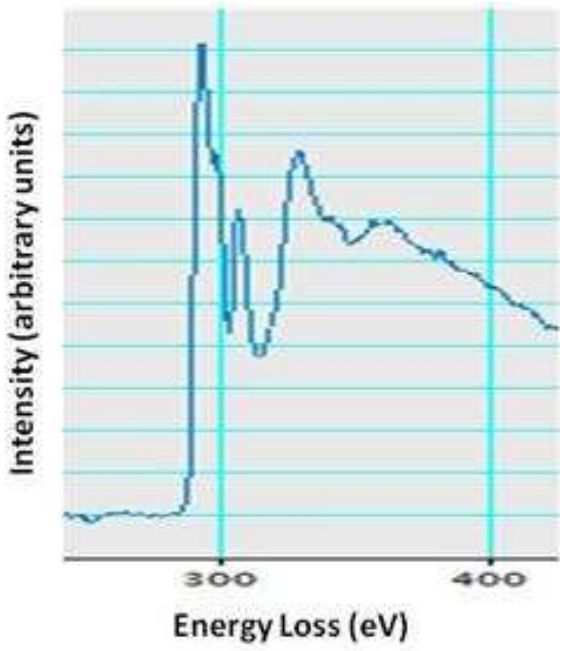

Figure 4.16: Core EELS spectrum acquired from C^+-implanted diamond to a fluence of 1×10^{15} ions cm^{-2} and annealed at 1600 K.

to crystalline diamond.

Figure 4.17 (a) shows an EELS spectrum of the bulk diamond comparable to that of unimplanted diamond and Figure 4.17 (b) is an EELS spectrum of the carbon K- edge obtained by using a window centered upon the $\pi^\star$ peak (284.1-289.9 eV)in Figure 4.17 (b) from the implanted layer with carbon ions to a high fluence of 7×10^{15} ions cm^{-2} and annealed at 1600 K.

Although the $\pi^\star$ peak is an indication of the sp^2 character of the carbon layer, the overall EEL spectrum in Figure 4.17 (b) is characteristic of highly disordered carbon [148] and the spectrum image map of the implanted layer shown in Figure 4.14 (b) indicates that the implanted layer consists of disordered carbon. These findings were confirmed by HRTEM imaging across the implanted region shown in Figure 4.18 (b).

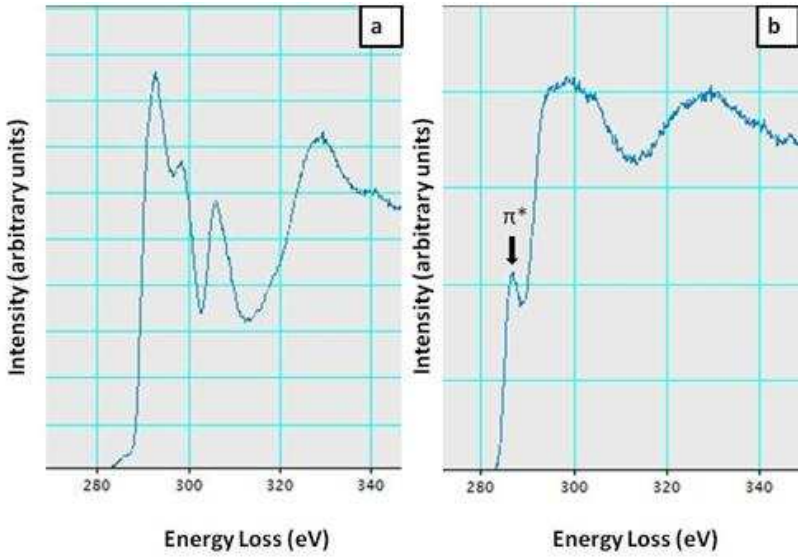

Figure 4.17: (a) EEL Spectrum acquired from bulk diamond (un-implanted) and annealed at 1600 K. The EELS spectrum above indicates the crystalline structure of diamond. (b) EEL Spectrum of the carbon K-edge acquired from C^+-implanted diamond layer to a high fluence of 7×10^{15} ions cm^{-2} and annealed at 1600 K. A pre-edge peak is assigned to the transition from the 1s core level to antibonding $\pi^\star$ levels above the Fermi level.

4.5 HRTEM results of high fluence carbon implanted diamond.

Figure 4.18 (a) is a high-resolution TEM images of unetched C^+-implanted diamond to a high fluence of 7×10^{15} ions cm^{-2} and annealed at 1600 K. The insert shows a corresponding selected area diffraction (SAD) pattern which exhibit the 002 arcs of graphite. The enlarged HRTEM image in Figure 4.18 (b), acquired across the implanted region, clearly shows the presence of regions with bent (002) graphitic fringes and regions of amorphous carbon.

The HRTEM image in Figure 4.19 shows the interface between the implanted layer

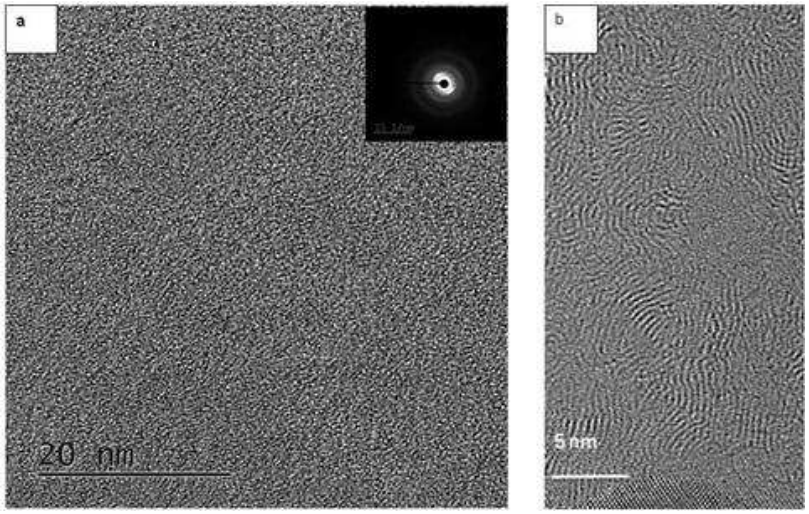

Figure 4.18: (a) High-resolution TEM images of C^+-implanted diamond to a high fluence of 7×10^{15} ions cm^{-2} and annealed at 1600 K. Insert: Corresponding selected area diffraction (SAD) pattern. The SAD pattern exhibits the 002 arcs of graphite. (b) Enlarged HRTEM image acquired across the implanted region.

and the diamond substrate (see the horizontal arrow of Figure 4.14 (a)). Diamond crystallites (D), interspersed between regions of amorphous carbon (A) and partially graphitized carbon (G), are visible in this region. An interesting observation is the lattice images of extended defects (arrowed) visible in the diamond structure at the interface between the implanted region and the diamond substrate shown in Figure 4.19. These defects, which might have been responsible for the dark diffraction contrast visible in Figure 4.14 (a) (See horizontal arrow) were produced at the tail of the projected range of the carbon ions where the ion dose was too low to render the diamond amorphous.

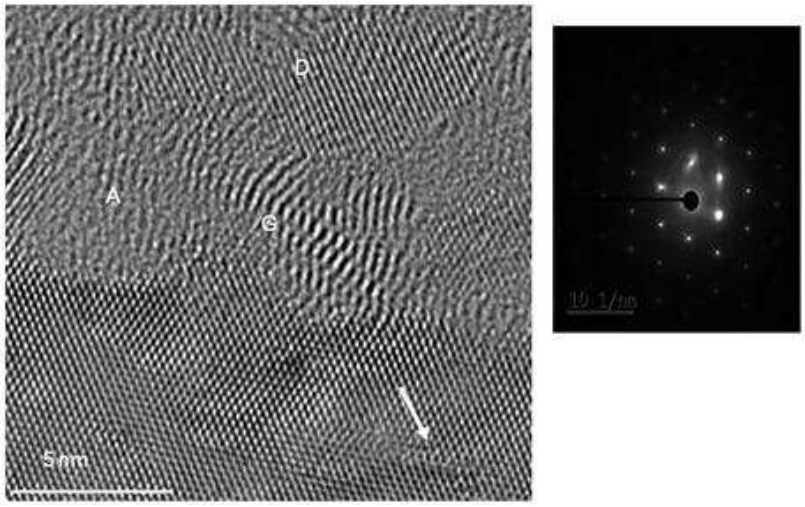

Figure 4.19: High-resolution TEM images of the interface between the implanted layer and diamond substrate. Diamond crystallites (D), interspersed between regions of amorphous carbon (A) and partially graphitized carbon (G), are visible. The arrowed region shows lattice images of extended defects. The selected area diffraction pattern corresponds to the diamond substrate. The SAD pattern of the substrate shows the 111 reflections of diamond.

4.6 Raman spectroscopy of unimplanted, ion-beam thinned, as-implanted, low and high fluence C^+-implanted and annealed diamond samples.

Raman spectroscopy is known as a non destructive tool of crystalline and non-crystalline phases of carbon [149] hence its choice to complement the transmission electron microscopy based techniques used in this work. All the Raman spectra were performed at room temperature and were acquired with the aid of Jobin-Yvon T6400 Raman spectrometer. The argon ion-laser with an excitation wavelength of 514.5 nm was used along side with the green emission line of a mercury lamp at position

1122.42 cm^{-1} employed for Raman spectral calibration.

The power at the sample was nearly 1% of the initial power so as to minimize heating to the diamond sample. For unimplanted natural type Ia and synthetic HPHT type Ib diamonds, the Raman spectra were acquired over a linemap, with the 1800 lines/mm grating and 10 points in a 6 μm straight line accross the centre of the diamond sample.

Figure 4.20 shows a typical first-order Raman spectrum of unimplanted HPHT synthetic type Ib diamond. The Lorentzian peak fitting method allowed the determination of the Raman peak position and the full width at half maximum (FWHM). A sharp Raman peak position at (1330.941±0.008) cm^{-1} with FWHM of (2.08±0.03) cm^{-1} were observed in the Raman spectrum. Similarly, Figure 4.21 shows a typical

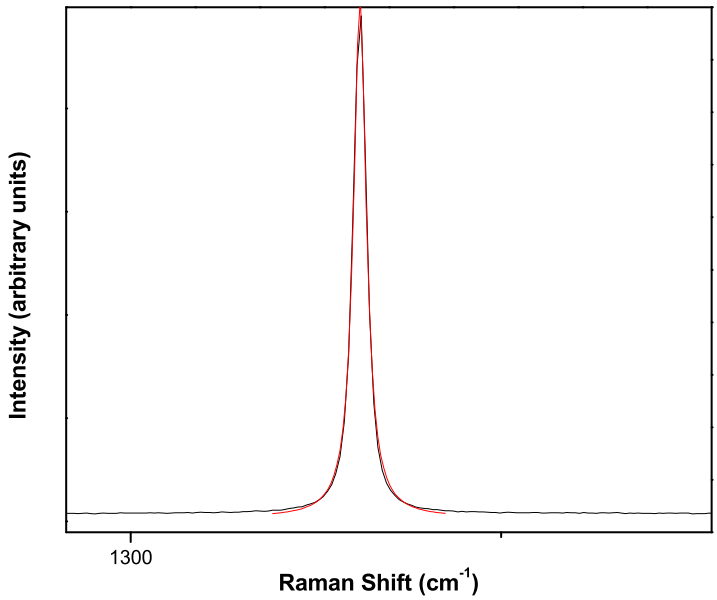

Figure 4.20: Raman spectrum of unimplanted HPHT synthetic type Ib diamond.

first-order Raman spectrum of unimplanted natural type Ia diamond. Its peak position and FWHM with the estimation of their corresponding errors are (1332.024±0.007)

cm^{-1} and (2.36±0.02) cm^{-1}, respectively. Thus the synthetic HPHT and natural diamonds used is this study were of good quality as widths in the range of 2 cm^{-1} are known to be characteristic signatures of good quality diamonds [150].

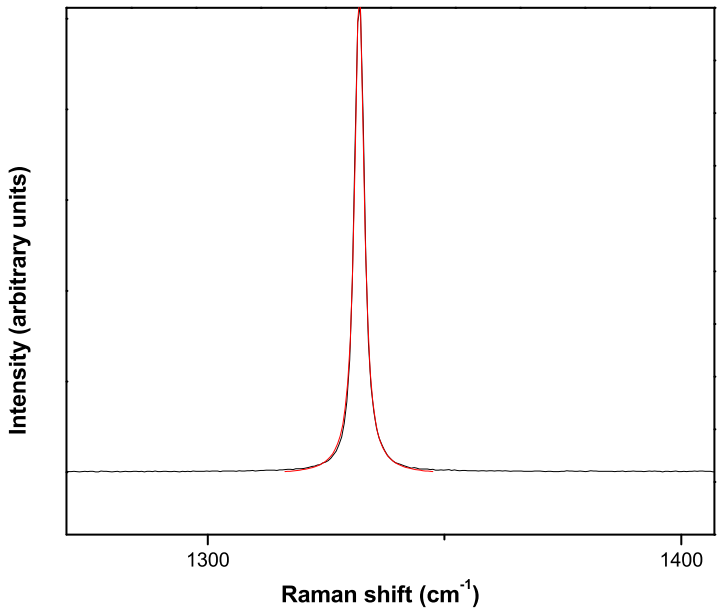

Figure 4.21: Raman spectrum of unimplanted natural Ia diamond.

Figure 4.22 shows Raman spectra acquired from ion-beam thinned sample (HPHT, type Ib) examined in a 200 keV Philip CM20. Thus, any radiation damage inflicted to the diamond lattice by both the ion-beam thinning procedure and TEM observations prior to ion implantation, should, in practice , be assessed. In this regard, the Raman spectrum was acquired from electron transparent regions, very close to the perforated hole. From Figure 4.22, one can see that the intensity of the diamond phonon peak of the ion-beam thinned sample is very low because the volume sampled is small. In addition, the Raman spectrum obtained from the ion-beam thinned/TEM processed diamond (HPHT, type Ib) shows a broad peak at about 1525 cm^{-1} with correspond-

ing linewidth of about 174 cm^{-1} which is consistent with amorphous carbon. This is most probably due to the sputtering process which would leave some residual material behind from the ion milling process. Indeed, even though the observed Raman spectrum shows stress and strain and amorphous carbon, the corresponding TEM micrograph shown in Fig. 4.7(a) shows crystalline diamond. Also, the diamond phonon peak is about 1330 cm^{-1} with FWHM of 5 cm^{-1}. The broadening of the width of the diamond phonon peak from 2.08 cm^{-1} to 5 cm^{-1} may be explained by stress created near the milled diamond surface. Furthermore, the strain in the electron transparent regions may be the cause of the decrease in the Raman frequency due to an increase in tensile stress. Figure 4.23 show a Raman spectrum of an unetched

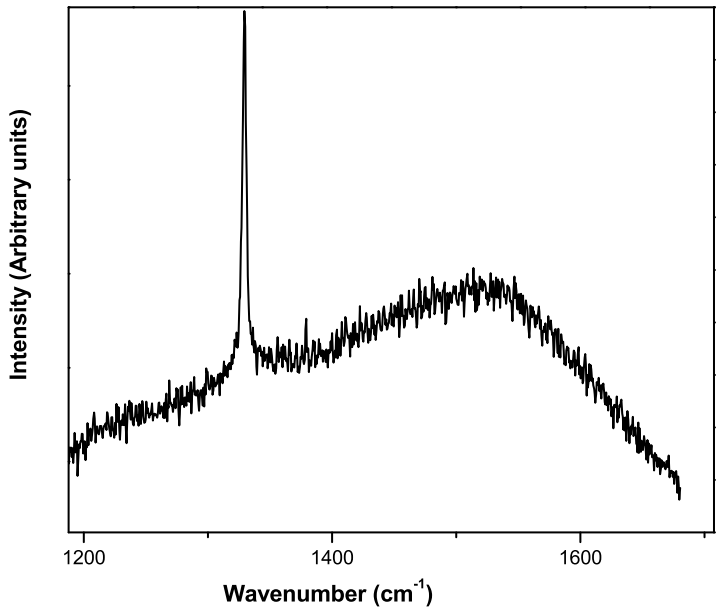

Figure 4.22: Raman spectrum of ion-beam thinned (IBT)/TEM analysed diamond. The Raman spectrum was taken from regions near the perforation, that is, electron transparent regions

C^+-as-implanted HPHT synthetic type Ib diamond, at room temperature at 150 keV,

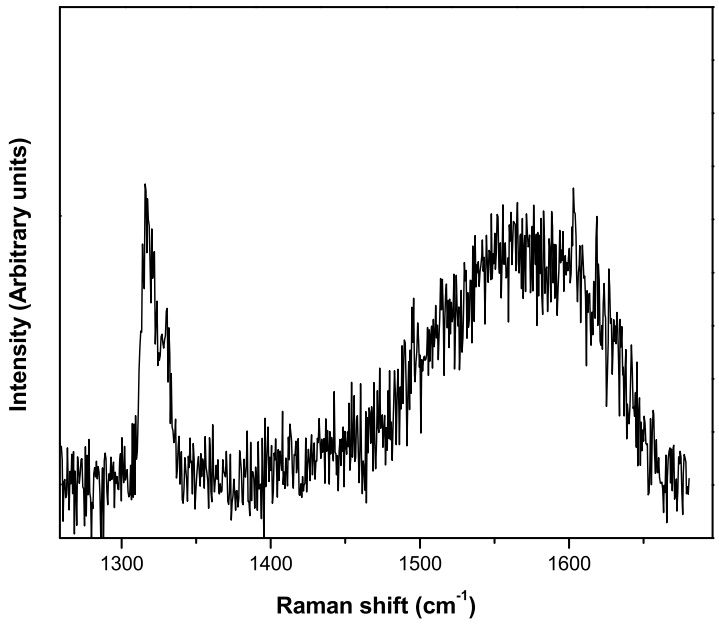

Figure 4.23: Raman spectrum of unetched C^+-as-implanted diamond at room temperature, to a fluence of 7×10^{15} ions cm^{-2} (close to the edge of the perforated hole).

to a fluence of 7×10^{15} ions cm^{-2}. The implantation was performed in the plan-view fashion where implanted ions crossed the electron transparent regions of the ion-beam thinned diamond sample. This was possible because the width of the implanted ions (0.25 μm) is much larger than the thickness of electron transparent regions which is about 100 nm. A G peak was 1568 cm^{-1} at the perforated hole and its linewidth narrowed was 113 cm^{-1}. Interestingly, a peak splitting was observed, with the first diamond phonon peak shifting into two sharp components whose wavenumbers are 1328 and 1317 cm^{-1}. The peak splitting arises most likely from tensile stress within the electrons transparent regions of the ion-beam thinned through which the accelerated ions at 150 keV would have passed. Indeed further Raman analysis performed in thicker regions of the ion-beam thinned diamond which were subjected to the same implantation conditions showed the same broad G peak at 1568 cm^{-1} with no indi-

cation of any peak splitting in the diamond line. The broad G peak at 1568 cm^{-1} is characteristic of amorphous carbon-like structure.

The following Raman measurements were done in the cross-sectional fashion (See Figure 4.24), redrawn from reference [151], where edge implantations were performed and followed by rapid thermal annealing. This cross-sectional configuration allows the laser spot to be focused on a uniform implanted edge of about 0.25 μm from the surface. However the fact that the laser probe covered a diameter of about 4 times larger than the implanted layer-it necessarily implied the sampling of portions of unimplanted diamond. Hence, in all the cross-sectional implantations, the sampling of unimplanted could be avoided by placing the laser probe thoroughly almost tangent to the implanted edge. Figure 4.25 shows low fluence (2.5×10^{15} ions cm^{-2}),

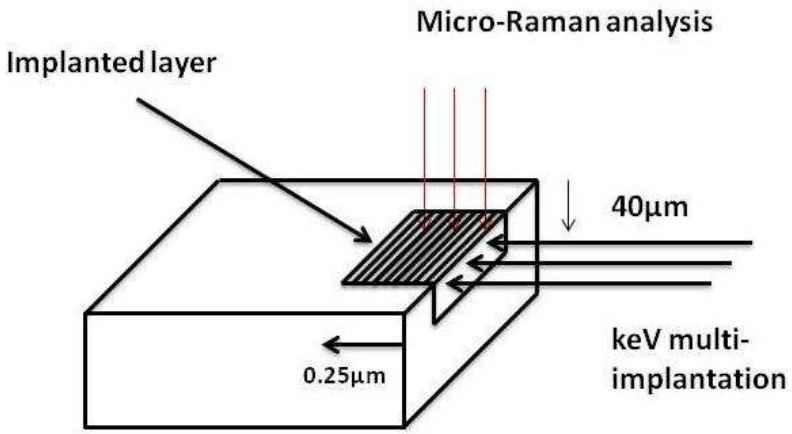

Figure 4.24: Schematic diagram, not to scale, showing cross-sectional geometry of ion-implantation radiation damage in diamond, redrawn after [151]. The thickness of the diamond is 40 μm while the width of the implanted diamond (edge) is 0.25 μm.

unetched C^+-implanted diamond at liquid nitrogen temperature and rapidly annealed at 1600 K. It shows both D (disorder-induced) and G bands which are known to arise from 'the breathing motion of sp^2 rings and the stretching of sp^2 in both rings and chains'[152, 153], respectively. One can see that a sharp first order diamond peak was

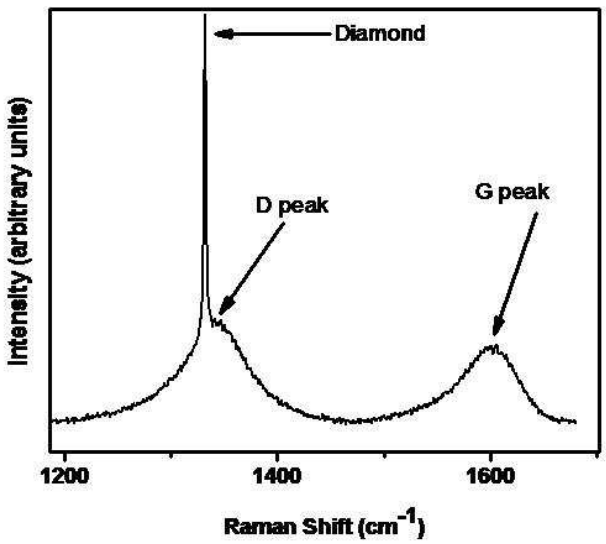

Figure 4.25: Raman spectrum of unetched C^+-implanted diamond (HPHT type Ib) at liquid nitrogen temperature with low fluence of 2.5×10^{15} ions cm^{-2} and rapidly annealed at 1600 K. A weak D band and a broad G peak are observed from carbon contamination. The Raman spectrum was acquired after the CIRA process, i.e. before glueing and milling.

overlapped by a faint or rather a weak D peak at 1341 cm^{-1}, while a broad G peak at 1599 cm^{-1} was observed. The corresponding TEM showed crystalline diamond (See Fig. 4.13 (b)). The observed D and G bands from the Raman for this sample is due to carbon surface contamination from the implantation/annealing process. This contamination is usually observed when the diamond is not cleaned by boiling in an oxidising acid solution.

Figure 4.26 shows high fluence (7×10^{15} ions cm^{-2}), unetched C^+-implanted diamond at liquid nitrogen temperature and rapidly annealed at 1600 K. A sharp D (1355 cm^{-1}) peak and a broad G (1597 cm^{-1}) peak are observed.The FWHM of the D and G bands are 35 cm^{-1} and 49 cm^{-1}, respectively.

In addition, a sharp diamond phonon peak at 1332 cm^{-1}, though low in intensity, is visible due to unavoidable overlap of the laser probe which passed some unimplanted diamond. The D and G peaks as seen in the Raman spectrum, are a signature of amorphous carbon spectra consisting of disordered carbon-findings confirmed by previous HRTEM and EELS studies.

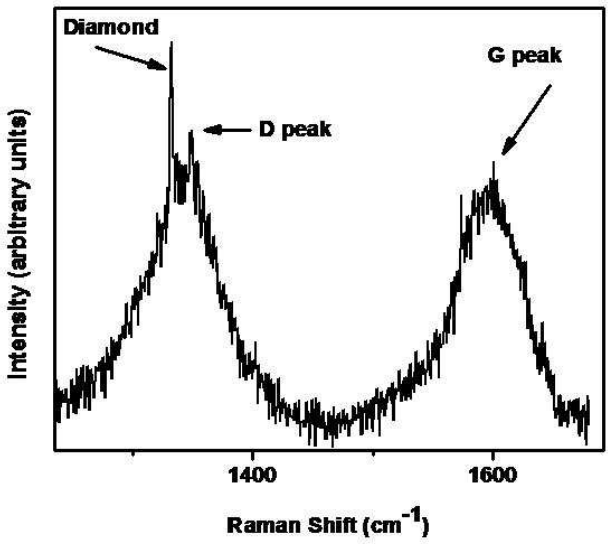

Figure 4.26: Raman spectrum of unetched C^+-implanted diamond (HPHT type Ib) at liquid nitrogen temperature with high fluence of 7×10^{15} ions cm^{-2} and rapidly annealed at 1600 K. Sharps D and G peaks are visible. The Raman spectrum was acquired after the CIRA process, i.e. before glueing and milling.

Chapter 5

Summary and Conclusions

The main purpose of this work was to understand the nature of the radiation damage accompanying carbon implanted and annealed diamonds. In this work, high-pressure, high temperature (HPHT) synthetic type Ib and natural type Ia diamonds irradiated by carbon ions according to the CIRA (Cold-Implantation-Rapid-Annealing) routine were investigated using cross sectional transmission electron microscopy coupled with selected area diffraction (SAD), High resolution transmission electron microscopy (HRTEM), electron energy loss spectroscopy (EELS) and Raman spectroscopy.

For sample preparation, two complementary methods were used to create cross sectional TEM samples from single crystal diamond. The first method consisted of combining mechanical polishing and ion milling, which was lengthy and challenging. The second method used FIB-SEM and in situ lift-out which turned out to be much faster and more reliable than the former. In addition, complementary characterization methods were chosen carefully so as to get thorough details of any amorphization and graphitic phase change of single-crystal diamond substrate subjected to ion implantation followed by annealing. In this regard, informative details were obtained using high resolution transmission electron microscopy (HRTEM) in conjunction with electron energy-loss spectroscopy (EELS) which imaged not only the crystallographic structure of the damaged diamond but also correlated EELS spectra with the radia-

tion effects viewed in HRTEM.

The results obtained show that as-implanted high pressure high temperature type Ib diamond with single energy of 150 keV carbon ions and fluence of 7×10^{15} ions cm^{-2} revealed an amorphous sp^3-type diamond layer of about 80 nm in thickness. In unimplanted type Ia natural diamond, a high density of platelets, exhibiting the typical contrast of both edge-on and inclined platelets on {100} planes was found. Also, it was found that irradiated HPHT synthetic type Ib diamond at sub-critical implantation fluences followed by a rapid thermal annealing (RTA) in a flowing argon atmosphere anneals back to crystalline diamond. In contrast to the sub-critical implantation fluences, i.e., above the critical threshold, the damaged diamond layer consists of disordered carbon comprising regions with bent (002) graphitic fringes and regions of amorphous carbon. Also, Raman spectroscopy of the damaged diamond layer above the critical threshold showed both D (disorder-induced) and G peaks which are known to arise from 'the breathing motion of sp^2 rings and the stretching of sp^2 in both rings and chains'[152, 153], respectively. These are a signature of disordered carbon thus corroborating HRTEM and EELS findings.

It is important to stress that immediately following ion irradiation to fluence well above the critical threshold, no graphitic carbon is observed in the implanted layer. It is only upon annealing that graphitic sp^2 carbon is observed in the EELS spectrum. Furthermore, the interface between the implanted and annealed layer and the diamond substrate at the end of the range, showed diamond crystallites interspersed between regions of amorphous carbon and partially graphitized carbon. This indicates that solid phase epitaxial recrystallization regrowth in diamond does not occur. Also, it is worth mentioning that the end of range damage in keV implants is similar to that of MeV implants

No extended defects in the form of dislocation loops which occur in silicon, for instance, at the end of range after implantation followed by annealing were observed in this study.

The damage threshold for keV implants is estimated to be at $\approx 6\times10^{22}$ vac/cm^3 for single energy implantation of carbon ions at 150 keV, which is almost six times higher than the known damage threshold (1×10^{22} vac/cm^3) for keV single energy implantations.

The CIRA method which consists of implanting the total fluence with a spread of energies i.e. over larger width is more advantageous than implanting the total fluence at a single energy. Indeed, one can see that the micrograph of Figure 4.3b shows a dark band of damage after a LN_2 implant ,which was not annealed, with the total fluence spread by using different energies. The implanted area still shows a high degree of order after implantation to a high fluence. In contrast, the micrograph of Figure 4.9 obtained for a nearly similar fluence but at single energy, room temperature and pressure shows a more apparent contrast in the damaged region. Both these fluences were chosen above the critical damage threshold. It therefore stands to reason that the recovery of the diamond structure is better achieved with the fluence spread over a wider width. In addition, the initial idea as proposed by Morehead and Crowder with regards to the precipitation of damage appears not to be applicable to diamond. If any graphitic regions created along the ion track due to thermal spikes were created, one should have observed these regions at atomic resolution in the EELS spectra after implantation. Within the context of this study, there is no evidence of graphitic carbon. The graphitic regions observed in the case of a high fluence implant followed by a rapid annealing were nano crystallites of graphite in an 'amorphous carbon'[1] matrix, implying that there were no long range order of the carbon atoms. Last but not least, for future work, it would be interesting to follow the evolution of the implantation damage in annealed diamond, varying ion fluences, the annealing temperatures, ion species and dose rates, using TEM, HRTEM, EELS and Raman spectroscopy characterization techniques. The latter variable (dose rates) is often ignored but can be very important when nucleation events become influential.

[1] sp^3 bonded carbon with no long range order.

References

[1] J.O. Orwa, K.W. Nugent, D.N. Jamieson, and S. Prawer. *Phys. Rev. B.*, **62**:5461, 2000.

[2] V.S. Vavilov, M.I. Guseva, E.A. Koronova, V.V. Krasnopevtsev, V.F. Sergienko, and V.V. Tutov. *Soviet Phys. Solid State*, **8**:1560, 1966.

[3] R.O. Carlson. *Trans. Metall. Soc. AIME*, **245**:483, 1969.

[4] P.F. Lai, S. Prawer, and L.A. Bursill. *Diam. & Relat. Mater.*, **10**:82, 2001.

[5] D.P. Hickey, E Kurlyliw, K. Siebein, K.S. Jones, R Chodelka, and R. Elliman. *Journal of Vacuum Science & Technology A 24*, **24**:1302, 2006.

[6] D.P. Hickey, K.S. Jones, and R. Elliman. *Diam. & Relat. Mater.*, **18**:1353, 2009.

[7] T.E. Derry, E.K. Nshingabigwi, C.M. Levitt, J. Neethling, and S.R. Naidoo. *Nucl. Instr. and Meth. in Phys. Res. B.*, **267**:2705, 2009.

[8] E.K. Nshingabigwi, J.H. Neethling, C.M. Levitt, S.R. Naidoo, and T.E. Derry. In I. Basson and A.E. Botha, editors, *Proceedings of SAIP 2011, the 56th Annual Conference of the South African Institute of Physics*, page 711. University of South Africa, Pretoria, 2011, 2011. ISBN: 978-1-86888-688-3. Available at http://www.saip.org.za.

[9] L.W. Yin, Z.D. Zou, M.S. Li, G.L. Geng, D.S. Sun, and Z.Y. Hao. *Cryst. Res. Technol.*, **35**:1289, 2000.

[10] J.S. Williams. *Rep. Prog. Phys.*, **49**:491, 1986.

[11] M.S. Dresselhaus and R. Kalish. *Ion implantation in Diamond, Graphite and Related Materials*. Springer Verlag, Berlin, 1992.

[12] C. Uzan-Saguy, C. Cytermann, R. Breuer, H. Shaanan, and R. Kalish. *Appl. Phys. Lett.*, **67**:1194, 1995.

[13] B.A. Fairchild, P. Olivero, S. Rubanov, A.D. Greentree, F Waldermann, R.A. Taylor, S. Smith, S. Huntington, B.C. Gibson, D.N. Jamieson, and S. Prawer. *Advanced Materials*, **20**:4793, 2008.

[14] P. Olivero, S Rubanov, P. Reichart, B.C. Gibson, S.T. Huntington, J.R. Rabeau, A.D. Greentree, J. Salzman, D. Moore, D.N. Jamieson, and S. Prawer. *Diam. & Relat. Mater.*, **15**:1614, 2006.

[15] R.A. Kalish, A. Reznik, K.W. Nugent, and S. Prawer. *Nucl. Instr. and Meth. in Phys. Res. B.*, **148**:626, 1999.

[16] S. Prawer, D.N. Jamieson, K.W. Nugent, R. Walker, C. Uzan-Saguy, and R. Kalish. *Mater. Res. Soc. Symp. Proc.*, **647**:04.3.1, 1999.

[17] S. Sato. *Nucl. Instr. and Meth. in Phys. Res. B.*, **59/60**:1391, 1991.

[18] F.A. Cotton and G. Wilkinson. *Adv. Inorg. Chem.* Interscience Publishers, New York, 1962.

[19] R.H. Petrucci and W.S. Harwood. *General Chemistry: Principles & Modern Applications*. Mac Millan Publishing Company, 6 edition, 1993.

[20] J. Robertson. *Mater. Science and Eng. R* ***37***, pages 129,130, 2002.

[21] J. Robertson. *Prog. Solid St. Chem*, **21**:201, 1991.

[22] H.O. Pierson. *Handbook of Carbon, Graphite, Diamond and Fullerenes. Properties, Processing and Applications*. Noyes Publications, New Jersey, 1993.

[23] T.H. Hall. *Journal of Chemical Education.*, **38**:484, 1961.

[24] D.R. McKenzie. *Rep. Prog. Phys.*, **59**:1611, 1996.

[25] F.P. Bundy, W.A. Basset, M.S. Weathers, R.J. Hemley, H.K. Mao, and A.F. Goncharov. *Carbon*, **34**:141, 1996.

[26] A.C. Ferrari and J. Robertson. *Phys. Rev. B.*, **61**:2477, 2000.

[27] A.C. Ferrari and J. Robertson. *Phil. Trans. R. Soc. Lond. A*, **362**:2477, 2004.

[28] J.L. Peng, L.A. Bursill, B. Jiang, J.O. Orwa, and S. Prawer. *Phil. Mag Part B*, **81**:2071, 2004.

[29] D.R. LIDE, editor. *Handbook of Chemistry and Physics*. CRC Press, Boston, USA, 86 edition, 2005-2006.

[30] G. Dresselhaus, M.S.a nd Dresselhaus and P.C. Eklund. *Science of Fullerenes and Nanotubes*. Academic press, San Diego, 1996.

[31] T. Singh, M.J. Behr, E.S. Aydil, and D. Maroudas. *Chem. Phys. Lett.*, **474**:168, 2009.

[32] B. Wen, T. Li, X. Zhang, S. Yao, Z. Cao, D. Wang, S. Ji, and J. Jin. *J. Phys. : Condens. Matter*, **16**:2991, 2004.

[33] J. Robertson. *Adv. Phys*, **35**:317, 1986.

[34] G.M. Pharr, D.L. Callahan, S.D. Mc Adams, T.Y. Tsui, S. Anders, A. Anders, J.W. Ager, I.G. Brown, C.S. Bhatia, S.R.P. Silva, and J. Robertson. *Appl. Phys. Lett.*, **68**:779, 1996.

[35] P.J. Fallon, V.S. Veerasamy, C.A. Davis, J. Roberton, G.A.J. Amaratunga, W.I. Milne, and J. Koskinen. *Phys. Rev.*, **48**:4777, 1993.

[36] P. Koidl, C.H. Wild, B. Dischler, J. Wagner, M. Ramsteiner, W.I. Milne, and J. Koskinen. *Mater. Sci. Forum*, **52**:41, 1990.

[37] M. Weiler, S. Sattel, K. Jung, H. Ehrhardt, V.S. Veerasamy, and J. Robertson. *Appl. Phys. Lett.*, **64**:2797, 1994.

[38] G. Burns and A.M. Glazer. *Space Groups for Solid State scientists*. Academic Press, New York, 1978.

[39] L. S. Hounsome. PhD thesis, University of Exeter, 2007.

[40] J.D. Patterson and B.C. Bailey. *Solid- State Physics: Introduction to the theory*. Springer Verlag, Berlin, 2007.

[41] D.B. Holt and B.G. Yacobi. *Extended Defects in Semiconductors: Electronic Properties, Device Effects and Structure*. Cambridge University Press, Cambridge, 2007.

[42] S. J. Sque. PhD thesis, University of Exeter, 2005.

[43] W. Zhu. *Diamond: Electronic properties and Applications*, chapter : Defects in Diamond, page 173. Kluver Academic Publishers, London, 1995.

[44] M. Seal. In J.E. Field, editor, *The Properties of Natural and Synthetic Diamond*, page 622. Academic Press, London, 1992.

[45] J.F. Prins. *Mater. Sci. Rep.*, **7**:271, 1992.

[46] M. Moore. *Diamond: Natural*. Encyclopedia of materials: Science and Technology. 2008.

[47] K. Iakoubovskii and A. Stesman. *J. Phys.:Condens. Matter*, **14**:R467, 2002.

[48] A.M. Zaitsev. *Optical Properties of Diamond: A data Handbook*. Springer-Verlag, Berlin Heidelberg New York, 2001.

[49] A.T. Collins. *In The Physics of Diamond Course CXXXV, Proc.Int.School of Physics*. IOS PRESS, 1997.

[50] J. Beckman, R.B. Jackman, and J.S. Foord. *Diam. & Relat. Mater.*, **3**:602, 1994.

[51] G.S. Woods, I. Kiflawi, W Luyten, and van Tendello. *Phil. Mag. Letters*, **67**:405, 1993.

[52] O. Fukunuga, T. Miyake, and N. Ohashi. *Diam.& Relat. Mater*, **14**:160, 2005.

[53] J. Siebert, F. Guyot, and V. Malavergne. *Earth and Planetary Science Letters*, **229(3-4)**:205, 2005.

[54] C. Burns, R, O. Hansen, J, R.A Spits, and M. Sibanda. *Diam.& Relat. Mater*, **8**:1433, 1999.

[55] K. Johnston. PhD thesis, University of London, 2000.

[56] G. Farrer, R. *Solid State Commun.*, **7**:685, 1969.

[57] F. Prins, J. *Nucl. Instr. and Meth. in Phys. Res. A.*, **514**:69–70, 2003.

[58] S. Koizumi, H. Ozaki, M. Kano, Y. Sato, and T. Inuzuka. *Appl. Phys. Lett.*, **71**:1065, 1992.

[59] S. Koizumi, M. Kamo, S. Mita, A. Sawabe, A. Reznik, C. Uzan-Saguy, B Rau, and R. Kalish. *Diam.& Relat. Mater*, **7**:540, 1998.

[60] B. Butorac and A. Mainwood. *Phys. Rev.*, **78**:235204, 2008.

[61] S. Koizumi, Kamo M., Y. Sato, H. Ozaki, and T. Imizuka. *Appl. Phys. Lett.*, **71**:1065, 1997.

[62] J.F. Prins. *Diam. & Relat. Mater.*, **8**:1635, 1999.

[63] H. Sternschulte, Thonke K., R. Sauer, and S. Koizumi. *Phys. Rev. B.*, **59**:12924, 1999.

[64] M. Gabrysch. PhD thesis, Uppsala Universitet, 2008.

[65] J.F. Prins. *Semicond. Sci.Techn.*, **16**:540, 2001.

[66] R. Kalish. *J. Phys. D: Appl. Phys*, **40**:6468, 2007.

[67] J.F. Prins. *Applications of diamond films in electronics.* Proceedings of the International School of PhysicsEnrico Fermi' Course CXXXV. IOS Press Amsterdam, 1997.

[68] P.D. Towsend, P.J. Chandler, and L. Zhang. *Optical effects of Ion Implantation.* Cambridge University Press, 1994.

[69] R.A. Spits, J.F. Prins, and T.E. Derry. *Nucl. Instr. and Meth. in Phys. Res. B.*, **85**:347, 1994.

[70] T.E. Derry, R.A. Spits, and J.P.F. Sellschop. *Mater. Sc. and Eng, B.*, **11**:249, 1992.

[71] J.F. Prins. *Semicond. Sci.Techn.*, **18**:S27, 2003.

[72] R.A. Spits, J.F. Prins, J.D. Comins, and T.E. Derry. *S. Afr. J. Phys.*, **85**:17, 1993.

[73] L.C. Feldman and J.W. Mayer. *Fundamentals of surfaces and thin film analysis.* Elsevier Science Publishing Co., Inc, North Holland, Amsterdam, 1986.

[74] D. Fink. *Brazilian Journal of Physics*, **35**, $n^0$3B:735, 2005.

[75] J.S. Williams. *Rep. Prog. Phys.*, **49**:494–498, 1986.

[76] J. Lindhard and V. Nielson. *Physics Letters*, **2**:210, 1962.

[77] P.D. Townsend, J.C. Kelly, and N.E.W. Hartley. *Ion implantation, Sputtering and their Applications.* Academic Press, London, 1976.

[78] G. Carter and J.S. Colligon. *Ion bombardment of Solids.* Heinemann Educational Books Ltd, London, 1969.

[79] L. Marton. *Advances in electronics and electron physics*, volume 37. Academic Press, Inc., New York, 1975.

[80] G.O. Amolo. PhD thesis, University of the Witwatersrand, 2007.

[81] J.W. Mayer, L. Eriksson, and J.A. Davies. *Ion implantation in Semiconductors: Silicon and Germanium.* Academic Press, New York, 1970.

[82] S.M. Sze. *VLSI Technology.* McGraw-Hill, Boston, 2nd edition, 1988.

[83] R. Kalish, A. Reznik, D. Saada, and J. Adler. *Phys. St. Sol(a).*, **174**, 1999.

[84] D.S. Billington and J.H. Crawford Jr. *Radiation damage in Solids.* Oxford University Press, London, 1961.

[85] J.F. Prins. *Phys. Rev. B.*, **38**:5576, 1988.

[86] T.E. Derry, J.F. Prins, C.C.P. Madiba, J. Ennis, R.A Spits, and J.P.F. Sellschop. *Nucl. Instr. and Meth. in Phys. Res. B.*, **35**:431, 1988.

[87] R.S. Nelson, J.A. Hudson, and D.J. Mazey. *Br. Patent I 476313.* June 10, 1997.

[88] D. Saada. PhD thesis, Israel Institute of Technology, 2000.

[89] R. Kalish, A. Reznik, S. Prawer, D Saada, and J. Adler. *Phys. Stat. Sol. (a)*, **174**:83, 1999.

[90] S.J. Breuer and P.R. Briddon. *Phys. Rev. B.*, **51**:6984, 1995.

[91] D. Saada, Adler J., and R. Kalish. *Int. J. Mod. Phys.C*, **9**:61, 1998.

[92] J.F. Prins. *Phys. Rev. B.*, **39**:3764, 1989.

[93] T.L. Alford, L.C. Feldman, and J.W. Mayer. *Fundamentals of Nanoscale Film Analysis*. SpringerScience + Business Media, Inc, USA, 2007.

[94] B.J. Sealy. *Mater. Sci.Techn.*, **4**:500, 1988.

[95] A.R. Sattler and G. Dearnaley. *Phys. Rev.*, **161**:244, 1967.

[96] R. Simonton and A.F. Tasch. *Handbook of Ion Implantation Technology*, chapter :Channelling effects in ion implantations, page 21. Elsevier Science Publisher B.V, North Holland, 1992.

[97] http://www.vandiamond.com/article/knowledge-quest-series/cutting-a-diamond/. Accessed on 3/8/2011.

[98] T.E. Derry, R.W. Fearick, and J.P.F. Sellschop. *Phys. Rev. B.*, **24**:3675, 1981.

[99] J.E. Field. *Properties and Growth of Diamond*, pages 36–51. Emis Datareview Series No.9, INSPEC. Short Run Press Ltd. Exeter, London, United Kingdom, 1994.

[100] M. Rebak, J.P.F. Sellschop, and S.H. Connell. *Nucl. Instr. and Meth. in Phys. Res. B.*, **85**:243, 1994.

[101] N.W. Makau. PhD thesis, University of the Witwatersrand, 2006.

[102] F.M. van Bouwelen. *Diam. & Relat. Mater.*, **9**:925, 2000.

[103] S.E. Grillo, J.E. Field, and F.M. van Bouwelen. *J. Phys. D: Appl. Phys.*, **33**:985, 2000.

[104] M. Tolkowsky. D.Sc, University of London, 1920.

[105] E.M. Wilks and J. Wilks. *J. Phys. D: Appl. Phys.*, **5**:1902, 1972.

[106] J.R. Hird and J.E. Field. *Proc. R. Soc. Lond. A*, **460**:3547, 2004.

[107] M. Rebak. Private communication. 2004.

[108] J.R. Hird and J.E. Field. *Wear*, **258**:18–25, 2005.

[109] Y. Yarnitsky, J.P.F. Sellschop, M. Rebak, and S. Bartolucci Luyckx. *Mater. Sc. Engin. A*, **105/106**:565, 1988.

[110] M.S. Couto, W.J.P. van Enckevort, and M. Seal. *Phil. Mag. B.*, **69** 105/106:621, 1994.

[111] F.M. van Bouwelen, J.E. Field, and L.M. Brown. *Phil. Mag. No.7*, **83**:839, 2003.

[112] S. Prawer. *Diam. & Relat. Mater.*, **4**:864, 1995.

[113] Varian/Extrion. *Instruction manual production Ion Implanter model 200-20A2F*. Varian Extrion Division, Chapman & Hall, Gloucester UK, 1977.

[114] P.H. Rose. *Nucl. Instr. and Meth. in Phys. Res. B.*, **6**:1, 1985.

[115] J. Field, R. Caveney, J. Lomer, and C. Welbourn. In *The 62nd diamond Conference*, Warwick, July 2011.

[116] J.F. Prins. *Diam. & Relat. Mater.*, **9**:1275–1276, 2000.

[117] J.F. Prins. *Diam. & Relat. Mater.*, **10**:1756, 2001.

[118] S.R. Naidoo. PhD thesis, University of the Witwatersrand, 2007.

[119] J.F. Prins. *Diam. & Relat. Mater.*, **9**:1835, 2000.

[120] M. Razeghi. *Fundamentals of Solid State Engineering*, volume 2. Springer Science + Business Media, Inc, 2006.

[121] S. Mogck. PhD thesis, Groningen University, 2004.

[122] D.B. Williams and C.B. Carter. *A textbook for Materials Science*. Springer Science + Business Media, 2nd edition, 2009.

[123] D. Brandon and W.D. Kaplan. *Microstructural characterization of materials*, pages 123–260. John Wiley & Sons, Ltd, England, 2nd edition, 2008.

[124] A. Bhuiyan. Private communication. 2007.

[125] L.A. Woodward. General introduction. In H.A. Szymanski, editor, *Raman spectroscopy: Theory and Practice*, chapter 1, pages 1–43. Plenum Press, New York, 1967.

[126] R.L. McCreery. Magnitude of Raman scattering. In J.D. Wineforder, editor, *Raman spectroscopy for Chemical Analysis*, volume 157 of *Chemical Analysis*, chapter 2, page 15. A Wiley-Interscience publication, Canada, 2000.

[127] H. Kuzmany. *Solid-State Spectroscopy: An introduction*, chapter 9, page 169. Springer Verlag, Berlin, 1998.

[128] S. Reich, C. Thomsen, and J. Maultzsch. *Carbon Nanotubes: Basic concepts and Physical Properties*, chapter 7 & 8, pages 115–176. Wiley-Vch Verlag GmbH & Co. KGaA, Weinheim, 2003.

[129] D.A. Long. *The Raman effect: A unified treatment of the theory of Raman scattering by molecules*, chapter 2, page 19. John Wiley & Sons, Ltd, UK, 2002.

[130] G. Keresztury. Raman spectroscopy: Theory. In J.M. Chalmers and P.R. Griffiths, editors, *Handbook of Vibrational Spectroscopy*, volume 1, chapter 1 & 2. John Wiley, Ltd, New York, 2002.

[131] S. Ndiaye. Private communication. 2004.

[132] R.M. Erasmus. Private communication. 2005.

[133] Y. Leng. *Materials characterization: Introduction to microscopic and spectroscopic methods*. John Wiley & Sons (Asia) Pte Ltd, 2008.

[134] D.A. Long. *Raman spectroscopy*. McGraw-Hill, Inc, 1977.

[135] B. Fulz and J.M. Howe. *Transmission electron microscopy and diffractometry of materials*. Springer-Verlag, Berlin, 3nd edition, 2008.

[136] M.L. Jenkins and M.A. Kirk. *Characterization of Radiation Damage by Transmission Electron Microscopy*. IOP Publishing, Oxford, 2001.

[137] A.T. Blumenau. PhD thesis, der Universität Paderborn, 2002.

[138] P. Kovarik. *Phys. Rev. B.*, **48**:12123, 1993.

[139] J.F. Ziegler. Srim 2008(software package), 2008. http://www.srim.org/.

[140] S. Prawer and R. Kalish. *Phys. Rev. B.*, **51**, 1995.

[141] J. Koike, D.M. Parkin, and T.E. Mitchell. *Appl. Phys. Lett.*, **60**:1450, 1992.

[142] A.R. Lang. *Proc. Phys. Soc. Lond.*, **84**:871, 1964.

[143] G.S. Woods. *Proc. R. Soc. Lond. A*, **407**:219, 1986.

[144] F.F. Morehead and B.L. Crowder. *Radiat. Effect.*, **6**:27, 1970.

[145] B.E. Williams and J.T. Glass. *J. Mater. Res.*, **4**:373, 1989.

[146] P.K. Chu and L. Li. *Mater. Chem and Phys.*, **96**:253, 2006.

[147] A.A. El-Barbary, S. Trasobars, C.P. Ewels, O. Stephan, A.V. Okotrub, L.G. Bulusheva, C.J. Fall, and M.I. Heggie. *Journal of Physics: Conf. Series*, **26**:149, 2006.

[148] H. Daniels, R. Brydson, B. Rand, and A. Brown. *Phil. Mag.*, **87**:4073, 2007.

[149] S. Prawer, K.W. Nugent, D.N. Jamieson, J.O. Orwa, L.A. Bursill, and J.L. Peng. *Chem. Phys. Lett.*, **332**:93, 2000.

[150] D.S. Knight and W.B. White. *J. Mater. Res.*, **4**:93, 1989.

[151] D.N. Jamieson, S. Prawer, K.W. Nugent, and S.P. Dooley. *Nucl. Instr. and Meth. in Phys. Res. B.*, **106**:641, 1995.

[152] A.C. Ferrari and J. Robertson. *Phys. Rev. B.*, **64**:075414, 1991.

[153] J. Filik. *14spectroscopyeurope*, **17**, 2005.